BNL-220916-2021-JAAM

Measurements of Dihadron Correlations Relative to the Event Plane in Au+Au Collisions at √sNN= 200 GeV

D. Arkhipkin

To be published in "Chinese Physics C"

January 2021

Physics Department

Brookhaven National Laboratory

U.S. Department of Energy

USDOE Office of Science (SC), Nuclear Physics (NP) (SC-26)

Notice: This manuscript has been authored by employees of Brookhaven Science Associates, LLC under Contract No. DE-SC0012704 with the U.S. Department of Energy. The publisher by accepting the manuscript for publication acknowledges that the United States Government retains a non-exclusive, paid-up, irrevocable, world-wide license to publish or reproduce the published form of this manuscript, or allow others to do so, for United States Government purposes.

DISCLAIMER

This report was prepared as an account of work sponsored by an agency of the United States Government. Neither the United States Government nor any agency thereof, nor any of their employees, nor any of their contractors, subcontractors, or their employees, makes any warranty, express or implied, or assumes any legal liability or responsibility for the accuracy, completeness, or any third party's use or the results of such use of any information, apparatus, product, or process disclosed, or represents that its use would not infringe privately owned rights. Reference herein to any specific commercial product, process, or service by trade name, trademark, manufacturer, or otherwise, does not necessarily constitute or imply its endorsement, recommendation, or favoring by the United States Government or any agency thereof or its contractors or subcontractors. The views and opinions of authors expressed herein do not necessarily state or reflect those of the United States Government or any agency thereof.

arXiv:1010.0690v3 [nucl-ex] 21 Oct 2020

Measurements of Dihadron Correlations Relative to the Event Plane in Au+Au Collisions at $\sqrt{s_{\rm NN}} = 200$ GeV

H. Agakishiev,[17] M. M. Aggarwal,[29] Z. Ahammed,[21] A. V. Alakhverdyants,[17] I. Alekseev ,[15] J. Alford,[18] B. D. Anderson,[18] C. D. Anson,[27] D. Arkhipkin,[2] G. S. Averichev,[17] J. Balewski,[22] D. R. Beavis,[2] N. K. Behera,[13] R. Bellwied,[49] M. J. Betancourt,[22] R. R. Betts,[7] A. Bhasin,[16] A. K. Bhati,[29] H. Bichsel,[48] J. Bielcik,[9] J. Bielcikova,[10] B. Biritz,[5] L. C. Bland,[2] W. Borowski,[40] J. Bouchet,[18] E. Braidot,[26] A. V. Brandin,[25] A. Bridgeman,[1] S. G. Brovko,[4] E. Bruna,[51] S. Bueltmann,[28] I. Bunzarov,[17] T. P. Burton,[2] X. Z. Cai,[39] H. Caines,[51] M. Calderón de la Barca Sánchez,[4] D. Cebra,[4] R. Cendejas,[5] M. C. Cervantes,[41] Z. Chajecki,[27] P. Chaloupka,[10] S. Chattopadhyay,[46] H. F. Chen,[37] J. H. Chen,[39] J. Y. Chen,[50] L. Chen,[50] J. Cheng,[43] M. Cherney,[8] A. Chikanian,[51] K. E. Choi,[33] W. Christie,[2] P. Chung,[10] M. J. M. Codrington,[41] R. Corliss,[22] J. G. Cramer,[48] H. J. Crawford,[3] S. Dash,[12] A. Davila Leyva,[42] L. C. De Silva,[49] R. R. Debbe,[2] T. G. Dedovich,[17] A. A. Derevschikov,[31] R. Derradi de Souza,[6] L. Didenko,[2] P. Djawotho,[41] S. M. Dogra,[16] X. Dong,[21] J. L. Drachenberg,[41] J. E. Draper,[4] J. C. Dunlop,[2] L. G. Efimov,[17] M. Elnimr,[49] J. Engelage,[3] G. Eppley,[35] M. Estienne,[40] L. Eun,[30] O. Evdokimov,[7] R. Fatemi,[19] J. Fedorisin,[17] A. Feng,[50] R. G. Fersch,[19] P. Filip,[17] E. Finch,[51] V. Fine,[2] Y. Fisyak,[2] C. A. Gagliardi,[41] D. R. Gangadharan,[5] A. Geromitsos,[40] F. Geurts,[35] P. Ghosh,[46] Y. N. Gorbunov,[8] A. Gordon,[2] O. Grebenyuk,[21] D. Grosnick,[45] S. M. Guertin,[5] A. Gupta,[16] W. Guryn,[2] B. Haag,[4] O. Hajkova,[9] A. Hamed,[41] L-X. Han,[39] J. W. Harris,[51] J. P. Hays-Wehle,[22] M. Heinz,[51] S. Heppelmann,[30] A. Hirsch,[32] E. Hjort,[21] G. W. Hoffmann,[42] D. J. Hofman,[7] B. Huang,[37] H. Z. Huang,[5] T. J. Humanic,[27] L. Huo,[41] G. Igo,[5] P. Jacobs,[21] W. W. Jacobs,[14] C. Jena,[12] F. Jin,[39] J. Joseph,[18] E. G. Judd,[3] S. Kabana,[40] K. Kang,[43] J. Kapitan,[10] K. Kauder,[7] H. Ke,[50] D. Keane,[18] A. Kechechyan,[17] D. Kettler,[48] D. P. Kikola,[21] J. Kiryluk,[21] A. Kisiel,[47] V. Kizka,[17] A. G. Knospe,[51] D. D. Koetke,[45] T. Kollegger,[11] J. Konzer,[32] I. Koralt,[28] L. Koroleva,[15] W. Korsch,[19] L. Kotchenda,[25] V. Kouchpil,[10] P. Kravtsov,[25] K. Krueger,[1] M. Krus,[9] L. Kumar,[18] P. Kurnadi,[5] M. A. C. Lamont,[2] J. M. Landgraf,[2] S. LaPointe,[49] J. Lauret,[2] A. Lebedev,[2] R. Lednicky,[17] J. H. Lee,[2] W. Leight,[22] M. J. LeVine,[2] C. Li,[37] L. Li,[42] N. Li,[50] W. Li,[39] X. Li,[32] X. Li,[38] Y. Li,[43] Z. M. Li,[50] M. A. Lisa,[27] F. Liu,[50] H. Liu,[4] J. Liu,[35] T. Ljubicic,[2] W. J. Llope,[35] R. S. Longacre,[2] W. A. Love,[2] Y. Lu,[37] E. V. Lukashov,[25] X. Luo,[37] G. L. Ma,[39] Y. G. Ma,[39] D. P. Mahapatra,[12] R. Majka,[51] O. I. Mall,[4] L. K. Mangotra,[16] R. Manweiler,[45] S. Margetis,[18] C. Markert,[42] H. Masui,[21] H. S. Matis,[21] Yu. A. Matulenko,[31] D. McDonald,[35] T. S. McShane,[8] A. Meschanin,[31] R. Milner,[22] N. G. Minaev,[31] S. Mioduszewski,[41] A. Mischke,[26] M. K. Mitrovski,[11] B. Mohanty,[46] M. M. Mondal,[46] B. Morozov,[15] D. A. Morozov,[31] M. G. Munhoz,[36] M. Naglis,[21] B. K. Nandi,[13] T. K. Nayak,[46] P. K. Netrakanti,[32] L. V. Nogach,[31] S. B. Nurushev,[31] G. Odyniec,[21] A. Ogawa,[2] Oh,[33] Ohlson,[51] V. Okorokov,[25] E. W. Oldag,[42] D. Olson,[21] M. Pachr,[9] B. S. Page,[14] S. K. Pal,[46] Y. Pandit,[18] Y. Panebratsev,[17] T. Pawlak,[47] H. Pei,[7] T. Peitzmann,[26] C. Perkins,[3] W. Peryt,[47] S. C. Phatak,[12] P. Pile,[2] M. Planinic,[52] M. A. Ploskon,[21] J. Pluta,[47] D. Plyku,[28] N. Poljak,[52] A. M. Poskanzer,[21] B. V. K. S. Potukuchi,[16] C. B. Powell,[21] D. Prindle,[48] N. K. Pruthi,[29] P. R. Pujahari,[13] J. Putschke,[51] H. Qiu,[20] R. Raniwala,[34] S. Raniwala,[34] R. L. Ray,[42] R. Redwine,[22] R. Reed,[4] H. G. Ritter,[21] J. B. Roberts,[35] O. V. Rogachevskiy,[17] J. L. Romero,[4] A. Rose,[21] L. Ruan,[2] J. Rusnak,[10] N. R. Sahoo,[46] S. Sakai,[21] I. Sakrejda,[21] T. Sakuma,[22] S. Salur,[4] J. Sandweiss,[51] E. Sangaline,[4] A. Sarkar,[13] J. Schambach,[42] R. P. Scharenberg,[32] A. M. Schmah,[21] N. Schmitz,[23] T. R. Schuster,[11] J. Seele,[22] J. Seger,[8] I. Selyuzhenkov,[14] P. Seyboth,[23] E. Shahaliev,[17] M. Shao,[37] M. Sharma,[49] S. S. Shi,[50] Q. Y. Shou,[39] E. P. Sichtermann,[21] F. Simon,[23] R. N. Singaraju,[46] M. J. Skoby,[32] N. Smirnov,[51] H. M. Spinka,[1] B. Srivastava,[32] T. D. S. Stanislaus,[45] D. Staszak,[5] S. G. Steadman,[22] J. R. Stevens,[14] R. Stock,[11] M. Strikhanov,[25] B. Stringfellow,[32] A. A. P. Suaide,[36] M. C. Suarez,[7] N. L. Subba,[18] M. Sumbera,[10] X. M. Sun,[21] Y. Sun,[37] Z. Sun,[20] B. Surrow,[22] D. N. Svirida,[15] T. J. M. Symons,[21] A. Szanto de Toledo,[36] J. Takahashi,[6] A. H. Tang,[2] Z. Tang,[37] L. H. Tarini,[49] T. Tarnowsky,[24] D. Thein,[42] J. H. Thomas,[21] J. Tian,[39] A. R. Timmins,[49] D. Tlusty,[10] M. Tokarev,[17] V. N. Tram,[21] S. Trentalange,[5] R. E. Tribble,[41] Tribedy,[46] O. D. Tsai,[5] T. Ullrich,[2] D. G. Underwood,[1] G. Van Buren,[2] G. van Nieuwenhuizen,[22] J. A. Vanfossen, Jr.,[18] R. Varma,[13] G. M. S. Vasconcelos,[6] A. N. Vasiliev,[31] F. Videbæk,[2] Y. P. Viyogi,[46] S. Vokal,[17] M. Wada,[42] M. Walker,[22] F. Wang,[32] G. Wang,[5] H. Wang,[24] J. S. Wang,[20] Q. Wang,[32] X. L. Wang,[37] Y. Wang,[43] G. Webb,[19] J. C. Webb,[2] G. D. Westfall,[24] C. Whitten Jr.,[5] H. Wieman,[21] S. W. Wissink,[14] R. Witt,[44] W. Witzke,[19] Y. F. Wu,[50] Xiao,[43] W. Xie,[32] H. Xu,[20] N. Xu,[21] Q. H. Xu,[38] W. Xu,[5] Y. Xu,[37] Z. Xu,[2] L. Xue,[39] Y. Yang,[20] P. Yepes,[35] K. Yip,[2] I-K. Yoo,[33] M. Zawisza,[47] H. Zbroszczyk,[47] W. Zhan,[20] J. B. Zhang,[50] S. Zhang,[39] W. M. Zhang,[18] X. P. Zhang,[43] Y. Zhang,[21] Z. P. Zhang,[37] J. Zhao,[39] C. Zhong,[39] W. Zhou,[38] X. Zhu,[43] Y. H. Zhu,[39] R. Zoulkarneev,[17] and Y. Zoulkarneeva[17]

(STAR Collaboration)

[1]*Argonne National Laboratory, Argonne, Illinois 60439, USA*
[2]*Brookhaven National Laboratory, Upton, New York 11973, USA*
[3]*University of California, Berkeley, California 94720, USA*
[4]*University of California, Davis, California 95616, USA*
[5]*University of California, Los Angeles, California 90095, USA*
[6]*Universidade Estadual de Campinas, Sao Paulo, Brazil*
[7]*University of Illinois at Chicago, Chicago, Illinois 60607, USA*
[8]*Creighton University, Omaha, Nebraska 68178, USA*
[9]*Czech Technical University in Prague, FNSPE, Prague, 115 19, Czech Republic*
[10]*Nuclear Physics Institute AS CR, 250 68 Řež/Prague, Czech Republic*
[11]*University of Frankfurt, Frankfurt, Germany*
[12]*Institute of Physics, Bhubaneswar 751005, India*
[13]*Indian Institute of Technology, Mumbai, India*
[14]*Indiana University, Bloomington, Indiana 47408, USA*
[15]*Alikhanov Institute for Theoretical and Experimental Physics, Moscow, Russia*
[16]*University of Jammu, Jammu 180001, India*
[17]*Joint Institute for Nuclear Research, Dubna, 141 980, Russia*
[18]*Kent State University, Kent, Ohio 44242, USA*
[19]*University of Kentucky, Lexington, Kentucky, 40506-0055, USA*
[20]*Institute of Modern Physics, Lanzhou, China*
[21]*Lawrence Berkeley National Laboratory, Berkeley, California 94720, USA*
[22]*Massachusetts Institute of Technology, Cambridge, MA 02139-4307, USA*
[23]*Max-Planck-Institut für Physik, Munich, Germany*
[24]*Michigan State University, East Lansing, Michigan 48824, USA*
[25]*Moscow Engineering Physics Institute, Moscow Russia*
[26]*NIKHEF and Utrecht University, Amsterdam, The Netherlands*
[27]*Ohio State University, Columbus, Ohio 43210, USA*
[28]*Old Dominion University, Norfolk, VA, 23529, USA*
[29]*Panjab University, Chandigarh 160014, India*
[30]*Pennsylvania State University, University Park, Pennsylvania 16802, USA*
[31]*Institute of High Energy Physics, Protvino, Russia*
[32]*Purdue University, West Lafayette, Indiana 47907, USA*
[33]*Pusan National University, Pusan, Republic of Korea*
[34]*University of Rajasthan, Jaipur 302004, India*
[35]*Rice University, Houston, Texas 77251, USA*
[36]*Universidade de Sao Paulo, Sao Paulo, Brazil*
[37]*University of Science & Technology of China, Hefei 230026, China*
[38]*Shandong University, Jinan, Shandong 250100, China*
[39]*Shanghai Institute of Applied Physics, Shanghai 201800, China*
[40]*SUBATECH, Nantes, France*
[41]*Texas A&M University, College Station, Texas 77843, USA*
[42]*University of Texas, Austin, Texas 78712, USA*
[43]*Tsinghua University, Beijing 100084, China*
[44]*United States Naval Academy, Annapolis, MD 21402, USA*
[45]*Valparaiso University, Valparaiso, Indiana 46383, USA*
[46]*Variable Energy Cyclotron Centre, Kolkata 700064, India*
[47]*Warsaw University of Technology, Warsaw, Poland*
[48]*University of Washington, Seattle, Washington 98195, USA*
[49]*Wayne State University, Detroit, Michigan 48201, USA*
[50]*Institute of Particle Physics, CCNU (HZNU), Wuhan 430079, China*
[51]*Yale University, New Haven, Connecticut 06520, USA*
[52]*University of Zagreb, Zagreb, HR-10002, Croatia*

Dihadron azimuthal correlations containing a high transverse momentum (p_T) trigger particle are sensitive to the properties of the nuclear medium created at RHIC through the strong interactions occurring between the traversing parton and the medium, i.e. jet-quenching. Previous measurements revealed a strong modification to dihadron azimuthal correlations in Au+Au collisions with respect to p+p and d+Au collisions. The modification increases with the collision centrality, suggesting a path-length or energy density dependence to the jet-quenching effect. This paper reports STAR measurements of dihadron azimuthal correlations in mid-central (20-60%) Au+Au collisions at $\sqrt{s_{\rm NN}} = 200$ GeV as a function of the trigger particle's azimuthal angle relative to the event plane, $\phi_s = |\phi_t - \psi_{\rm EP}|$. The azimuthal correlation is studied as a function of both the trigger and associated particle p_T. The subtractions of the combinatorial background and anisotropic flow, assuming Zero

Yield At Minimum (ZYAM), are described. The correlation results are first discussed with subtraction of the even harmonic (elliptic and quadrangular) flow backgrounds. The away-side correlation is strongly modified, and the modification varies with ϕ_s, with a double-peak structure for out-of-plane trigger particles. The near-side ridge (long range pseudo-rapidity $\Delta\eta$ correlation) appears to drop with increasing ϕ_s while the jet-like component remains approximately constant. The correlation functions are further studied with subtraction of odd harmonic triangular flow background arising from fluctuations. It is found that the triangular flow, while responsible for the majority of the amplitudes, is not sufficient to explain the ϕ_s-dependence of the ridge or the away-side double-peak structure. The dropping ridge with ϕ_s could be attributed to a ϕ_s-dependent elliptic anisotropy, however, the physics mechanism of the ridge remains an open question. Even with a ϕ_s-dependent elliptic flow, the away-side correlation structure is robust. These results, with extensive systematic studies of the dihadron correlations as a function of ϕ_s, trigger and associated particle p_T, and the pseudo-rapidity range $\Delta\eta$, should provide stringent inputs to help understand the underlying physics mechanisms of jet-medium interactions in high energy nuclear collisions.

PACS numbers: 25.75.-q, 25.75.Dw

I. INTRODUCTION

Collisions at the Relativistic Heavy Ion Collider (RHIC) of Brookhaven National Laboratory have created a medium with properties that resemble a nearly perfect liquid of strongly interacting quarks and gluons [1–4]. This conclusion is based upon two pillars of evidence [5]: (i) the strong elliptic flow and (ii) jet-quenching– suppression of high transverse momentum (p_T) single hadron yields and dihadron correlations in heavy-ion collisions relative to elementary p+p interactions. While suppression of high p_T single hadron yields has limited sensitivity to the medium core, dihadron correlation measurements provide richer and more valuable information about the properties of the created medium [6–8]. There are several key observations that can be made from dihadron correlations with a high p_T trigger particle. (i) The correlated hadron yield at high p_T, while not much changed on the near side of the trigger particle (where azimuth difference between correlated and trigger particles $|\Delta\phi| < \pi/2$), is strongly suppressed on the away side (where $|\Delta\phi| > \pi/2$) [9]. This lends strong support to the partonic energy loss picture [10–12]. (ii) The correlated hadron yields at low p_T are strongly enhanced on both the near and away side [13]. In particular, the near-side enhancement is tied to long-range correlations in pseudo-rapidity – the ridge [13–15]. (iii) The away-side correlation broadens from peripheral to central collisions, and exhibits double peaks for select trigger and associated particle p_T ranges [13, 16, 17]. The double-peak structure is peculiar and may provide an opportunity to study the underlying physics mechanisms for partonic energy loss, such as gluon radiation [18, 19], Mach-cone shock-wave excitation [20–29], or simply the bulk medium response [30]. Three-particle jet-like correlation studies indicate that the double-peak emission pattern of correlated hadrons is characteristic of medium triangular flow [30] and/or Mach-cone shock-waves [31]. (iv) The away-side associated particles are partially equilibrated with the bulk medium in mid-central to central collisions, and a higher degree of equilibration is observed for particles which are more aligned back-to-back with the trigger particles [13, 17]. This observation may underscore the connection between the medium's path-length and partonic energy loss.

We study the path-length dependence of partonic energy loss in detail in non-central collisions where the overlap region between the two colliding nuclei is anisotropic: the size in the reaction-plane direction is shorter than that perpendicular to it. The reaction plane (RP) is defined by the beam direction and the line connecting the centers of two colliding nuclei. It can be estimated in non-central collisions by determining the azimuthal angle with the highest particle emission probability, using the fact that the particles have an elliptic emission pattern [32]. The estimated angle is called the event plane (EP) to emphasize that it is an experimental estimate of the reaction plane with finite resolution. By selecting the trigger particle direction with respect to the event plane, $\phi_s = |\phi_t - \psi_{\rm EP}|$ (where ϕ_t is the trigger particle azimuth and $\psi_{\rm EP}$ is the event-plane azimuth), we aim to select different path-lengths through the medium that the away-side parton traverses, providing differential information unavailable to inclusive jet-correlation measurements.

Previously, the Solenoidal Tracker at RHIC (STAR) experiment has performed an exploratory measurement of azimuthal correlations at high p_T with trigger particles in-plane ($\phi_s < \pi/4$) and out-of-plane ($\phi_s > \pi/4$) using non-central 20-60% Au+Au collisions [33]. The results hinted that the away-side correlation with out-of-plane trigger particles is more strongly suppressed than that with in-plane trigger particles. In this paper, we extend those measurements to finer bins in ϕ_s and to lower associated and trigger p_T ranges [34]. We also present inclusive jet-like correlation results from minimum bias d+Au collisions as a reference to the Au+Au data. We further study the ridge as a function of ϕ_s, and investigate the systematics of the ridge in an attempt to further identify the underlying physics mechanism for the formation of the ridge. The highlights of the results have been published in Ref. [35]. This paper provides extensive results and analysis details. Similar results on the event-plane dependent dihadron correlations have been recently reported by the PHENIX collaboration [36].

The paper is organized as follows. In Sec. II we describe in detail our data analysis of dihadron correlations relative to the event plane. In Sec. III we discuss our extensive studies of the systematic uncertainties of our results. In Sec. IV we report and discuss our results of dihadron correlations relative to the event plane. We finally conclude in Sec. V. We present all raw and background-subtracted dihadron correlation functions relative to the event plane in Appendix C.

II. EXPERIMENT AND DATA ANALYSIS

The data used in this analysis were taken by the STAR experiment [37] at RHIC at the nucleon-nucleon center of mass energy of $\sqrt{s_{\rm NN}}$ = 200 GeV. The minimum-bias Au+Au data were from Run IV in 2004 at RHIC. The reference minimum-bias d+Au data used for comparison were from Run III in 2003. The minimum-bias triggers for Au+Au and d+Au collisions were provided by the Central Trigger Barrel [38] and the Zero Degree Calorimeters [39].

The details of the STAR experiment can be found in Ref. [37]. The main detector used for this analysis is the Time Projection Chamber (TPC) [40, 41]. The TPC is surrounded by a solenoidal magnet providing a nearly uniform magnetic field of 0.5 Tesla along the beam direction. Particle tracks are reconstructed in the TPC. The primary event vertex was fit using reconstructed tracks which pass certain quality cuts. Events with a primary vertex within ±30 cm of the geometric center of the TPC along the beam axis are used in the analysis. With this range of primary vertex position, the TPC has good acceptance within the pseudo-rapidity region of $|\eta| \leq 1.1$. The Au+Au collision centrality is defined according to the measured charged hadron multiplicity in the TPC within $|\eta| < 0.5$ (reference multiplicity) [42]. We choose the 20-60% centrality data for our analysis where good event-plane resolution is achieved (see later).

In our analysis, only tracks that extrapolate to within 2 cm of the primary vertex are used. Tracks are required to be reconstructed with at least 20 out of a maximum of 45 hits in the TPC. The ratio of the number of hits used in track reconstruction to the number of possible hits is required to be greater than 0.51 to eliminate multiple track segments being reconstructed from a single particle trajectory. The same event and track cuts are applied to particle tracks used for event-plane reconstruction and for the subsequent correlation analysis. Particle tracks within $|\eta| < 1$ are used in the correlation analysis.

High p_T particles are selected as triggers off-line to perform the correlation analyses. We select high p_T trigger particles within the $p_T^{(t)}$ ranges of 3-4 GeV/c and 4-6 GeV/c. A total of 4.4 million Au+Au events with centrality ranging from 20-60% are used in this analysis. From the event sample we find 2.1 million trigger particles with p_T values ranging between 3-4 GeV/c and 0.36 million trigger particles with p_T values between 4-6 GeV/c. Associated particles, i.e. all particles in the event including those correlated with the trigger particles, are grouped into the $p_T^{(a)}$ ranges of 0.15-0.5, 0.5-1.0, 1.0-1.5, 1.5-2.0, 2.0-3.0 (or 2.0-4.0) GeV/c. The low $p_T^{(a)}$ cut-off of 0.15 GeV/c was imposed by the magnetic field strength and the TPC aperture. The azimuthal correlation functions in $\Delta\phi$ (azimuthal angle difference between associated particle and trigger particle) are analyzed separately for trigger particles at different azimuthal angles (ϕ_s) relative to the event plane.

The associated particle yields are corrected for single-particle track reconstruction efficiency which is obtained from embedding simulated tracks into real events [43]. It depends on both centrality and p_T. The efficiency is found to be insensitive to η and is therefore averaged over η. The ϕ-dependent part of the acceptance and track reconstruction efficiency are corrected for both the trigger and associated particle yields. This ϕ-dependent correction is obtained from the inverse of the single-particle ϕ distribution whose average is normalized to unity. Correction for the ϕ-dependent efficiencies for both trigger and associated particles removes the majority of the non-uniformity caused by the TPC sector boundaries. The remaining non-uniformity in $\Delta\phi$ is corrected by using an event-mixing technique, where the trigger particle from one event is paired with associated particles from another event within the same centrality bin [13]. The two-particle acceptance in $\Delta\eta$ (pseudo-rapidity difference between associated particle and trigger particle), which is approximately triangle-shaped in $\Delta\eta$, is not corrected to be consistent with earlier publications [13]. The correlation function is normalized by the corrected number of trigger particles in its corresponding ϕ_s bin. The centrality and p_T dependent aspects of the trigger particle efficiency cancel out in the normalization.

Tracks that are spatially near each other can be combined into a single reconstructed track due to merged space points of ionization in the STAR TPC. This track merging results in a pair inefficiency at $\Delta\eta \sim 0$ and small, but finite $\Delta\phi$ whose value depends on the magnetic field polarity, charge combination and the p_T's of the trigger and associated particles [15]. The track merging effect is most significant in central collisions where the TPC hit occupancy is high. The track merging effect in our centrality range of 20-60% is negligible.

A. Event-Plane Reconstruction

We use the second Fourier harmonic in azimuthal angle to determine the event-plane angle $\psi_{\rm EP}$ [32], which is not identical to the real reaction-plane angle ($\psi_{\rm RP}$). The event plane is an estimate, with finite resolution, of the second harmonic participant plane (the plane defined by the beam direction and the minor axis of the overlap geometry of participant nucleons) [44]. The participant plane angle, ψ_2, fluctuates about the reaction plane direction. The particles used to determine the

event plane are below $p_T = 2$ GeV/c. To avoid self-correlations, particles from the p_T bin that is used in the correlation analysis are excluded from event-plane reconstruction. For example, for the associated particle p_T bin of $1.0 < p_T^{(a)} < 1.5$ GeV/c, the particles used to calculate the event plane are from p_T ranges of $0.15 < p_T < 1.0$ GeV/c plus $1.5 < p_T < 2.0$ GeV/c. We use the p_T-weight method [32] which gives better event-plane resolution due to the stronger anisotropy at larger p_T. The slight non-uniform efficiency and acceptance in azimuthal angle were corrected as mentioned previously in the event-plane reconstruction. Figure 1 shows examples of the constructed event plane azimuthal angle distributions. As seen from the figure, the constructed event plane $\psi_{\rm EP}$ distribution is approximately uniform. We weight the events by the inverse of the event-plane angle distributions in Fig. 1 in our correlation analysis. However, we found negligible difference in our results with and without this event-plane weighting.

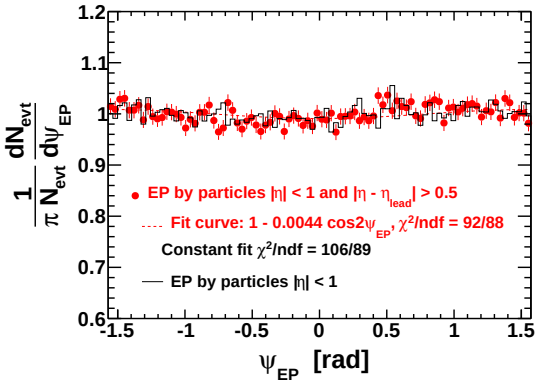

FIG. 1: (Color online) Constructed event plane azimuthal angle ($\psi_{\rm EP}$) distributions by the modified reaction-plane (MRP) method (points) and the traditional reaction-plane method (histogram). The particles used for constructing the event plane shown in this figure are from $0.15 < p_T < 1$ GeV/c or $1.5 < p_T < 2$ GeV/c, to be used for correlation analysis for the associated particle $p_T^{(a)}$ bin of $1 < p_T^{(a)} < 1.5$ GeV/c.

Nonflow correlations, such as di-jets, can influence the determination of the event plane. To reduce this effect, we exclude from EP reconstruction particles within pseudorapidity difference of $|\Delta\eta| = |\eta - \eta_{\rm trig}| < 0.5$ from the trigger particle. This method is called the modified reaction-plane (MRP) method [45]. The traditional reaction-plane method, on the other hand, does not exclude from EP reconstruction those particles in the η vicinity of the trigger particle. Remaining possible biases due to correlations between trigger particles and EP particles may be assessed by comparing our results relative to the EP reconstructed from these two different methods with their respective EP resolutions. The results are found qualitatively similar, suggesting that any biases may be small. See Appendix A for details.

To extract the near-side jet-like component, we use the difference in azimuthal correlations between analyzed at small and large $|\Delta\eta|$. The MRP method, which excludes particles within $|\Delta\eta| < 0.5$ of the trigger particle in the event, would have different systematic biases on the $\Delta\phi$ correlations at small and large $|\Delta\eta|$. Thus, we use the traditional reaction-plane method for the jet-like component. Figure 1 shows the $\psi_{\rm EP}$ distributions from the modified reaction-plane method (data points) and the traditional reaction-plane method (histogram). We have checked the correlation between the event plane angles constructed from the traditional method and the MRP method, and found they are correlated as expected.

We divide our data into six equal-size slices of trigger particle azimuthal angle relative to the event plane, ϕ_s, and analyze azimuthal correlations separately in each slice. Figure 2 shows a schematic view, with the slices numerically labeled 1 to 6 corresponding to $\phi_s = |\phi_t - \psi_{\rm EP}| = 0$-$\pi/12$, $\pi/12$-$\pi/6$, $\pi/6$-$\pi/4$, $\pi/4$-$\pi/3$, $\pi/3$-$5\pi/12$, and $5\pi/12$-$\pi/2$. We form azimuthal correlations with trigger particles in each slice separately. Figure 3 shows, as examples, the raw azimuthal correlations in 20-60% Au+Au collisions for six slices in ϕ_s for trigger and associated particle p_T ranges of $3 < p_T^{(t)} < 4$ GeV/c and $1 < p_T^{(a)} < 2$ GeV/c (upper panel), and $4 < p_T^{(t)} < 6$ GeV/c and $2 < p_T^{(a)} < 4$ GeV/c (lower panel), respectively. All raw correlation functions are presented in Figs. 27, 28, 29, and 30 in Appendix C as a function of trigger $p_T^{(t)}$, associated $p_T^{(a)}$, and ϕ_s.

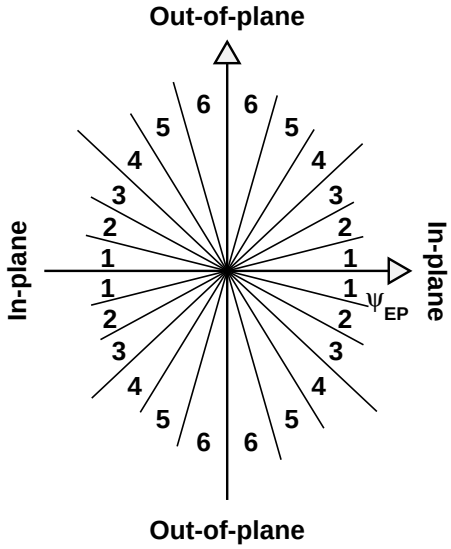

FIG. 2: Sketch of six slices in trigger particle azimuthal angle relative to the event plane, $\phi_s = |\phi_t - \psi_{\rm EP}|$.

B. Elliptic and Quadrangular Flow Background

The correlation structure sits atop a large combinatorial background. The background has a flow modula-

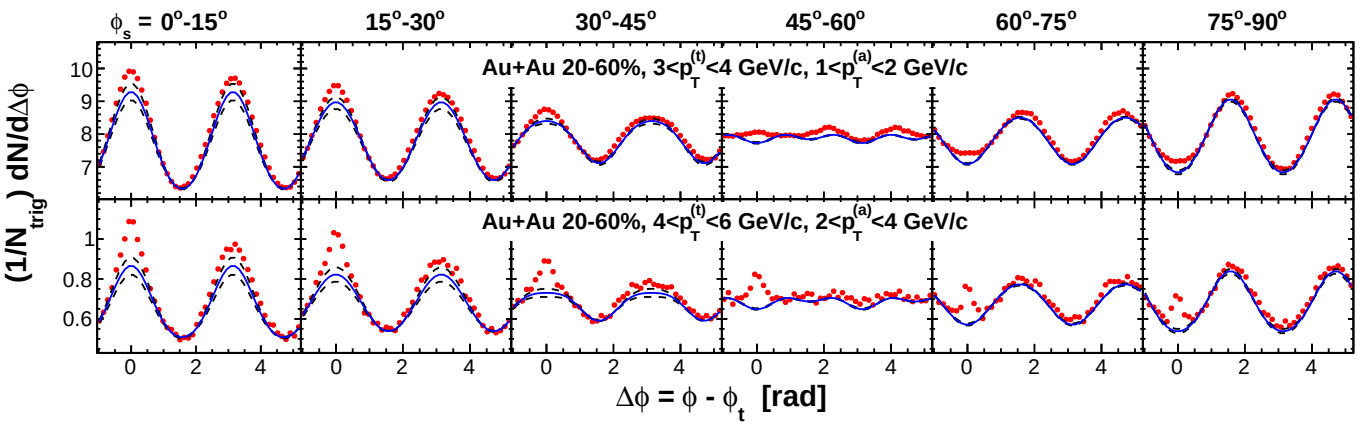

FIG. 3: (Color online) Raw dihadron $\Delta\phi$ correlations with trigger particles in six slices of azimuthal angle relative to the event plane, $\phi_s = |\phi_t - \psi_{\rm EP}|$. The data are from minimum-bias 20-60% Au+Au collisions. The trigger and associated particle p_T ranges are $3 < p_T^{(t)} < 4$ GeV/c and $1 < p_T^{(a)} < 2$ GeV/c (upper panel), and $4 < p_T^{(t)} < 6$ GeV/c and $2 < p_T^{(a)} < 4$ GeV/c (lower panel), respectively. Note the lower panels correspond to the kinematic range used in Ref. [9]. Both the trigger and associated particles are restricted to within $|\eta| < 1$. The triangle two-particle $\Delta\eta$ acceptance is not corrected. Statistical errors are smaller than the symbol size. The raw data in the upper panels have been published in Ref. [35]. The curves are flow modulated ZYAM background including v_2 and $v_4\{\psi_2\}$ by Eq. (1). The used v_2 values are given in Table I from four-particle $v_2\{4\}$ and two-particle $v_2\{2, \eta_{\rm gap}{=}0.7\}$ (dashed curves) and the average v_2 from the two methods (solid curve). The $v_4\{\psi_2\}$ is taken from the parameterization in Eq. (15).

tion induced by the anisotropies of the trigger particle and the background particles with respect to the participant plane [46]. In this analysis we use anisotropic flow parameters measured by two- and multi-particle cumulants [32] for the combinatorial background. An alternative approach that has been used to describe dihadron correlation data treats the anisotropic flow modulations as free parameters in a multi-parameter model fit to the dihadron correlation functions in 2-dimensional $\Delta\eta$-$\Delta\phi$ space [47, 48]. Results from this alternative approach to the inclusive dihadron correlation data (without a high-p_T trigger or cutting on ϕ_s) can be found in Ref. [47, 48]. The multi-parameter fit approach to our ϕ_s-dependent high-p_T triggered dihadron correlations is considered in Sec. III E, but a detailed discussion of the differences in assumptions and conclusions of the two approaches is beyond the scope of this paper.

In this analysis, first, only the v_2 and v_4 harmonic flow backgrounds are considered. The triangular harmonic flow background and other high-order effects are described in the next subsection, Section II C. Only considering the v_2 and v_4 harmonics, the flow correlated background is given by [49]

$$\frac{dN}{d\Delta\phi} = B\left[1 + 2v_2^{(a)}v_2^{(t,R)}\cos(2\Delta\phi) + 2v_4^{(a)}\{\psi_2\}v_4^{(t,R)}\{\psi_2\}\cos(4\Delta\phi)\right], \quad (1)$$

where B is the background normalization. In Eq. (1) $v_2^{(a)}$ and $v_4^{(a)}\{\psi_2\}$ are the associated particle's second and fourth harmonics with respect to the second harmonic event plane, ψ_2, and $v_2^{(t,R)}$ and $v_4^{(t,R)}\{\psi_2\}$ are the average harmonics of the trigger particles, $v_2^{(t,R)} = \langle\cos\left[2\left(\phi_t - \psi_2\right)\right]\rangle^{(R)}$ and $v_4^{(t,R)}\{\psi_2\} = \langle\cos\left[4\left(\phi_t - \psi_2\right)\right]\rangle^{(R)}$, respectively. The superscript '(R)' indicates that the averages are taken within the ϕ_t region of a slice of width $2c$ at ϕ_s: $\phi_s - c < |\phi_t - \psi_{\rm EP}| < \phi_s + c$ (where $c = \pi/24$ in our analysis). Note that we have used ϕ_s here and in Eq. (3) to be the center value of a $|\phi_t - \psi_{\rm EP}|$ bin, while elsewhere we simply use $\phi_s = |\phi_t - \psi_{\rm EP}|$ to indicate a narrow bin in $|\phi_t - \psi_{\rm EP}|$. For the $n^{\rm th}$ harmonic anisotropy we have [49],

$$v_n^{(R)} = \frac{v_n^{(\rm t)} + \delta_{n,\rm even}T_n + \sum_{k=2,4,6,\ldots}\left(v_{k+n}^{(\rm t)} + v_{|k-n|}^{(\rm t)}\right)T_k}{1 + \sum_{k=2,4,6,\ldots}2v_k^{(\rm t)}T_k}. \quad (2)$$

Here T_k is a short-hand notation for

$$T_k = \cos(k\phi_s)\frac{\sin(kc)}{kc}\langle\cos(k\Delta\psi)\rangle, \quad (3)$$

$\langle\cos(k\Delta\psi)\rangle \equiv \langle\cos k(\psi_{\rm EP} - \psi_2)\rangle$ is the event-plane res-

olution with respect to the $k^{\rm th}$ harmonic, and δ is Kronecker's delta. Since the correlation signal we are studying is on the order of a few percent of the background, we need to keep the flow correction in Eq. (2) up to the order $v_2 v_4 \sim 0.1\%$. Keeping terms for $v_2^{(t,R)}$ up to v_4 and for $v_4^{(t,R)}\{\psi_2\}$ up to v_2, we have

$$v_2^{(t,R)} \approx \frac{T_2 + (1+T_4)v_2^{(t)} + (T_2+T_6)v_4^{(t)}\{\psi_2\}}{1 + 2T_2 v_2^{(t)} + 2T_4 v_4^{(t)}\{\psi_2\}}\,, \quad (4)$$

and

$$\begin{aligned} v_4^{(t,R)}\{\psi_2\} &\approx \frac{T_4 + (T_2+T_6)v_2^{(t)} + (1+T_8)v_4^{(t)}\{\psi_2\}}{1 + 2T_2 v_2^{(t)} + 2T_4 v_4^{(t)}\{\psi_2\}} \\ &\approx \frac{T_4 + (T_2+T_6)v_2^{(t)}}{1 + 2T_2 v_2^{(t)}}\,. \end{aligned} \quad (5)$$

Note the $v_4^{(t)}\{\psi_2\}$ above is with respect to the second harmonic plane ψ_2. The final flow correction is given by Eqs. (1), (4), and (5).

The event-plane resolutions, $\langle\cos(k\Delta\psi)\rangle$ ($k = 2, 4, 6$), are obtained from the sub-event method [32]. The event is randomly divided into two sub-events a and b with equal multiplicities. The sub-events, excluding the associated particle p_T region, are analyzed to yield event-plane angles which, ideally, should be identical. The difference between the obtained event-plane angles, $\psi_a - \psi_b$, gives the uncertainty in the event-plane determination of the sub-events [32]

$$\langle\cos(k\Delta\psi)\rangle_{\text{sub-event}} = \sqrt{\langle\cos k(\psi_a - \psi_b)\rangle}. \quad (6)$$

The event-plane resolution of the full event can be approximated by [32]

$$\langle\cos(k\Delta\psi)\rangle \approx \sqrt{2}\langle\cos(k\Delta\psi)\rangle_{\text{sub-event}} \quad (7)$$

in the limit of small event-plane resolution. The factor $\sqrt{2}$ comes in because the multiplicities of the sub-events are smaller than the full event multiplicity by a factor of 2. We use the approximate form of Eq. (7) to assess systematic uncertainties in the event-plane resolutions by different ways of dividing the event into sub-events (see Sec. III B).

The precise form of the event-plane resolution of the full event is given by [32]

$$\langle\cos(k\Delta\psi)\rangle = \sqrt{\frac{\pi}{2}}\left(\frac{\chi_k}{2}\right) e^{-\frac{\chi_k^2}{4}} \left[I_0\left(\frac{\chi_k^2}{4}\right) + I_1\left(\frac{\chi_k^2}{4}\right)\right] \quad (8)$$

where

$$\chi_k(N) = v_k\sqrt{2N}\frac{\langle p_T\rangle}{\sqrt{\langle p_T^2\rangle}} \quad (9)$$

depends on the harmonic anisotropy magnitude v_k and the number of particles N used in event-plane reconstruction. The p_T enters into Eq. (9) because we weighted each particle by its p_T in constructing the event plane. In data analysis we solve for the sub-event $\chi_k(N/2)$ by Eq. (8) and the known event-plane resolution of the sub-events from Eq. (6) employing an iterative procedure [32]. From Eq. (9) we obtain the full event $\chi_k(N) = \sqrt{2}\chi_k(N/2)$. We then use Eq. (8) to determine the event-plane resolution of the full event [32]. The event-plane resolutions are listed in Table I. The resolutions depend on the p_T bin because particles in a given p_T bin (to be used for correlation analysis) are excluded from the event-plane reconstruction to avoid self-correlations as aforementioned.

One would naively expect that the event-plane resolution should be different for different trigger particle orientations from the event plane because the influence of di-jets on the event-plane determination should vary: a di-jet aligned with the reaction plane enhances the event-plane reconstruction resulting in a better resolution, whereas a di-jet perpendicular to the reaction plane reduces the accuracy of the constructed event plane resulting in a poorer resolution. However, this is a post effect due to the selection of the trigger particle angle relative to the event plane. The resolutions used in Eq. (1), on the other hand, are those of all triggered events before any selection of the trigger particle orientation is made. We have also verified this with Monte Carlo toy model simulations.

Since only triggered events enter into our correlation measurements, the event-plane resolutions are measured using only these events. The event-plane resolutions from inclusive events (minimum-bias events within the given centrality bin) are found to be within a couple of percent of that from the triggered events (see systematic uncertainty discussion in Sec. III B).

We analyzed the elliptic flow in each of the p_T bins used in our correlation analysis. The obtained elliptic flow parameters are tabulated in Table I together with their systematic uncertainties. The analysis of the elliptic flow and the assessment of its systematic uncertainty are both described in Sec. III A. We used these v_2 parameters for background subtraction. The calculated magnitudes of the elliptic flow modulation, $2v_2^{(a)}v_2^{(t,R)}$, are listed in Table II together with their systematic uncertainties. The calculated background curves are superimposed in Fig. 3.

As mentioned previously, our trigger particle p_T ranges are $3 < p_T^{(t)} < 4$ GeV/c and $4 < p_T^{(t)} < 6$ GeV/c. In elementary p+p and d+Au collisions, the particles in these p_T ranges originate mainly from hard-scatterings and jets. In relativistic heavy ion colllisions, however, a large baryon to meson ratio was observed in the p_T region around 3 GeV/c [50, 51]. The reason for the large ratio and the sources of those high p_T particles are still under debate. The coalescence and recombination models [52–54] can elegantly explain the large baryon to meson ratio from a thermal bath of constituent quarks. On the other hand, the jet-like correlations at small angles relative to trigger particles of $p_T^{(t)} > 3$ GeV/c, with the long range ridge correlation removed, are measured

TABLE I: Elliptic flow and event-plane resolutions as a function of p_T in 20-60% minimum-bias Au+Au collisions. The resolutions depend on the p_T bin because particles in a given p_T bin are excluded from the event-plane reconstruction to avoid self-correlations. The errors on v_2 are systematic uncertainties given by two-particle $v_2\{2, \eta_{\rm gap}{=}0.7\}$ (with a reference particle $0.15 < p_T < 2$ GeV/c) and four-particle $v_2\{4\}$ (with three reference particles). Systematic uncertainties on the resolutions are negligible.

p_T (GeV/c)	v_2	$\langle\cos(2\Delta\psi)\rangle$	$\langle\cos(4\Delta\psi)\rangle$	$\langle\cos(6\Delta\psi)\rangle$
0.15 - 0.5	0.038 ± 0.003	0.673	0.324	0.127
0.5 - 1	0.082 ± 0.006	0.596	0.247	0.082
1 - 1.5	0.128 ± 0.010	0.637	0.286	0.104
1.5 - 2	0.164 ± 0.011	0.676	0.328	0.129
2 - 3	0.189 ± 0.012	0.704	0.360	0.150
3 - 4	0.194 ± 0.013			
4 - 6	0.163 ± 0.020			

TABLE II: The elliptic flow modulation in the correlation background, $2v_2^{(a)}v_2^{(t,R)}$, calculated using measurements in Table I, as a function of $p_T^{(a)}$ (in rows) and $\phi_s = |\phi_t - \psi_{\rm EP}|$ (in columns) in minimum-bias 20-60% Au+Au collisions. Both trigger particle p_T ranges of $3 < p_T^{(t)} < 4$ GeV/c and $4 < p_T^{(t)} < 6$ GeV/c are listed. Quoted errors are systematic uncertainties. Note the significantly smaller systematic uncertainties out-of-plane than in-plane.

$p_T^{(a)}$ (GeV/c)	$0-\pi/12$	$\pi/12-\pi/6$	$\pi/6-\pi/4$	$\pi/4-\pi/3$	$\pi/3-5\pi/12$	$5\pi/12-\pi/2$
			$3 < p_T^{(t)} < 4$ GeV/c			
0.15 - 0.5	0.0544 ± 0.0046	0.0433 ± 0.0039	0.0229 ± 0.0025	−0.0028 ± 0.0006	−0.0270 ± 0.0015	−0.0416 ± 0.0028
0.5 - 1	0.1098 ± 0.0096	0.0884 ± 0.0082	0.0490 ± 0.0055	−0.0004 ± 0.0018	−0.0466 ± 0.0022	−0.0745 ± 0.0045
1 - 1.5	0.1793 ± 0.0149	0.1435 ± 0.0128	0.0776 ± 0.0085	−0.0054 ± 0.0024	−0.0831 ± 0.0042	−0.1301 ± 0.0081
1.5 - 2	0.2376 ± 0.0178	0.1892 ± 0.0152	0.0999 ± 0.0100	−0.0128 ± 0.0025	−0.1186 ± 0.0057	−0.1825 ± 0.0105
2 - 3	0.2814 ± 0.0194	0.2233 ± 0.0166	0.1159 ± 0.0108	−0.0199 ± 0.0024	−0.1473 ± 0.0067	−0.2243 ± 0.0121
			$4 < p_T^{(t)} < 6$ GeV/c			
0.15 - 0.5	0.0535 ± 0.0047	0.0421 ± 0.0041	0.0213 ± 0.0028	−0.0045 ± 0.0008	−0.0284 ± 0.0013	−0.0427 ± 0.0026
0.5 - 1	0.1073 ± 0.0101	0.0853 ± 0.0088	0.0451 ± 0.0062	−0.0045 ± 0.0025	−0.0502 ± 0.0017	−0.0777 ± 0.0041
1 - 1.5	0.1758 ± 0.0156	0.1390 ± 0.0136	0.0717 ± 0.0095	−0.0115 ± 0.0034	−0.0883 ± 0.0035	−0.1344 ± 0.0074
1.5 - 2	0.2337 ± 0.0186	0.1838 ± 0.0162	0.0928 ± 0.0113	−0.0201 ± 0.0038	−0.1246 ± 0.0048	−0.1872 ± 0.0097
2 - 3	0.2773 ± 0.0202	0.2174 ± 0.0177	0.1080 ± 0.0123	−0.0280 ± 0.0039	−0.1537 ± 0.0057	−0.2291 ± 0.0113

to be invariant from p+p, d+Au, peripheral to central Au+Au collisions [55], and independent of the reaction plane direction in Au+Au collisions as will be shown in this work. These experimental evidences strongly suggest that those $p_T^{(t)} > 3$ GeV/c particles are mostly of jet origin in Au+Au collisions just as in p+p and d+Au collisions. It is possible that recombination may still be at work in our trigger particle p_T ranges, but in such a fashion that the parton(s) prior to recombination have already imprinted angular correlations related to the hard-scatterings [56].

Different sources, such as the recombination [52–54] and jet fragmentation discussed above, will likely give different anisotropies to those high p_T particles. However, the anisotropy of the trigger particles to be used in the background subtraction in Eqs. (1), (2), (4), and (5) should be the experimentally measured net anisotropy [57], as we have done in this work, irrespective of the different origins.

C. Triangular and High-Order Harmonic Flow Background

In Eq. (1) we have neglected the odd harmonic terms, such as $2v_1^{(a)}v_1^{(t,R)}\cos(\Delta\phi)$ and $2v_3^{(a)}v_3^{(t,R)}\cos(3\Delta\phi)$. Due to symmetry at mid-rapidity, the averages of the odd harmonic coefficients v_1, v_3, and etc. vanish. However, their fluctuations would yield non-vanishing averages of the products of $v_1^{(a)}v_1^{(t)}$ and $v_3^{(a)}v_3^{(t)}$, thereby contributing to the background in the dihadron correlations. If one assumes that the amplitude of the v_1 (directed flow) fluctuations is of the same order of magnitude as the maximum v_1 in our pseudorapidity range (which was measured to be small [58]), then the v_1 fluctuation contribution can be neglected [59, 60]. In the present work we neglect any direct flow fluctuation effect in our background subtraction. More recent developments [61, 62] in the understanding of initial geometry fluctuations, however, suggest that v_1 fluctuation effects (sometimes called rapidity-even v_1)

may not be small as originally thought [59, 60]. We remark in Sec. IV F on the magnitude of the possible v_1 fluctuation effects using recent measurements.

Note that the possible effect of statistical global momentum conservation can generate a negative dipole [63] which has the same shape as the v_1 fluctuation effect. However, the statistical momentum conservation effect is not from v_1 fluctuations, but part of the correlation signal, same as momentum conservation by any other mechanisms, such as dijet production.

It has been shown that the initial fluctuations in the overlap geometry (spatial distribution of participating nucleons) gives rise to v_3 (triangular flow) fluctuations [30, 64, 65]. It was found from the Monte Carlo Glauber model [66] that the triangularity due to geometry fluctuations can be comparable to the magnitude of the eccentricity which is connected to the elliptic flow [30]. It is thus possible that large triangular flow fluctuations can arise which would give triangular peaks in the flow background [30, 64, 65]. This appears to be the case in the AMPT (A Multi-Phase Transport) model and the UrQMD (Ultrarelativistic Quantum Molecular Dynamics) model studied in Ref. [30, 67, 68] and [65], respectively. Hydrodynamic calculations with event-by-event geometry fluctuations confirm that sizeable v_3 can be generated from initial geometry fluctuations [69–73]. The v_3 magnitude is smaller than that of v_2 despite of the similar initial triangular and elliptic eccentricities of ϵ_3 and ϵ_2, respectively. This is likely due to the larger damping power of shear viscosity on v_3 than on v_2 [69–72, 74].

Since the orientation of the triangular overlap shape due to fluctuations is random relative to the event-plane direction [75, 76], determined by the elliptic anisotropy, the effect of any triangular flow is independent of the event plane. In other words, the triangular flow background would be proportional to $2v_3^{(a)}v_3^{(t,R)}\cos(3\Delta\phi) = 2v_3^{(a)}v_3^{(t)}\cos(3\Delta\phi)$ independent of ϕ_s. With triangular flow, the flow background of Eq. (1) becomes

$$\frac{dN}{d\Delta\phi} = B\left[1 + 2v_2^{(a)}v_2^{(t,R)}\cos(2\Delta\phi) + 2v_4^{(a)}\{\psi_2\}v_4^{(t,R)}\{\psi_2\}\cos(4\Delta\phi) + 2v_3^{(a)}v_3^{(t)}\cos(3\Delta\phi)\right]. \tag{10}$$

We may estimate the effect of triangular flow fluctuations in our correlation measurements. The AMPT and UrQMD models indicate that in the 20-60% centrality range the triangular flow fluctuation effect is about 10% of the elliptic flow for our trigger and associated p_T bins, $v_3^2/v_2^2 \approx 0.1$ [30, 65, 77]. Event-by-event hydrodynamic calculations yield a similar magnitude of v_3^2/v_2^2 [78]. Experimental data on inclusive two-particle correlations at $p_T > 2$ GeV/c indicate a ratio of the harmonic coefficients also of the magnitude $v_3^2/v_2^2 \approx 0.1$ within 20-60% centrality [79]. More recent measurements on triangular anisotropy are consistent with these estimates [80, 81]. This suggests that the measured third harmonic term in the inclusive two-particle correlations at low p_T may be dominated by triangular flow fluctuations, just as the second harmonic term dominated by elliptic flow. As we will show in Sec. IV C, the effect of the triangular flow of this magnitude is sizeable in our dihadron correlation measurements with high p_T trigger particles as well. In the main work of our study of high-p_T dihadron correlations relative to the EP, we do not include the possible contributions from v_3 anisotropy in the flow background subtraction. In Sec. IV F we discuss the effect of the presently measured v_3 on our dihadron correlation results.

So far only the v_4 contribution correlated with the second harmonic plane ψ_2 has been considered as in Eq. (1). This part of v_4 is referred to $v_4\{\psi_2\}$. The other part of v_4 arises from fluctuations and is uncorrelated to $\psi_{\rm EP}$. We refer to this part as $V_4\{\rm uc\}$. The flow background is then given by

$$\frac{dN}{d\Delta\phi} = B\left[1 + 2v_2^{(a)}v_2^{(t,R)}\cos(2\Delta\phi) + 2v_4^{(a)}\{\psi_2\}v_4^{(t,R)}\{\psi_2\}\cos(4\Delta\phi) + 2v_3^{(a)}v_3^{(t)}\cos(3\Delta\phi) + 2V_4\{\rm uc\}\cos(4\Delta\phi)\right]. \tag{11}$$

Section IV F discusses how $V_4\{\rm uc\}$ is obtained in the present analysis.

Glauber model [66] calculations also show that the quadrangularity, pentagonality, and hexagonality due to geometry fluctuations equal to the triangularity, all large and comparable to the eccentricity [77, 82]. However, it was suggested that those higher order eccentricities were inefficient to generate sizeable high-order harmonic flow in final state momentum space [77]. Experimental data also indicate that the magnitudes and fluctuations of v_4

and v_6 are small relative to the magnitude of v_2 [83]. Although we include $V_4\{\mathrm{uc}\}$ in our flow background of Eq. (11), the effect of $V_4\{\mathrm{uc}\}$ is small as will be discussed in Sec. IV F. It is safe to neglect v_5^2 and the higher order anisotropic fluctuation terms in the flow background of Eq. (1).

D. Background Normalization by ZYAM

The flow correlated backgrounds given by Eq. (1), as an example, are shown in Fig. 3 as solid curves. The background curves have been normalized assuming that the background-subtracted signal has Zero Yield At Minimum (ZYAM) [13, 84]. To obtain the ZYAM normalization factor, we fold the raw correlation function to within the range of $0 < \Delta\phi < \pi$ because of the symmetry of the correlation function. We take the ratio of the folded raw correlation to the background curve of Eq. (1), where B is set to unity before taking the ratio. We obtain a continuous range of the size of $\pi/6$ where the average ratio is the smallest. This smallest average ratio is the normalization factor B to be used in the flow background of Eq. (1), which is then subtracted from the raw correlation function to obtain the final correlation signal.

The background levels can be different for the different ϕ_s slices because of the net effect of the variations in jet-quenching with ϕ_s and the centrality cuts in total charged particle multiplicity in the TPC within $|\eta| < 0.5$. Thus, in our correlation analysis, the background level B is treated independently in individual ϕ_s slices. In the recent proposal [85] to fit the ϕ_s-dependent near-side correlations at large $\Delta\eta$ (i.e. the ridge region) by Fourier coefficients and treat them as backgrounds, the background level B is required to be the same in all ϕ_s slices.

Table III lists the obtained background level B as a function of ϕ_s and $p_T^{(a)}$ in 20-60% Au+Au collisions. Results from both trigger particle p_T ranges of $3 < p_T^{(t)} < 4$ GeV/c and $4 < p_T^{(t)} < 6$ GeV/c are listed. The background levels listed are not only for the correlation functions with the $|\Delta\eta| < 2$ region within our acceptance, but also for those in the large $\Delta\eta$ region of $|\Delta\eta| > 0.7$. The latter is used for the ridge studies (see Sec. IV C). One notices that the background level for the lower trigger particle $p_T^{(t)}$ range is slightly larger. This is due to the fact that relatively more events contain multiple jets with the lower trigger particle $p_T^{(t)}$ and those events are used multiple times in our di-hadron correlation analysis [17].

It is worthwhile to emphasize here that our quantitative results depend on the assumption of the ZYAM background normalization, and the effects of variations in the ZYAM normalization within reasonable range are assessed by systematic uncertainties. However, as will be discussed in Sec. III E, our qualitative conclusions are not affected by the ZYAM normalization.

III. SYSTEMATIC UNCERTAINTIES

Background subtraction is the major source of systematic uncertainty in our results. We first study the dihadron correlations with even harmonic flow subtraction. The even harmonic flow background, as given by Eq. (1), has three important ingredients: the anisotropic flow measurements v_2 and v_4, the event-plane resolutions, and the background magnitude B. We discuss these systematic uncertainties in Sections III A-III E, respectively. They have effects on dihadron correlation functions presented in Sec. IV A and away-side correlation widths and magnitudes presented in IV B.

We also report results on near-side jet-like and ridge correlations in Sec. IV C. Uncertainties in v_2 and the ZYAM background normalization contribute to the uncertainties in the ridge correlation results. They do not affect the jet-like correlation results in which they largely cancel because v_2 is approximately independent of pseudo-rapidity within our acceptance. Additional systematic uncertainties arise from the assumption of a uniform ridge in $\Delta\eta$, which affects both the ridge and jet-like results. These additional systematic uncertainties are discussed in Sec. III F.

We also study the dihadron correlations with background subtraction including odd harmonic flow. Various systematics are discussed together with the correlation results in Sec. IV F.

A. Systematic Uncertainty due to Anisotropic Flow

The anisotropic flow (mainly elliptic flow) background which is to be subtracted from the dihadron correlation is the anisotropy caused by particle correlations to the participant plane [86, 87]. There are several measurements of elliptic flow; many of them are affected to various degrees by nonflow contributions that are caused by particle correlations unrelated to the reaction plane (or participant plane), such as resonance decays and jet-correlations. One technique, called the event-plane method, is to construct the event plane from all charged particles except those of interest and then calculate $v_2\{\mathrm{EP}\} = \langle\cos 2(\phi - \psi_{\mathrm{EP}})\rangle / \langle\cos 2\Delta\psi\rangle$ for the particles of interest, where $\langle\cos 2\Delta\psi\rangle$ is the event-plane resolution [32]. This method is affected by nonflow contributions in both sets of particles, those of interest and those used to construct the event plane. The $v_2\{\mathrm{EP}\}$ already contains flow fluctuation effects which should be included in the jet-correlation background.

Another method, called the two-particle method, is to calculate $v_2\{2\} = \sqrt{\langle\cos 2\Delta\phi\rangle}$ using all particle pairs of interest [32]. This method is affected by nonflow only in the interested particles used for correlation studies. This flow parameter also contains flow fluctuation effects. The two-particle cumulant method can be also applied between the particle of interest and a reference particle. The anisotropy of the particle of interest is then

TABLE III: Background level B in flow subtraction by Eq. (1) as a function of $p_T^{(a)}$ (in rows) and $\phi_s = |\phi_t - \psi_{\rm EP}|$ (in columns) in minimum-bias 20-60% Au+Au collisions. Both trigger particle p_T ranges of $3 < p_T^{(t)} < 4$ GeV/c and $4 < p_T^{(t)} < 6$ GeV/c are listed. The trigger and associated particles are within $|\eta| < 1$. Backgrounds are tabulated for the entire $|\Delta\eta| < 2$ range of our acceptance as well as for large $\Delta\eta$ cut of $|\Delta\eta| > 0.7$. The first error is statistical. The second error is the quadratic sum of the ZYAM systematic uncertainty and the one-sided systematic uncertainty due to background deviation from ZYAM. The former is assessed by varying the $\Delta\phi$ normalization range. The latter is assessed by comparing our ZYAM background to those obtained from asymmetric correlations of the separate positive and negative $\phi_t - \psi_{\rm EP}$ regions.

$p_T^{(a)}$ (GeV/c)	$0 - \pi/12$	$\pi/12 - \pi/6$	$\pi/6 - \pi/4$	$\pi/4 - \pi/3$	$\pi/3 - 5\pi/12$	$5\pi/12 - \pi/2$
			$3 < p_T^{(t)} < 4$ GeV/c			
0.15 - 0.5	$47.41 \pm 0.01^{+0.06}_{-0.07}$	$47.37 \pm 0.01^{+0.07}_{-0.09}$	$47.28 \pm 0.02^{+0.02}_{-0.17}$	$47.22 \pm 0.02^{+0.06}_{-0.08}$	$47.16 \pm 0.02^{+0.02}_{-0.10}$	$47.04 \pm 0.02^{+0.04}_{-0.06}$
0.5 - 1	$22.47 \pm 0.01^{+0.01}_{-0.10}$	$22.67 \pm 0.01^{+0.03}_{-0.15}$	$22.92 \pm 0.01^{+0.03}_{-0.20}$	$23.31 \pm 0.01^{+0.06}_{-0.18}$	$23.40 \pm 0.01^{+0.06}_{-0.11}$	$23.59 \pm 0.01^{+0.03}_{-0.09}$
1 - 1.5	$6.023 \pm 0.005^{+0.008}_{-0.015}$	$6.072 \pm 0.005^{+0.020}_{-0.089}$	$6.128 \pm 0.005^{+0.016}_{-0.106}$	$6.177 \pm 0.005^{+0.033}_{-0.081}$	$6.128 \pm 0.005^{+0.022}_{-0.042}$	$6.199 \pm 0.006^{+0.014}_{-0.028}$
1.5 - 2	$1.683 \pm 0.002^{+0.005}_{-0.007}$	$1.691 \pm 0.003^{+0.002}_{-0.034}$	$1.698 \pm 0.002^{+0.003}_{-0.046}$	$1.700 \pm 0.003^{+0.010}_{-0.034}$	$1.694 \pm 0.003^{+0.006}_{-0.036}$	$1.694 \pm 0.003^{+0.001}_{-0.013}$
2 - 3	$0.655 \pm 0.002^{+0.004}_{-0.002}$	$0.662 \pm 0.002^{+0.003}_{-0.017}$	$0.663 \pm 0.002^{+0.003}_{-0.028}$	$0.660 \pm 0.002^{+0.002}_{-0.026}$	$0.654 \pm 0.002^{+0.001}_{-0.014}$	$0.659 \pm 0.002^{+0.008}_{-0.011}$
			$4 < p_T^{(t)} < 6$ GeV/c			
0.15 - 0.5	$46.63 \pm 0.04^{+0.02}_{-0.12}$	$46.56 \pm 0.04^{+0.08}_{-0.16}$	$46.72 \pm 0.04^{+0.08}_{-0.24}$	$46.77 \pm 0.04^{+0.08}_{-0.27}$	$46.67 \pm 0.05^{+0.12}_{-0.07}$	$46.76 \pm 0.05^{+0.12}_{-0.15}$
0.5 - 1	$22.16 \pm 0.02^{+0.01}_{-0.07}$	$22.30 \pm 0.02^{+0.09}_{-0.22}$	$22.42 \pm 0.02^{+0.00}_{-0.32}$	$23.11 \pm 0.03^{+0.06}_{-0.19}$	$23.07 \pm 0.03^{+0.11}_{-0.09}$	$23.42 \pm 0.03^{+0.07}_{-0.17}$
1 - 1.5	$5.947 \pm 0.012^{+0.003}_{-0.049}$	$5.989 \pm 0.012^{+0.001}_{-0.084}$	$5.985 \pm 0.012^{+0.006}_{-0.109}$	$6.113 \pm 0.013^{+0.040}_{-0.101}$	$6.076 \pm 0.014^{+0.021}_{-0.061}$	$6.174 \pm 0.014^{+0.037}_{-0.057}$
1.5 - 2	$1.659 \pm 0.006^{+0.003}_{-0.041}$	$1.664 \pm 0.006^{+0.003}_{-0.035}$	$1.673 \pm 0.006^{+0.017}_{-0.050}$	$1.671 \pm 0.007^{+0.024}_{-0.051}$	$1.674 \pm 0.007^{+0.013}_{-0.022}$	$1.712 \pm 0.007^{+0.014}_{-0.038}$
2 - 3	$0.611 \pm 0.004^{+0.001}_{-0.006}$	$0.618 \pm 0.004^{+0.003}_{-0.017}$	$0.613 \pm 0.004^{+0.001}_{-0.024}$	$0.621 \pm 0.004^{+0.010}_{-0.028}$	$0.615 \pm 0.004^{+0.008}_{-0.012}$	$0.615 \pm 0.005^{+0.004}_{-0.014}$
3 - 4	$0.058 \pm 0.001^{+0.001}_{-0.002}$	$0.060 \pm 0.001^{+0.001}_{-0.009}$	$0.061 \pm 0.001^{+0.002}_{-0.014}$	$0.063 \pm 0.001^{+0.000}_{-0.016}$	$0.061 \pm 0.001^{+0.001}_{-0.020}$	$0.062 \pm 0.001^{+0.001}_{-0.004}$
			$3 < p_T^{(t)} < 4$ GeV/c, $\lvert\Delta\eta\rvert > 0.7$			
0.15 - 0.5	$19.37 \pm 0.01^{+0.02}_{-0.05}$	$19.35 \pm 0.01^{+0.02}_{-0.06}$	$19.29 \pm 0.01^{+0.00}_{-0.12}$	$19.25 \pm 0.01^{+0.00}_{-0.06}$	$19.28 \pm 0.01^{+0.02}_{-0.05}$	$19.22 \pm 0.01^{+0.00}_{-0.03}$
0.5 - 1	$9.187 \pm 0.006^{+0.001}_{-0.043}$	$9.268 \pm 0.006^{+0.022}_{-0.100}$	$9.356 \pm 0.006^{+0.022}_{-0.100}$	$9.507 \pm 0.007^{+0.022}_{-0.102}$	$9.548 \pm 0.007^{+0.009}_{-0.024}$	$9.603 \pm 0.007^{+0.041}_{-0.028}$
1 - 1.5	$2.452 \pm 0.003^{+0.004}_{-0.006}$	$2.475 \pm 0.003^{+0.006}_{-0.050}$	$2.497 \pm 0.003^{+0.012}_{-0.061}$	$2.512 \pm 0.003^{+0.014}_{-0.053}$	$2.493 \pm 0.003^{+0.012}_{-0.025}$	$2.517 \pm 0.004^{+0.017}_{-0.015}$
1.5 - 2	$0.683 \pm 0.002^{+0.003}_{-0.005}$	$0.688 \pm 0.002^{+0.003}_{-0.020}$	$0.691 \pm 0.002^{+0.003}_{-0.026}$	$0.689 \pm 0.002^{+0.005}_{-0.017}$	$0.686 \pm 0.002^{+0.007}_{-0.016}$	$0.685 \pm 0.002^{+0.005}_{-0.004}$
2 - 3	$0.264 \pm 0.001^{+0.001}_{-0.004}$	$0.269 \pm 0.001^{+0.002}_{-0.008}$	$0.269 \pm 0.001^{+0.002}_{-0.014}$	$0.267 \pm 0.001^{+0.002}_{-0.015}$	$0.265 \pm 0.001^{+0.003}_{-0.010}$	$0.264 \pm 0.001^{+0.004}_{-0.002}$
			$4 < p_T^{(t)} < 6$ GeV/c, $\lvert\Delta\eta\rvert > 0.7$			
0.15 - 0.5	$18.98 \pm 0.02^{+0.00}_{-0.05}$	$18.99 \pm 0.02^{+0.01}_{-0.10}$	$19.01 \pm 0.03^{+0.00}_{-0.11}$	$18.98 \pm 0.03^{+0.02}_{-0.16}$	$18.98 \pm 0.03^{+0.01}_{-0.01}$	$19.00 \pm 0.03^{+0.02}_{-0.07}$
0.5 - 1	$9.014 \pm 0.015^{+0.003}_{-0.045}$	$9.065 \pm 0.015^{+0.014}_{-0.116}$	$9.110 \pm 0.015^{+0.017}_{-0.122}$	$9.374 \pm 0.017^{+0.035}_{-0.108}$	$9.391 \pm 0.018^{+0.025}_{-0.077}$	$9.518 \pm 0.018^{+0.004}_{-0.120}$
1 - 1.5	$2.421 \pm 0.008^{+0.008}_{-0.012}$	$2.434 \pm 0.008^{+0.003}_{-0.036}$	$2.435 \pm 0.008^{+0.009}_{-0.078}$	$2.456 \pm 0.008^{+0.023}_{-0.045}$	$2.457 \pm 0.009^{+0.011}_{-0.034}$	$2.501 \pm 0.009^{+0.008}_{-0.019}$
1.5 - 2	$0.673 \pm 0.004^{+0.001}_{-0.011}$	$0.669 \pm 0.004^{+0.003}_{-0.017}$	$0.677 \pm 0.004^{+0.009}_{-0.032}$	$0.681 \pm 0.004^{+0.010}_{-0.039}$	$0.677 \pm 0.005^{+0.007}_{-0.010}$	$0.691 \pm 0.005^{+0.004}_{-0.018}$
2 - 3	$0.241 \pm 0.003^{+0.002}_{-0.004}$	$0.250 \pm 0.003^{+0.004}_{-0.010}$	$0.248 \pm 0.003^{+0.001}_{-0.014}$	$0.253 \pm 0.003^{+0.002}_{-0.014}$	$0.245 \pm 0.003^{+0.004}_{-0.007}$	$0.247 \pm 0.003^{+0.003}_{-0.004}$
3 - 4	$0.023 \pm 0.001^{+0.001}_{-0.001}$	$0.024 \pm 0.001^{+0.000}_{-0.003}$	$0.025 \pm 0.001^{+0.000}_{-0.004}$	$0.025 \pm 0.001^{+0.001}_{-0.008}$	$0.023 \pm 0.001^{+0.001}_{-0.007}$	$0.024 \pm 0.001^{+0.000}_{-0.002}$

the ratio of the two-particle cumulant to the anisotropy of the reference particles, which can be in turn obtained from the two-particle cumulant between reference particle pairs. (More details are given in Sec. IV F.) This method of mixed pair cumulant is intrinsically similar to the event-plane method.

The third method, called the four-particle method, is to obtain $v_2\{4\}$ from the four-particle cumulant [88]. This method is less affected by nonflow from particle clustering because the nonflow arising from two particle correlations is eliminated, and the nonflow from three particle correlations does not contribute. This method is subject to nonflow from higher orders (four-particle correlation and above) but those contributions are suppressed by high orders of multiplicity [88]. The flow fluctuation will give a negative contribution to $v_2\{4\}$ [88].

The fourth method is to decompose the low p_T two-particle correlation (the so-called untriggered correlation, without the requirement of a trigger particle) into a near-angle Gaussian, a dipole, and a quadrupole, and infer $v_2\{2\text{D}\}$ from the fitted quadrupole [89]. The method attempts to geometrically separate the reaction-plane correlated v_2 from other (i.e. nonflow) correlations (small-angle correlations and large-angle dipole). However, the method assumes a particular functional form for those nonflow correlations, whereas the goal of this paper is to study the magnitude and shape of those nonflow (jet) correlations, defined to be the data minus harmonic (flow) backgrounds.

The measured $v_2\{2\}$ and $v_2\{\text{MRP}\}$ are similar and they both significantly overestimate elliptic flow due to large contributions from nonflow and fluctuations. While flow fluctuation effect should be included in our background subtraction, nonflow should be excluded. The major

component of nonflow is the measured small-angle two-particle correlation [47, 48, 90]. To suppress nonflow, a pseudo-rapidity η-gap ($\eta_{\rm gap}$) is often applied between the particle pair in the $v_n\{2\}$ measurement, and in the $v_2\{\rm EP\}$ measurement, between the particle of interest and the particles used in EP reconstruction. In this analysis, we apply $\eta_{\rm gap} = 0.7$ to obtain the two-particle cumulant elliptic flow, $v_2\{2, \eta_{\rm gap}{=}0.7\}$. However, the away-side two-particle correlations, presumably due to jet-like correlations, cannot be eliminated [8, 91, 92]. This is because inter-jet correlation in η is broad (nearly uniform in the STAR TPC acceptance) due to the unconstrained underlying parton kinematics in the longitudinal direction.

We use $v_2\{2\}$ as our upper systematic bound for v_2. The $v_2\{2\}$ is measured in 10%-size centrality bins. Two-particle cumulants between the particle of interest and a reference particle, $V_n\{p_T\text{-ref}\}$, and between two reference particles, $V_n\{\text{ref-ref}\}$, are calculated. The particle of interest is from a particular p_T bin while the reference particle is from $0.15 < p_T < 2$ GeV/c. To reduce nonflow one particle is taken from $\eta < -0.35$ and the other from $\eta > 0.35$, with an $\eta_{\rm gap} = 0.7$ in-between. The v_n are referred to as $v_n\{2, \eta_{\rm gap}{=}0.7\}$ or simply as $v_n\{2\}$. The cumulants are calculated by the Q-cumulant method and divided by the corresponding number of pairs in each event. The cumulants are averaged over the event sample with a unit weight (not weighted by the number of pairs). The anisotropy of the particle of interest is simply given by

$$v_n\{2\}(p_T) = \frac{V_n\{p_T\text{-ref}, \eta_{\rm gap}{=}0.7\}}{\sqrt{V_n\{\text{ref-ref}, \eta_{\rm gap}{=}0.7\}}}\,. \qquad (12)$$

The $v_n\{2\}$ of the four individual centralities are averaged by weighting each centrality by the number of particles of interest.

The measured $v_2\{4\}$ likely underestimates elliptic flow because the flow fluctuation effect in $v_2\{4\}$ is negative [88]. We note that $v_2\{4\}$ may still contain some nonflow effects. However, the agreement between $v_2\{4\}$ and the elliptic flow measurement using the Lee-Yang-Zero method suggests that such nonflow effects are small [93]. We therefore use $v_2\{4\}$ as our lower bound of v_2 systematic uncertainty, as same as in Refs. [13, 17]. The $v_2\{4\}$ is obtained as follows. Two four-particle cumulants are calculated. One is for quadralets of one particle of interest and three reference particles, referred to as $V_2\{p_T\text{-ref}^3\}$. The other is for quadralets of four reference particles, referred to as $V_2\{\text{ref}^4\}$. Since nonflow is negligible in $v_n\{4\}$, no $\eta_{\rm gap}$ is applied; all four particles are from the entire region of $|\eta| < 1$. Similar to $v_2\{2\}$, the Q-cumulant method is used to calculate $v_2\{4\}$. Self-correlations are properly removed. The four-particle anisotropy of the particle of interest is given by

$$v_2\{4\}(p_T) = V_2\{p_T\text{-ref}^3\}/(V_2\{\text{ref}^4\})^{3/4}\,. \qquad (13)$$

Again the $v_2\{4\}(p_T)$ of the four individual centralities are averaged by weighting each centrality by the number of particles of interest.

As the default v_2, we use the average

$$v_2 = (v_2\{2\} + v_2\{4\})/2\,. \qquad (14)$$

We use the range bracketed by $v_2\{2\}$ and $v_2\{4\}$ as our systematic uncertainty on v_2. Table I lists the default v_2 values together with systematic uncertainties for different p_T bins in 20-60% Au+Au collisions.

We parameterized the v_4 measurement [45] as

$$v_4\{\psi_2\} = 1.15 v_2^2\,, \qquad (15)$$

and used this parameterization for both trigger and associated particles in our flow correction [31]. The uncertainties in v_2 are propagated to v_4. Note that the v_4 fluctuation effects related to the second harmonic event plane, which should be included in our flow background, are already included in the v_4 measurement which was carried out with respect to the second harmonic event plane [45, 83]. Fluctuations in v_4 related to the fourth harmonic event plane could be potentially not small [83] and are not included in the available measurement of v_4, however, these fluctuation effects come into our two-particle correlation background as v_4^2 (not through the cross-term of $v_2 v_4$) and are therefore negligible for our centrality range. Nevertheless, in Sec. IV F, we also include this fluctuation effect in flow subtraction.

The flow backgrounds are shown by the solid curves in Fig. 3. The systematic uncertainties due to anisotropic flow parameters are shown by the dashed curves. The normalization of each background curve is adjusted by ZYAM to match the raw correlation function such that the background-subtracted correlation is zero at minimum (see Sec. II D). As seen from the figures, the dashed curves are not symmetric about the solid curve. This is mainly due to the ZYAM normalization as the normalization region is around $\Delta\phi \approx \pm 1$, not at $\pm\pi/2$.

The coefficient $v_2^{(a)} v_2^{(t,R)}$ in Eq. (1) determines the size of the modulation in the flow background. These coefficients are tabulated in Table II. For in-plane trigger particles, $v_2^{(t,R)}$ is positive as given by Eq. (2) or (4). The correlated elliptic flow uncertainties in $v_2^{(a)}$ and $v_2^{(t,R)}$ gives a large uncertainty in $v_2^{(a)} v_2^{(t,R)}$. For out-of-plane trigger particles, however, $v_2^{(t,R)}$ is negative. The correlated uncertainty in $v_2^{(a)}$ and $v_2^{(t,R)}$ tends to cancel each other, resulting in a small uncertainty in $v_2^{(a)} v_2^{(t,R)}$. This is apparent in the systematic uncertaities listed in Table II. It is shown in the systematic uncertainty background curves in Fig. 3, where the uncertainty for in-plane correlations is large, while for out-of-plane correlations it is small.

B. Systematic Uncertainty due to Event-Plane Resolution

The event-plane resolutions enter into the flow background modulation together with the anisotropic flow pa-

rameters, via $v_n\langle\cos(k\Delta\psi)\rangle$. Terms with $k = n$ are not affected by uncertainties in the event-plane resolutions, because $v_n\langle\cos(n\Delta\psi)\rangle$ are the measured anisotropic flow parameters. The event-plane resolutions $\langle\cos(k\Delta\psi)\rangle$ of different k's are likely correlated, hence the uncertainty in $v_n\langle\cos(k\Delta\psi)\rangle$ for $k \neq n$ due to uncertainties in the resolutions may be greatly reduced. To be conservative, we assume the uncertainties in the event-plane resolutions to be uncorrelated in our estimation of their effects on our correlation results.

The systematic uncertainty of the event-plane resolution was determined by repeating the sub-event method, but splitting the particles by charge instead of by random determination, as done in the default case. They are also assessed by comparing the event-plane resolution from triggered events only (default) to inclusive events, and by applying a weighting of the number of trigger particles (default) and not applying this weighting. In addition, differences in event-plane resolutions are assessed with (default) and without event-plane flattening by weighting of the inverse of ϕ-dependent efficiencies. The event-plane resolution uncertainties thus estimated are typically less than 1% for $\langle\cos(2\Delta\psi)\rangle$, and less than 2-3% for $\langle\cos(4\Delta\psi)\rangle$ and $\langle\cos(6\Delta\psi)\rangle$.

The effects of the estimated event-plane resolution uncertainties on the final background-subtracted correlation functions are significantly smaller than those caused by the uncertainties on anisotropic flow, and are therefore neglected.

C. Effect of Finite Centrality Bin Width

For the data reported in this paper, the entire 20-60% Au+Au centrality range is treated as a single centrality bin in which the event-plane resolutions and elliptic flow are obtained and the azimuthal correlation is analyzed. Alternatively, the analysis was repeated in each of the four 10%-size centrality bins using the corresponding event-plane resolutions and the elliptic flow measurements. Those correlation results are added together, weighted by the number of trigger particles in each centrality bin. The recombined results are consistent with using a single 20-60% centrality bin, well within the systematic uncertainties due to those in flow subtraction and ZYAM normalization. This is because the measured elliptic flow v_2 is fairly constant over the entire 20-60% centrality range, so that $\langle v_2^{(t)} v_2^{(a)}\rangle \approx \langle v_2^{(t)}\rangle\langle v_2^{(a)}\rangle$. The event-plane resolutions vary with centrality mainly due to the multiplicity change. However, the event-plane resolutions enter into the flow background of Eq. (1) linearly, and because the high p_T trigger particle multiplicity scales almost linearly with the total multiplicity, the effect of the centrality-varying event-plane resolution is minimal in the flow correction calculated from the single 20-60% centrality bin or summed from multiple narrower centrality bins.

D. Systematic Uncertainty due to ZYAM Background Normalization

Naively one would expect the background level B in Eq. (1) to be the same for all ϕ_s slices because the underlying background should not depend on the signal (or orientation of the trigger particle). However, there could be biases in the event samples with trigger particles at different ϕ_s such that they contain slightly different underlying background multiplicities due to the possible difference in jet-like correlated multiplicities at different ϕ_s and the overall constraints caused by centrality cuts on the reference multiplicity. In our analysis we use different B values for different ϕ_s slices, each independently obtained using ZYAM on the correlation function of the corresponding slice.

One source of systematic uncertainty on B is due to the limited range in $\Delta\phi$ where the background-subtracted correlations appear to have a minimum 'plateau'. This part of the systematic uncertainty is assessed by varying the size of the normalization range in $\Delta\phi$ between $\pi/12$ and $\pi/4$ (default range is $\pi/6$), similarly to Ref. [13].

The ZYAM assumption likely gives an upper limit to the underlying background level. One could make an improved assessment of the background level with more stringent requirements, such as using three-particle correlation ZYAM [31]. However, the analysis of three-particle correlation within a limited ϕ_s range of the trigger particle is difficult.

In this paper, we assess this part of the systematic uncertainty on B by comparing to the ZYAM backgrounds obtained separately from correlation functions at positive $\phi_t - \psi_{\rm EP}$ and negative $\phi_t - \psi_{\rm EP}$. Those ZYAM backgrounds are always lower than our default B from ZYAM of the combined correlation function of positive and negative $\phi_t - \psi_{\rm EP}$. This is because the separately analyzed correlation functions are asymmetric about $\Delta\phi = 0$ and $\Delta\phi = \pi$, and the ZYAM is determined by only one side of the correlation function [94, 95], whereas in our combined correlation functions reported here, the two sides of the separately analyzed asymmetric correlation functions are averaged. We treat the difference between the ZYAM background from this paper and that obtained from the asymmetric correlation functions as an additional, one-sided systematic uncertainty on B.

We may also study the background level by fitting the ZYAM-background-subtracted correlation functions with a combination of Gaussians and a free parameter for an offset from zero. Specifically we fit the correlation data to three Gaussians (a near-side Gaussian at $\Delta\phi = 0$ and two away-side Gaussians symmetric about $\Delta\phi = \pi$), and four Gaussians (adding a fourth Gaussian at $\Delta\phi = \pi$ with the same width as the near-side Gaussian). Some of the fits yielded unphysical offsets because of the limited constraint of the correlation data on the fit model. For the other fits, the fitted offsets are comparable to the systematic uncertainty obtained from the comparisons to the asymmetric correlation functions discussed above.

The Gaussian fits to the correlation functions without the offset will be discussed in Sec. IV E.

The different sources of systematic uncertainties on B are added in quadrature. The total systematic uncertainty is listed in Table III together with the statistical uncertainty. We take the quadratic sum of the statistical and systematic uncertainties as the total uncertainty for B on our correlation results.

E. Is the Away-Side Double-Peak an Artifact of ZYAM?

As will be shown in IV A, the v_2 and v_4 background-subtracted correlation functions on the away side are single-peaked at $\Delta\phi = \pi$ for triggered particles in-plane, but double-peaked for trigger particles out-of-plane beyond the flow systematic uncertainties. Since the subtracted background is flow-modulated, the natural question is whether the away-side double-peak structure is due to an unrealistic systematic uncertainty. To address this question, it is worthwhile to note that the flow background modulation changes phase when the trigger particle moves from in-plane to out-of-plane, as shown in Fig. 3. A smaller elliptic flow would make the in-plane correlation more peaked at $\Delta\phi = 0$ and π and the out-of-plane correlation more dipped at π (hence more double peaked on the away side). On the other hand, a larger elliptic flow would make the out-of-plane away-side correlation less double-peaked. One would need a $\sim$15% larger $v_2^{(a)}v_2^{(t,R)}$ than in Table II, significantly beyond the systematic uncertainty from the anisotropy measurements, to eliminate the away-side double-peak for the out-of-plane ϕ_s slice. However, this large $v_2^{(a)}v_2^{(t,R)}$ would result in double-peaked away-side correlations for some of the other ϕ_s slices.

The background magnitude affects the absolute magnitude of the flow modulation subtracted from the raw data in obtaining the correlation signal. Since the background normalization is determined by the ZYAM description, the question arises whether the away-side double-peak for the out-of-plane ϕ_s slices is an artifact of a significantly smaller background level than ZYAM beyond the ZYAM normalization systematic uncertainty. The answer is negative because the flow background is the lowest at $\Delta\phi = \pi$ for out-of-plane trigger particles. Allowing a non-zero flow-modulated "pedestal" into the correlation signal will exaggerate the double-peak feature, i.e., the dip at $\Delta\phi = \pi$ will be even deeper than the double peaks. In other words, if the true background is lower than ZYAM, then the away-side correlation functions for out-of-plane trigger particles will be more double-peaked. Only when the background is larger than ZYAM would the dihadron correlation signal become single-peaked; however, as a result the signal strength would become negative.

In summary, to eliminate the away-side double-peak, one needs either a larger anisotropic flow than measured while fixing the background normalization by ZYAM, or a larger background normalization than ZYAM while fixing the anisotropic flow as measured. To investigate further the interplay between background normalization and anisotropic flow and its effect on the dihadron correlation signal, we performed a study of free fits to the raw correlation data, treating the anisotropic flow and the background magnitude as free parameters. In order to do so, one needs a prescription for the correlation signal functional form. It has been shown that the sum of a near-side Gaussian, a negative dipole, and a quadrupole (reflecting elliptic flow) can adequately describe the two-particle azimuthal correlation at low p_T without the requirement of a high p_T trigger particle [47, 48]. Thus, we fit our raw correlation data by

$$\frac{dN}{d\Delta\phi} = B\left(1 + 2V_2\cos 2\Delta\phi + 2V_4\cos 4\Delta\phi\right) + A_{\rm ns}\exp\left(-\frac{(\Delta\phi)^2}{2\sigma_{\rm ns}^2}\right) - A_{\rm dipole}\cos\Delta\phi, \quad (16)$$

treating the flow modulations V_2 and V_4, the near-side Gaussian parameters $A_{\rm ns}$ and $\sigma_{\rm ns}$, and the negative dipole magnitude $A_{\rm dipole}$ as free parameters. Figure 4 (upper panels) shows the fits by Eq. (16) to the raw correlation functions in six ϕ_s slices for $3 < p_T^{(t)} < 4$ GeV/c and $1 < p_T^{(a)} < 2$ GeV/c. The fits are shown in the solid curves. The dashed curves show the fitted flow backgrounds. The lower panels of Fig. 4 show the correlation functions after subtracting the fitted flow backgrounds. The fitted near-side Gaussian and the negative dipole are depicted individually.

As seen from the χ^2/NDF written in each upper panel, the fits by Eq. (16) are generally good. This is also true for the other $p_T^{(t)}$ and $p_T^{(a)}$ bins. However, the fitted flow modulations (written in the lower panels) are significantly larger than the measured ones for the out-of-plane ϕ_s slices, much beyond their systematic uncertainties quoted in Table II. In other words, in order to eliminate the away-side double-peak, an anisotropic flow that is much larger than that measured by two-particle cumulant method is required, consistent with our earlier observation. Moreover, the deviations of the fitted flow modulations from the measured ones vary from slice to slice (non-monotonically), which should not be the case if the measured flow parameters that we used were simply in error. Qualitatively the same features are observed for the other $p_T^{(t)}$ and $p_T^{(a)}$ bins. These free fit results suggest that the near-side Gaussian and the negative dipole in the fit model of Eq. (16) likely do not correspond to the nonflow dihadron correlation signal sought after in this analysis with a high p_T trigger particle.

We have also used other single-peaked functional forms, e.g., a near-side Gaussian and an away-side Gaussian, in our fit. Similar conclusions were reached. The away-side double-peak for the out-of-plane trigger particles cannot be eliminated without using a flow subtraction much larger than experimentally determined, either

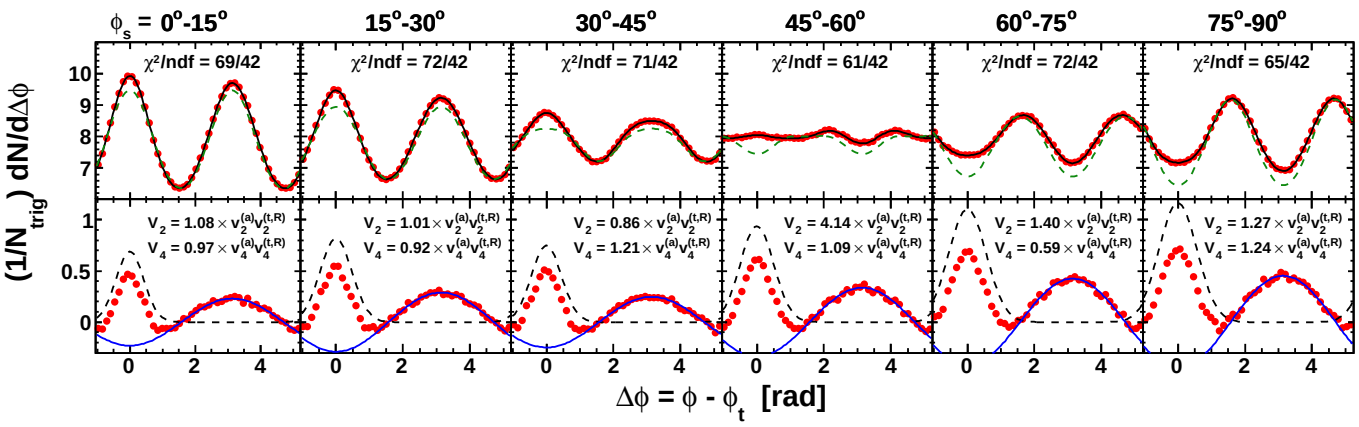

FIG. 4: (Color online) Fit by Eq. (16) to the raw correlation data in the upper panels of Fig. 3. (Upper panels) The solid curves are the fit results and the dashed curves are the fitted flow background. (Lower panels) The correlation functions after subtracting the fitted flow background. The texts in each plot are the fitted V_2 and V_4 results relative to the measured $v_2^{(a)}v_2^{(t,R)}$ and $v_4^{(a)}\{\psi_2\}v_4^{(t,R)}\{\psi_2\}$, respectively. The fitted same-side Gaussian and negative dipole are depicted individually in the dashed and solid curves, respectively.

with or without ZYAM. Thus, we conclude that the away-side double-peak structure is not an artifact of the ZYAM flow subtraction procedure used in this analysis.

F. Systematic Uncertainties on Jet-Like and Ridge Correlations

To obtain the jet-like component we take the difference of the correlation functions from $|\Delta\eta| < 0.7$ and $|\Delta\eta| > 0.7$ (properly weighted by the relative two-particle $\Delta\eta$ acceptance). The assumption in this procedure is that the ridge is uniform in $\Delta\eta$ (after taking into account the trivial two-particle $\Delta\eta$ acceptance) and is therefore subtracted away in the difference [14]. Measurements at low p_T without a trigger particle indicate that the ridge is broad but drops with increasing $\Delta\eta$ [96]. If this is true for trigger particle correlations as studied here, our "jet" measurement contains a residual ridge contribution. To estimate this effect, we study $\Delta\eta$ correlation functions for near-side associated particles ($|\Delta\phi| < 1$). An example is shown in Fig. 5 for $3 < p_T^{(t)} < 4$ GeV/c and $0.15 < p_T^{(a)} < 3$ GeV/c in the 20-60% centrality bin. The in-plane direction ($0 < \phi < \pi/4$) is used because, as will be shown later, the ridge resides mainly in the in-plane direction. We compare the ridge contributions to the $|\Delta\eta| < 0.7$ region as extrapolated from a constant ridge fit and from a linear fit [14], both done in the large $\Delta\eta$ range of $|\Delta\eta| > 0.7$. Because of possible edge effects in the $\Delta\eta$ acceptance, we also limit our fit range within $0.7 < |\Delta\eta| < 1.6$. We assign the difference, ±15%, as the systematic uncertainty on the jet-like component yield due to the assumption of the uniform ridge.

In this paper, we consider all correlated particles at $|\Delta\eta| > 0.7$ and $|\Delta\phi| < 1$ to be part of the ridge. The ridge yield we report in this paper is defined to be the integral of the correlated particle yield over $0.7 < |\Delta\eta| < 2.0$ (and $|\Delta\phi| < 1$). Thus, the assumption of the ridge shape does not affect the ridge yield.

We have assumed that the jet-like component is contained within $|\Delta\eta| < 0.7$, and assigned the entire correlated yield in $|\Delta\eta| > 0.7$ as ridge. This introduces uncertainty in the ridge yield as well as in the jet-like yield. Moreover, the fraction of the jet-like component that leaks out of the $\Delta\eta$ cut is subtracted in obtaining the jet-like part, thus the effect of the leakage is doubled in the extracted jet-like component. To study this effect, we fit the $\Delta\eta$ correlation function (such as that shown in the upper panel of Fig. 5) to a Gaussian with centroid at $\Delta\eta = 0$ and a constant pedestal (i.e., uniform ridge). The Gaussian width is shown in Fig. 5(b) as a function of ϕ_s for $1 < p_T^{(a)} < 2$ GeV/c and in Fig. 5(c) as a function of $p_T^{(a)}$ for integrated ϕ_s. The Gaussian width does not significantly depend on ϕ_s or $p_T^{(a)}$. We estimate the effect of the leakage of the jet-like component to be about 10% of the jet-like yield, assigned as a single-sided negative uncertainty on the ridge yield, and a single-sided positive uncertainty, twice as large, on the jet-like yield. The physics of the correlation widths will be discussed in Sec. IV E.

The systematic uncertainty on the jet-like yield due to flow uncertainty is small because the large uncertainties due to v_2 are cancelled, assuming v_2 is constant over $\Delta\eta$. This should be a good assumption because the PHOBOS experiment found that v_2 was constant within the η acceptance of the STAR TPC (dropping only towards larger $|\eta|$) [97, 98].

Figure 6 illustrates the various systematic uncertainties on the extracted ridge yield. (i) The systematic uncertainties due to flow subtraction are shown by the solid curves. The uncertainty is dominant at small ϕ_s; the flow uncertainty at large ϕ_s is small. (ii) The system-

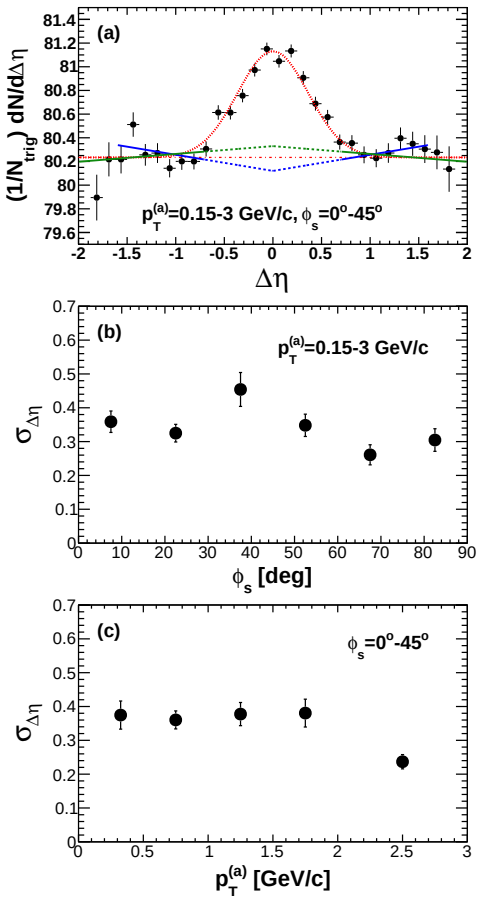

FIG. 5: (Color online) (a) Raw $\Delta\eta$ correlation of near-side associated hadrons ($|\Delta\phi| < 1$) integrated over $0 < \phi_s = |\phi_t - \psi_{\rm EP}| < \pi/4$ and $0.15 < p_T^{(a)} < 3$ GeV/c, corrected by the two-particle $\Delta\eta$ acceptance. The dotted curve is a single Gaussian fit and the dot-dashed horizontal line is the fit pedestal; the solid lines are linear fits to the regions $0.7 < |\Delta\eta| < 1.6$ and $0.7 < |\Delta\eta| < 2.0$, respectively, and the dashed lines are their extrapolations. (b) Gaussian fit σ to near-side $\Delta\eta$ correlation in $0.15 < p_T^{(a)} < 3$ GeV/c as a function of ϕ_s. (c) Gaussian fit σ to near-side $\Delta\eta$ correlation integrated over $0 < \phi_s < \pi/4$ as a function of $p_T^{(a)}$. The data are from minimum-bias 20-60% Au+Au collisions. The trigger particle p_T range is $3 < p_T^{(t)} < 4$ GeV/c. Error bars are statistical.

atic uncertainty due to background normalization uncertainty is shown in brackets, as assessed by varying background normalization range and by comparing to background normalizations of asymmetric correlation functions at positive and negative $\phi_t - \psi_{\rm EP}$ separately. (iii) There is an additional systematic uncertainty in the extracted ridge yield because the jet-like correlation can be broader than 0.7 in $\Delta\eta$ and the jet-like yield beyond $|\Delta\eta| > 0.7$ is contained in the extracted ridge yield. This part of the systematic uncertainty is shown by the arrows. The total systematic uncertainties are obtained by the quadratic sum of the individual sources and shown by the boxes.

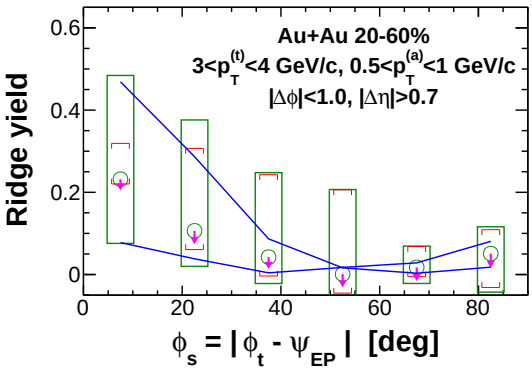

FIG. 6: (Color online) Illustration of the different systematic uncertainties on the ridge yield (defined in Sec. IV C) within $|\Delta\phi| < 1$ and $|\Delta\eta| > 0.7$ as a function of $\phi_s = |\phi_t - \psi_{\rm EP}|$. The data are from minimum-bias 20-60% Au+Au collisions. The trigger and associated particle p_T ranges are $3 < p_T^{(t)} < 4$ GeV/c and $0.5 < p_T^{(a)} < 1$ GeV/c, respectively. Statistical errors are smaller than the symbol size. The various systematic uncertainties are due to: (i) flow subtraction by Eq. (1) (shown by the solid curves), (ii) background normalization uncertainty (shown in brackets), assessed by varying ZYAM background normalization range and by comparing to ZYAM from asymmetric correlations separately for positive and negative $\phi_t - \psi_{\rm EP}$, and (iii) leakage from the jet-like component into the $|\Delta\eta| > 0.7$ region (shown by the arrows). The total systematic uncertainties are shown by the boxes.

IV. RESULTS AND DISCUSSIONS

We first present in Sections IV A–IV E our dihadron correlation results with subtraction of the v_2 and v_4 harmonic flow backgrounds of Eq. (1). We then present in Section IV F the corresponding dihadron correlation results with additional background subtraction including v_3 harmonic and other high-order effects by Eqs. (10 and (11).

A. Correlation Functions

Figure 7 shows the v_2 and v_4 background-subtracted dihadron azimuthal correlations in 20-60% Au+Au collisions as a function of the trigger particle orientation relative to the event plane, ϕ_s. The subtracted flow background is given by Eq. (1) using measurements in Table I and the parameterization of $v_4\{\psi_2\}$ by Eq. (15). The thin histograms embracing the shaded area indicate the systematic uncertainties due to anisotropic flow. The horizontal shaded band around zero indicates the systematic uncertainties due to ZYAM background normalization. The slight modulations of the edges of the band are because of the anisotropic flow in the combintorial background. For comparison the minimum-bias d+Au inclusive dihadron correlation (without differentiating with respect to an "event plane") is superimposed in each panel

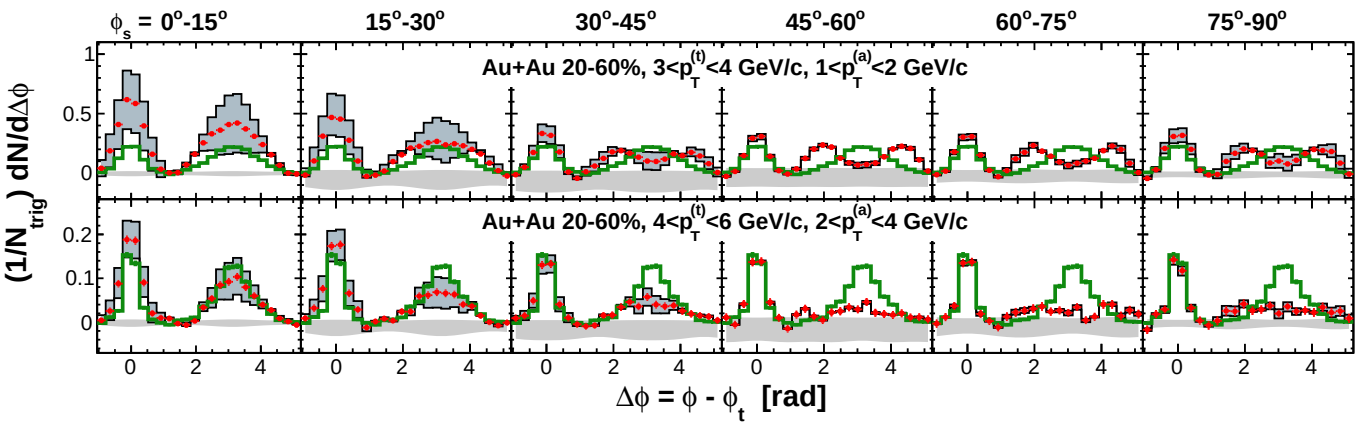

FIG. 7: (Color online) Background-subtracted dihadron correlations with trigger particle in six slices of azimuthal angle from the event plane, $\phi_s = |\phi_t - \psi_{\rm EP}|$. The trigger and associated particle p_T ranges are $3 < p_T^{(t)} < 4$ GeV/c and $1 < p_T^{(a)} < 2$ GeV/c (upper panel), and $4 < p_T^{(t)} < 6$ GeV/c and $2 < p_T^{(a)} < 4$ GeV/c (lower panel), respectively. Note the bottom row corresponds to the kinematic range used in Ref. [9]. Both the trigger and associated particles are restricted to be within $|\eta| < 1$. The triangle two-particle $\Delta\eta$ acceptance is not corrected. The data points are from minimum-bias 20-60% Au+Au collisions. Flow background is subtracted by Eq. (1) using measurements in Table I and the parameterization in Eq. (15). Systematic uncertainties are shown in the thin histograms embracing the shaded area due to flow subtraction and in the horizontal shaded band around zero due to ZYAM background normalization. Statistical errors are smaller than the symbol size. For comparison, the inclusive dihadron correlations from d+Au collisions are superimposed as the thick (green) histograms (only statistical errors are depicted).

in Fig. 7. The trigger and associated particle p_T ranges are $3 < p_T^{(t)} < 4$ GeV/c and $1 < p_T^{(a)} < 2$ GeV/c (upper panel), and $4 < p_T^{(t)} < 6$ GeV/c and $2 < p_T^{(a)} < 4$ GeV/c (lower panel), respectively. These kinematic ranges correspond to those for the raw correlations shown in Fig. 3. The background-subtracted correlations for all trigger and associated particle p_T ranges are presented in Appendix C in Figs. 31 and 32.

As seen in Fig. 7, the near-side peaks in Au+Au collisions are evident for all trigger particle orientations. The single-peak shape of the near-side correlation remains relatively unchanged from in-plane ($\phi_s \sim 0$) to out-of-plane ($\phi_s \sim \pi/2$). However, the amplitude of the near-side peak decreases with ϕ_s, becoming similar to that from d+Au collisions at large ϕ_s. Our previous studies have shown that the near-side correlation, while not much modified at high p_T, is enhanced in Au+Au collisions relative to p+p and d+Au collisions at low to modest p_T [13, 14, 17]. The present results show that the near-side enhancement is mostly present for trigger particles oriented in-plane and the modification for trigger particles oriented at $\phi_s \sim \pi/2$ is minimal for this centrality bin.

Unlike the near side, the away-side correlation structure evolves when trigger particles move from in-plane to out-of-plane for the 20-60% centrality bin. The away side has a single peak when the trigger particles are oriented close to the event plane. Only when the trigger particle direction is far away from the event plane, the double-peak structure emerges on the away side. In addition, the away-side modification increases with increasing associated particle $p_T^{(a)}$. Our previous studies showed that the away-side correlation structure is significantly modified in central Au+Au collisions, and the modification is the largest in the intermediate p_T range [13, 17]. The present result indicates that the away-side modification has a strong dependence on the trigger particle direction relative to the event plane. The strongest away-side modification is found for trigger particles perpendicular to the event plane (see Fig. 7). However, the systematic uncertainty due to flow subtraction is presently large; when the upper systematic bound of v_2 is used, the change from in-plane to out-of-plane is less dramatic. The results nevertheless suggest that the medium path-length dependence in ϕ_s plays an important role, and should provide useful input to theoretical modeling of partonic energy loss in the nuclear medium.

The lower panel of Fig. 7 shows the high p_T associated particle results. The "disappearance" of the away-side correlation at high associated particle p_T, first observed for this kinematic range in the inclusive dihadron correlations in Ref. [9], has a clear dependence on the trigger particle orientation. When the trigger particles move from $\phi_s \sim 0$ to $\pi/2$, the path-length increases, and the away-side peak(s) become diminished.

STAR has previously published dihadron correlations for in-plane ($\phi_s < \pi/4$) and out-of-plane ($\phi_s > \pi/4$) trigger particles [33]. We sum up our correlation results from slices 1-3 and 4-6 to obtain the in-plane and out-of-plane correlations, respectively. We have also analyzed the data treating $\phi_s < \pi/4$ as a single slice to obtain the in-plane correlation and $\phi_s > \pi/4$ for the out-of-plane correlation. The resultant correlation functions are consistent

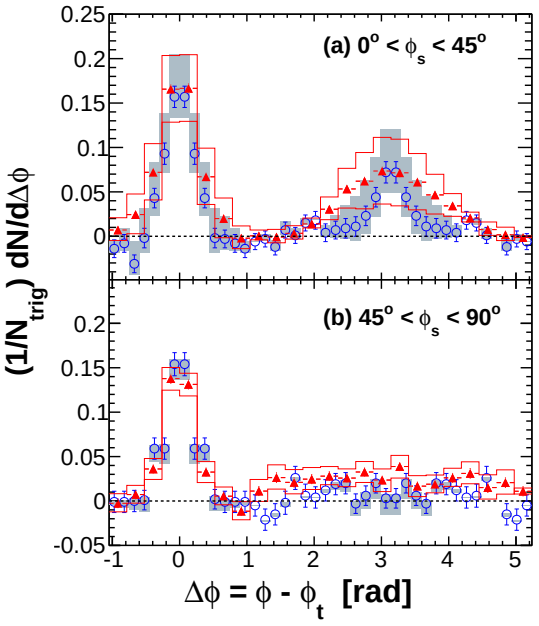

FIG. 8: (Color online) Comparison of dihadron correlation results from this work (triangles) to those in Ref. [33] (circles) for (a) in-plane ($\phi_s < \pi/4$) and (b) out-of-plane ($\phi_s > \pi/4$) trigger particles. Data are from 20-60% Au+Au collisions. The trigger and associated particle p_T ranges are $4 < p_T^{(t)} < 6$ GeV/c and $2 < p_T^{(a)} < 4$ GeV/c respectively. Both the trigger and associated particles are restricted within $|\eta| < 1$. The triangle two-particle $\Delta\eta$ acceptance is not corrected. Error bars are statistical. Systematic uncertainties in background subtraction by Eq. (1) (including those due to anisotropic flow v_2 and due to background normalization from different ZYAM normalization ranges) are shown in histograms for results from this work and in shaded areas for results from Ref. [33]. The systematic uncertainty due to background deviations from ZYAM is not included for fair comparison.

with those reported here that were summed from individual slices. Figure 8 compares results from this work to those in [33]. The histograms show systematic uncertainties of the results from this work, while the shaded boxes show those of the results from [33]. The analysis reported here differs from that in Ref. [33] in two ways: (i) In the average $v_2 = (v_2\{2, \eta_{\rm gap}{=}0.7\} + v_2\{4\})/2$ used in this analysis the two-particle cumulant flow was obtained with a $\eta_{\rm gap} = 0.7$, whereas in the average used in Ref. [33] all particle pairs are included in the two-particle cumulant flow which contains more significant nonflow effect; (ii) The flow correlation is corrected up to v_4 in this analysis while correction only up to v_2 was done in Ref. [33].

Figure 9 shows the in-plane and out-of-plane correlation results for two trigger $p_T^{(t)}$ ranges and two associated particle $p_T^{(a)}$ ranges for the 20-60% Au+Au collisions. The histograms show the systematic uncertainties due to flow subtraction; those due to ZYAM background normalization are shown as boxes in the legends.

With admittedly large systematic uncertainties, a difference seems evident between in-plane and out-of-plane dihadron correlations for both trigger $p_T^{(t)}$ ranges and both associated particle $p_T^{(a)}$ bins. The near-side correlated yield appears larger for in-plane than out-of-plane triggers. As will be discussed in Sections IV C and IV D, the difference is due to the larger ridge contribution in-plane than out-of-plane, and the jet-like contributions are similar between in-plane and out-of-plane. A more significant difference appears on the away side between in-plane and out-of-plane correlations. For in-plane trigger particles, the away-side correlations appear to peak at $\Delta\phi = \pi$. For out-of-plane trigger particles, the away-side correlations are double-peaked. The double-peak structure is stronger for the lower trigger particle $p_T^{(t)}$ range. The away-side structure is studied in more detail in Sec. IV B below.

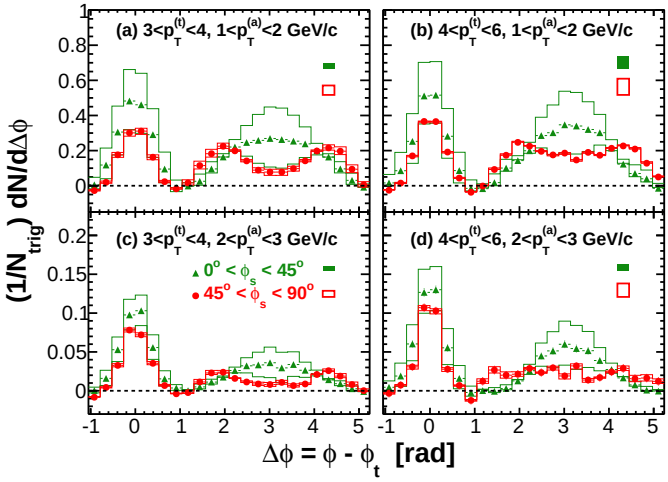

FIG. 9: (Color online) Background-subtracted dihadron correlations with trigger particles in-plane ($\phi_s < \pi/4$) and out-of-plane ($\phi_s > \pi/4$) in 20-60% Au+Au collisions. The results are for $3 < p_T^{(t)} < 4$ GeV/c (left panels) and $4 < p_T^{(t)} < 6$ GeV/c (right panels), and $1 < p_T^{(a)} < 2$ GeV/c (upper panels) and $2 < p_T^{(a)} < 3$ GeV/c (lower panels). Both the trigger and associated particles are restricted within $|\eta| < 1$. The triangle two-particle $\Delta\eta$ acceptance is not corrected. Flow background is subtracted by Eq. (1) using measurements in Table I and the parameterization in Eq. (15). Error bars are statistical. Systematic uncertainties due to those on anisotropic flow v_2 are shown in histograms; those due to ZYAM background normalization are indicated by the vertical sizes of the filled and hollow boxes in the legends for in-plane and out-of-plane trigger particles, respectively.

B. Discussion on the Away-Side Results

In order to quantify the modification in the away-side correlation structure, we calculate the width of the dis-

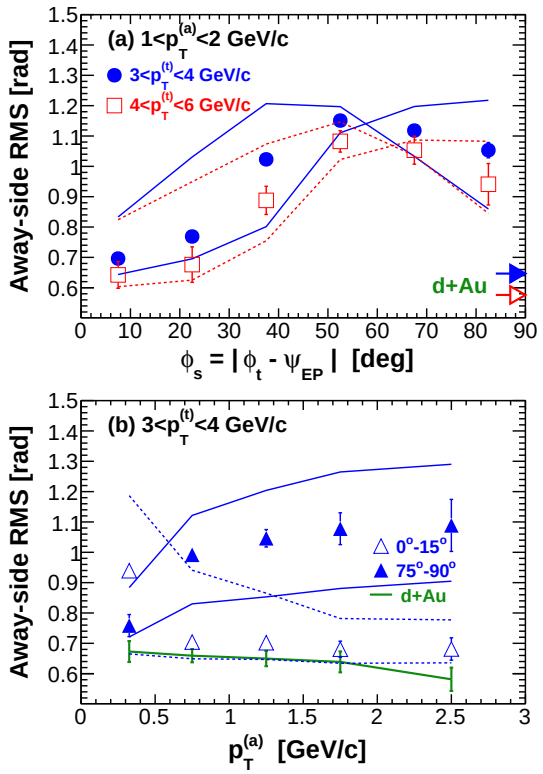

FIG. 10: (Color online) (a) The away-side RMS of the dihadron correlation function versus the trigger particle azimuth relative to the event plane, $\phi_s = |\phi_t - \psi_{\rm EP}|$, in 20-60% Au+Au collisions for $1 < p_T^{(a)} < 2$ GeV/c. Two trigger $p_T^{(t)}$ selections are shown: $3 < p_T^{(t)} < 4$ GeV/c (solid circles) and $4 < p_T^{(t)} < 6$ GeV/c (hollow squares). (b) The away-side RMS for slice 1 (hollow triangles) and slice 6 (solid triangles) versus the associated particle $p_T^{(a)}$ in 20-60% Au+Au collisions. The trigger particle p_T range is $3 < p_T^{(t)} < 4$ GeV/c. Error bars are statistical. The curves indicate systematic uncertainties due to flow subtraction, solid curves for the solid data points and dashed curves for the hollow data points. The systematic uncertainty due to ZYAM background normalization is not shown. The corresponding d+Au results are indicated by the arrows (solid arrow for $3 < p_T^{(t)} < 4$ GeV/c and hollow arrow for $4 < p_T^{(t)} < 6$ GeV/c) in the upper panel and by the lower solid line connecting error bars in the lower panel.

tribution by

$$\text{RMS} = \left(\frac{\int_1^{2\pi-1} \frac{dN}{d\Delta\phi}(\Delta\phi - \pi)^2 d\Delta\phi}{\int_1^{2\pi-1} \frac{dN}{d\Delta\phi} d\Delta\phi} \right)^{1/2} . \quad (17)$$

We show in Fig. 10(a) the RMS of the away-side correlation as a function of the trigger particle orientation ϕ_s for 20-60% Au+Au collisions. The associated particle p_T range is $1 < p_T^{(a)} < 2$ GeV/c. Two trigger particle p_T ranges are shown: $3 < p_T^{(t)} < 4$ GeV/c and $4 < p_T^{(t)} < 6$ GeV/c. The central value of RMS increases with increasing ϕ_s by approximately a factor of 1.5 from in-plane to out-of-plane. The distribution becomes more double-peaked as ϕ_s increases. No difference is observed between the two trigger $p_T^{(t)}$ selections. Only when the upper bound of ellipic flow is used for background subtraction, does the away-side RMS difference between $\phi_s = 0$ and π diminish, but the change of RMS with ϕ_s becomes nonmonotonic.

For comparison, the d+Au results are indicated by the arrows in Fig. 10(a). As seen, the RMS in 20-60% Au+Au collisions from slices 1 and 2 is not much larger than in d+Au. This may be consistent with the path-length effect. However, we note that the correlation amplitudes in Au+Au collisions for the in-plane slices are larger than in d+Au collisions, as discussed below. This suggests that the away-side single peak in Au+Au and d+Au collisions may come from different physics mechanisms. As will be discussed in Sec. IV C, the near-side correlation for in-plane trigger particles has a large contribution from the ridge, and it is likely that there is an accompanying back-to-back ridge on the away side.

Figure 10(b) shows the RMS as a function of the associated particle $p_T^{(a)}$ for slices 1 and 6 in 20-60% centrality. The RMS remains constant for slice 1, and is not much broader than the d+Au result for all measured $p_T^{(a)}$ bins. The RMS for slice 6 increases with $p_T^{(a)}$ and then seems to saturate. The double-peak structure is the strongest when the trigger particle is perpendicular to the reaction plane and the associated particle is not soft. Results for other slices vary smoothly between slices 1 and 6. The features for trigger particles of $4 < p_T^{(t)} < 6$ GeV/c are qualitatively the same.

The away-side double-peak structure observed in the inclusive dihadron correlation (i.e., without differentiating trigger particle azimuthal angles relative to the reaction plane) [13] has stimulated much interest [20–27, 29]. The three-particle jet-like correlation studies indicate that the double-peak correlated hadrons are emitted event-by-event, not an effect of averaging of single peaks in individual events [31]. To study the double-peak structure in more detail, we show in Fig. 11 the average correlation amplitude on the away side in the π-region ($|\Delta\phi - \pi| < 0.39$) and in the double-peak region ($0.81 < |\Delta\phi - \pi| < 1.59$) as a function of ϕ_s in 20-60% Au+Au collisions. Two trigger $p_T^{(t)}$ selections are shown; no significant difference is observed. With default elliptic flow subtraction, the amplitudes in the π-region drop with increasing ϕ_s, from a value larger than that in d+Au (as indicated by the arrows) to a value significantly smaller than that in d+Au. If the upper systematic bound of the elliptic flow is subtracted, the π-region amplitude seems to vary nonmonotonically with ϕ_s. On the other hand, the double-peak region amplitude seems rather constant with ϕ_s in Au+Au collisions, and is significantly stronger than that in d+Au collisions for both trigger particle $p_T^{(t)}$ selections. This suggests that the double-peak emission of correlated hadrons may also be

present underneath the single away-side peak for in-plane trigger particles. See discussion in Sec. IV D.

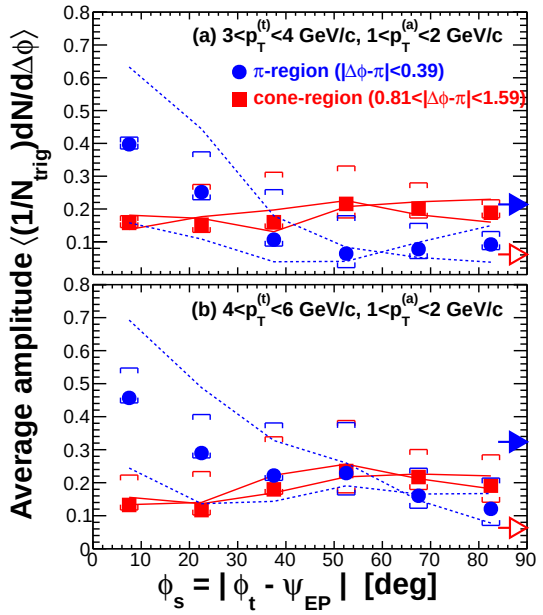

FIG. 11: (Color online) The away-side dihadron correlation amplitudes in the π-region ($|\Delta\phi - \pi| < 0.39$) and the double-peak region ($0.81 < |\Delta\phi - \pi| < 1.59$) as a function of the trigger particle azimuth relative to the event plane, $\phi_s = |\phi_t - \psi_{\rm EP}|$, in 20-60% Au+Au collisions. Statistical errors are smaller than the symbol size. The curves indicate systematic uncertainties due to flow subtraction, and the brackets indicate those due to ZYAM background normalization. Both trigger p_T ranges are shown: (a) $3 < p_T^{(t)} < 4$ GeV/c and (b) $4 < p_T^{(t)} < 6$ GeV/c. The associated particle p_T range is $1 < p_T^{(a)} < 2$ GeV/c. The d+Au results in the π- and double-peak regions are indicated by the solid and hollow arrows, respectively.

Comparison of the relative amplitudes in the π-region and the double-peak region shown in Fig. 11 again reveals the degree of the double-peak structure. In order to study the p_T dependence of the relative amplitudes, Fig. 12(a) and (b) show the amplitude ratios of π-region to double-peak region in slices 1 and 6, respectively. The amplitude ratio in slice 1 increases with $p_T^{(a)}$ for the higher $p_T^{(t)}$ trigger particles. The trend is not much different from that observed in d+Au collisions (shown by the black line). The increasing trend suggests that for in-plane trigger particles the away-side correlation is dominated by physics mechanisms other than double-peak emission, such as punch-though jets and/or back-to-back ridge. The increasing trend may also be present for the lower $p_T^{(t)}$ triggers, but the systematic uncertainty in this analysis prevents a firm conclusion. On the other hand, for slice 6 the amplitude ratio decreases with $p_T^{(a)}$. The away-side jet-like correlation at $\Delta\phi = \pi$ is essentially diminished; what remains are hadrons that form the double-peak structure. It is also worth to note that the away-side amplitude ratio for out-of-plane trigger particles (lower panel of Fig. 12) is significantly smaller than for in-plane trigger particles (upper panel of Fig. 12). This is again the consequence of the significant away-side broadening from in-plane to out-of-plane.

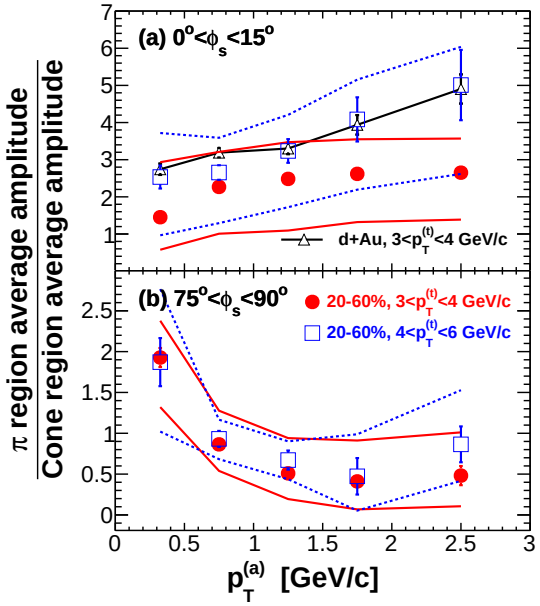

FIG. 12: (Color online) Associated particle $p_T^{(a)}$ dependence of the ratio of away-side dihadron correlation amplitude in the π-region ($|\Delta\phi - \pi| < 0.39$) to that in the double-peak region ($0.81 < |\Delta\phi - \pi| < 1.59$). Two $\phi_s = |\phi_t - \psi_{\rm EP}|$ slices are shown: (a) $0 < \phi_s < \pi/12$ and (b) $5\pi/12 < \phi_s < \pi/2$. The data are from minimum-bias 20-60% Au+Au collisions. Both trigger p_T ranges of $3 < p_T^{(t)} < 4$ GeV/c and $4 < p_T^{(t)} < 6$ GeV/c are shown. Error bars are statistical. The curves indicate systematic uncertainties due to flow subtraction. The systematic uncertainty due to ZYAM background normalization is not shown. The d+Au results are indicated by the open triangles connected by the line in (a), where the error bars are statistical.

C. Discussion on the Near-Side Results

Recall that in Fig. 7, we observe a significant change in the near-side peak amplitude. The near-side amplitude drops with increasing ϕ_s. For the 20-60% centrality, the amplitude at large ϕ_s is not much different from the d+Au result, perhaps indicating minimal medium modification. On the other hand, the amplitude at small ϕ_s appears significantly larger than in d+Au suggesting large medium effect. This might be counterintuitive at first glance. Due to jet-quenching, the near-side jets predominately emerge outward from the surface of the medium, so variation in the medium thickness traversed by the near-side jets between in-plane and out-of-plane directions is not naively expected.

It has been shown by the inclusive dihadron correla-

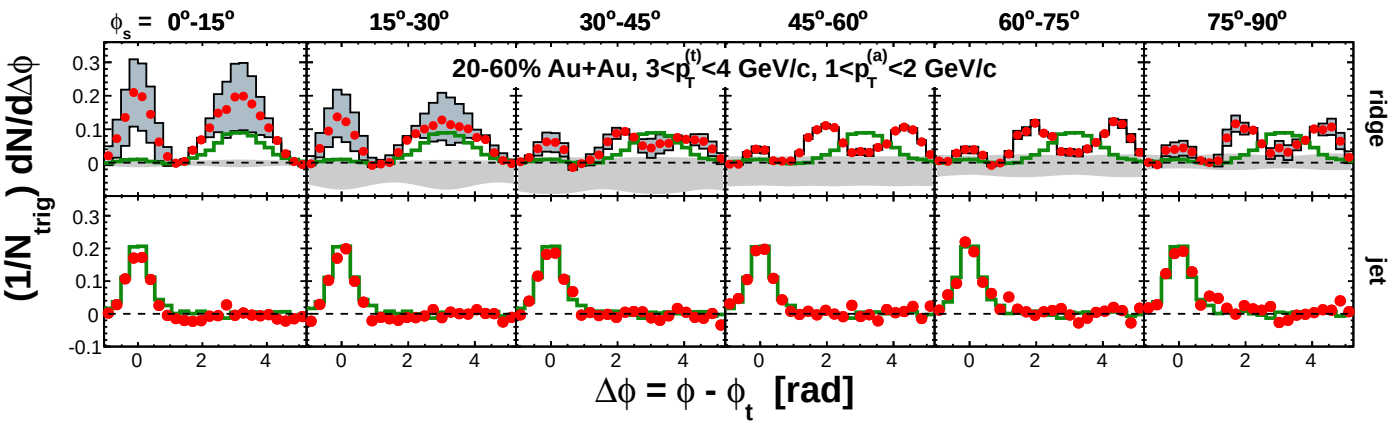

FIG. 13: (Color online) Upper panels: background-subtracted dihadron correlations with trigger particles in six slices of azimuthal angle relative to the event plane, $\phi_s = |\phi_t - \psi_{\rm EP}|$, with a cut on the trigger-associated pseudo-rapidity difference of $|\Delta\eta| > 0.7$. The triangle two-particle $\Delta\eta$ acceptance is not corrected. Statistical errors are smaller than the symbol size. Flow background is subtracted by Eq. (1) using measurements in Table I and the parameterization in Eq. (15). Systematic uncertainties are shown in the black histograms due to flow subtraction and in the horizontal shaded band around zero due to ZYAM background normalization. The near-side correlation is due to the ridge. Lower panels: The difference between raw dihadron correlations in $|\Delta\eta| < 0.7$ and $|\Delta\eta| > 0.7$, after multiplying a coefficient onto the latter such that the resultant difference is zero on average on the away side in the range $|\Delta\phi - \pi| < 1$. This correlation represents the jet-like component of the dihadron correlations. Statistical errors are smaller than the symbol size. Systematic uncertainties are small. The results are for $3 < p_T^{(t)} < 4$ GeV/c and $1 < p_T^{(a)} < 2$ GeV/c in 20-60% Au+Au collisions. In both panels the corresponding inclusive dihadron correlations from d+Au collisions (thick histograms) are superimposed for comparison.

tion that the near-side correlation strength is enhanced in Au+Au with respect to p+p and d+Au collisions [13, 17], and the enhancement is mainly due to the large contribution from the ridge [13, 14]. In order to investigate the underlying physics mechanism for the near-side structure change with trigger particle orientation, we separate contributions from the ridge and the jet-like component by analyzing the correlation data in two different $\Delta\eta$ regions [14]: $|\Delta\eta| > 0.7$ where the ridge is the dominant contributor and $|\Delta\eta| < 0.7$ where both the ridge and jet-like correlations contribute. Figure 13 (upper panel) shows the v_2 and v_4 background-subtracted dihadron correlation function from $|\Delta\eta| > 0.7$ for trigger and associated particle p_T ranges of $3 < p_T^{(t)} < 4$ GeV/c and $1 < p_T^{(a)} < 2$ GeV/c in 20-60% Au+Au collisions. (The $|\Delta\eta| > 0.7$ correlation functions for all kinematic ranges are presented in Appendix C in Figs. 33 and 34.) The near-side correlation for $|\Delta\eta| > 0.7$ is due to the ridge because the jet-like contribution is mostly confined within $|\Delta\eta| < 0.7$. The ridge correlation shows a significant drop with increasing ϕ_s. The ridge contribution is close to zero for trigger particles perpendicular to the reaction plane in the 20-60% centrality bin.

The near-side ridge correlation at large $\Delta\eta$, after two-particle $\Delta\eta$ acceptance correction, was found to be nearly uniform in $\Delta\eta$ [14]. If the ridge is uniform over the entire measured $\Delta\eta$ range, then the ridge can be readily subtracted by taking the difference between the raw (not background-subtracted) correlations from the small and large $\Delta\eta$ regions as

$$\frac{dN_{\rm jet-like}}{d\Delta\phi} = \int_{-0.7}^{0.7} \frac{d^2N_{\rm raw}}{d\Delta\phi d\Delta\eta} d\Delta\eta - \mathcal{A}\left(\int_{-2.0}^{-0.7} \frac{d^2N_{\rm raw}}{d\Delta\phi d\Delta\eta} d\Delta\eta + \int_{0.7}^{2.0} \frac{d^2N_{\rm raw}}{d\Delta\phi d\Delta\eta} d\Delta\eta\right) . \quad (18)$$

The coefficient $\mathcal{A}$ accounts for the $\Delta\eta$ acceptance difference between $|\Delta\eta| < 0.7$ and $|\Delta\eta| > 0.7$, and can be easily obtained from the acceptance ratio of the two $\Delta\eta$ regions. It can also be obtained by requiring the away side of the resultant average correlation magnitude to be zero because the away-side correlation (after $\Delta\eta$ acceptance correction) is also uniform within the measured $\Delta\eta$ range in the TPC [13]. We use the latter method to obtain $\mathcal{A}$ such that the resultant away-side average correlation signal within $|\Delta\phi - \pi| < 1$ is zero, namely

$$\int_{\pi-1}^{\pi+1} d\Delta\phi \int_{-0.7}^{0.7} \frac{d^2N_{\rm raw}}{d\Delta\phi d\Delta\eta} d\Delta\eta - \mathcal{A} \int_{\pi-1}^{\pi+1} d\Delta\phi \left(\int_{-2.0}^{-0.7} \frac{d^2N_{\rm raw}}{d\Delta\phi d\Delta\eta} d\Delta\eta + \int_{0.7}^{2.0} \frac{d^2N_{\rm raw}}{d\Delta\phi d\Delta\eta} d\Delta\eta \right) = 0\,. \tag{19}$$

The obtained coefficient is approximately $\mathcal{A} \approx 1.45$. The resultant difference by Eq. (18) represents the dihadron correlation of the near-side jet-like component under the assumption that the near-side ridge is uniform in $\Delta\eta$ within our measured range. The $\Delta\phi$ correlation of the jet-like component obtained by Eq. (18) is free of large systematic uncertainties because the anisotropic flow, approximately independent of η, is largely cancelled in the difference.

The obtained $\Delta\phi$ correlation of the jet-like component is shown in the lower panel of Fig. 13. The corresponding d+Au result is superimposed on the figure. The $\Delta\phi$ correlation of the jet-like component is approximately independent of the trigger particle orientation, in contrast to the ridge component shown in the upper panel of Fig. 13. The near-side jet-like correlations are consistent between d+Au and Au+Au collisions. The $\Delta\phi$ correlation functions of the jet-like component for all trigger and associated particle p_T ranges are presented in Appendix C in Figs. 35 and 36.

To quantify the near-side modification, we study the ridge and jet-like yields as a function of ϕ_s. We extract the ridge yield in $|\Delta\eta| > 0.7$ and $|\Delta\phi| < 1$ from the ZYAM background-subtracted correlations, such as those in the upper panel of Fig. 13, by

$$\text{Ridge yield} = \frac{1}{N_{\rm trig}} \int_{-1}^{1} d\Delta\phi \left(\int_{-2.0}^{-0.7} \frac{d^2N}{d\Delta\phi d\Delta\eta} d\Delta\eta + \int_{0.7}^{2.0} \frac{d^2N}{d\Delta\phi d\Delta\eta} d\Delta\eta \right)\,. \tag{20}$$

We extract the jet-like yield in $|\Delta\eta| < 0.7$ and $|\Delta\phi| < 1$ from the correlations of the jet-like component, such as those in the lower panel of Fig. 13, by

$$\text{Jet-like yield} = \frac{1}{N_{\rm trig}} \int_{-1}^{1} d\Delta\phi \int_{-0.7}^{0.7} \frac{d^2N}{d\Delta\phi d\Delta\eta} d\Delta\eta\,. \tag{21}$$

Note the $\Delta\eta$ acceptance is not corrected in the $\Delta\phi$ correlations of the ridge or the jet-like component; hence, neither is the extracted corresponding yields. The extracted ridge and jet-like yields are shown in Fig. 14 as a function of ϕ_s in the 20-60% centrality bin. The boxes indicate the total systematic uncertainty; the individual sources of systematic uncertainties and their correlations have been discussed earlier in Sec. III. As seen from Fig. 14, the jet-like yield is approximately independent of ϕ_s in Au+Au collisions, and consistent with the d+Au data. The ridge yield in Au+Au collisions at small ϕ_s (in-plane) is significant, but it decreases quickly with increasing ϕ_s. The ridge yield at large ϕ_s (out-of-plane) is consistent with zero. The ridge is dominated by events where trigger particles are within approximately $\pi/4$ of the event plane.

The trend of decreasing ridge amplitude with increasing ϕ_s is seen in all measured $p_T^{(a)}$ bins. To quantify this, we show in Fig. 15(a) and (b) the $p_T^{(a)}$ dependence of the ratio of ridge yield in $5\pi/12 < \phi_s < \pi/2$ and $\pi/6 < \phi_s < \pi/4$, respectively, to that in $0 < \phi_s < \pi/12$. Both trigger particle $p_T^{(t)}$ selections are shown. The systematic uncertainties, shown for $3 < p_T^{(t)} < 4$ GeV/c in the boxes, have taken into account correlations among the different sources of systematic uncertainties. Within the systematic uncertainty there is no observable difference between the two $p_T^{(t)}$ selections. The ridge ratios from different ϕ_s slices appear to be independent of $p_T^{(a)}$. The ridge decreases with ϕ_s universally for all $p_T^{(a)}$. The ridge yield out-of-plane is consistent with zero at all associated particle $p_T^{(a)}$ for both the trigger particle $p_T^{(t)}$ selections.

Motivated by the preliminary version of our data, Chiu and Hwa [99] suggested that alignment between jet propagation and medium flow direction, likely to be found for in-plane trigger particles, may be responsible for the ridge; radiated gluons (within a small angle of the parton direction) become thermalized with the medium and combine with medium partons to form the ridge when they are aligned in the same direction. This model, called the Correlated Emission Model (CEM), predicts a measurable asymmetry in the $\Delta\phi$ correlation of the near-side ridge for trigger particles on a single side of the event plane [99]. We note that this correlated emission of ridge particles with the medium flow direction may be rather general, not necessarily restricted to the recombination of radiated and medium gluons. For instance, it is possible that initial fluctuations of color flux tubes together with the stronger in-plane transverse flow can produce similar effects [100–105]. We discuss this color flux tube

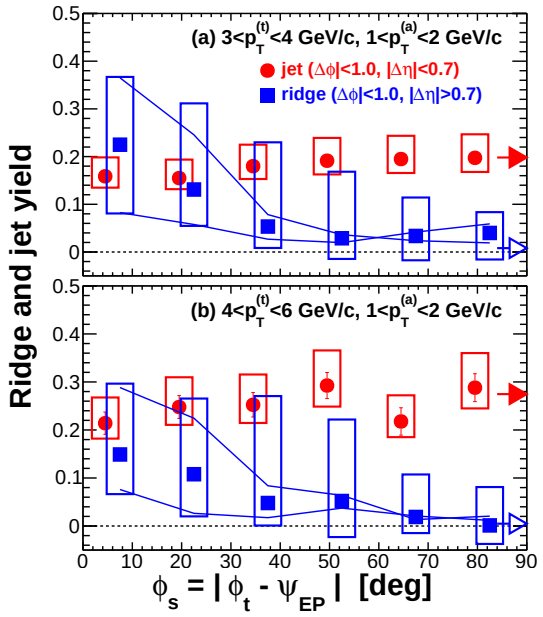

FIG. 14: (Color online) The near-side jet-like and ridge yields as a function of the trigger particle azimuth relative to the event plane, $\phi_s = |\phi_t - \psi_{\rm EP}|$. The results are from 20-60% Au+Au collisions. Two trigger $p_T^{(t)}$ ranges are shown: (a) $3 < p_T^{(t)} < 4$ GeV/c and (b) $4 < p_T^{(t)} < 6$ GeV/c. The associated particle $p_T^{(a)}$ range is $1 < p_T^{(a)} < 2$ GeV/c. The jet-like yield is from $|\Delta\phi| < 1$ and $|\Delta\eta| < 0.7$ and the ridge yield is from $|\Delta\phi| < 1$ and $|\Delta\eta| > 0.7$. Error bars are statistical. The systematic uncertainties are shown by the boxes. For the ridge yield they include those from anisotropic flow (indicated by the curves) and ZYAM background normalization. The systematic uncertainties on the jet-like component are due to leakage of jet-like correlations out to $|\Delta\eta| > 0.7$ and the assumption that the ridge is uniform in $\Delta\eta$. The d+Au results in the jet and ridge regions are indicated by the filled and hallow arrows, respectively.

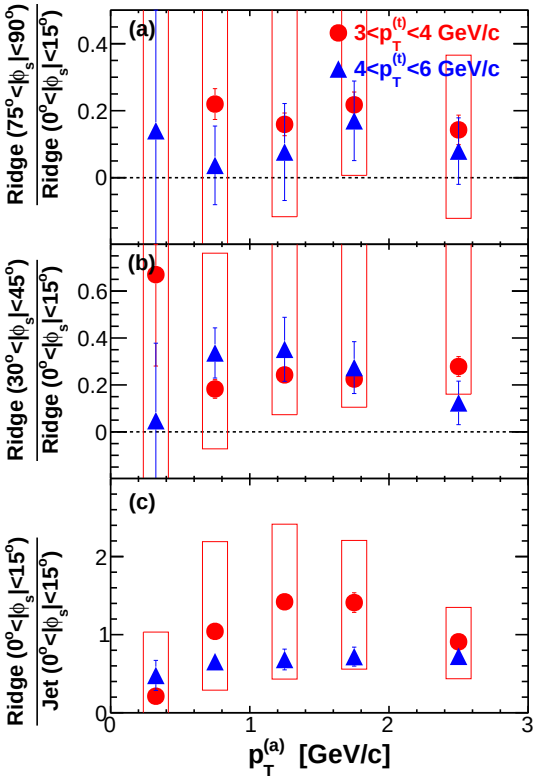

FIG. 15: (Color online) (a) Ratio of the ridge yield from $5\pi/12 < \phi_s < \pi/2$ to that from $0 < \phi_s < \pi/12$. (b) Ratio of the ridge yield from $\pi/6 < \phi_s < \pi/4$ to that from $0 < \phi_s < \pi/12$. (c) Ratio of the ridge yield to the jet-like yield from $0 < \phi_s < \pi/12$. The ridge yield is from $|\Delta\phi| < 1$ and $|\Delta\eta| > 0.7$ and the jet-like yield is from $|\Delta\phi| < 1$ and $|\Delta\eta| < 0.7$. Data are from 20-60% Au+Au collisions. Both trigger $p_T^{(t)}$ ranges of $3 < p_T^{(t)} < 4$ GeV/c and $4 < p_T^{(t)} < 6$ GeV/c are shown. Error bars are statistical. Boxes indicate systematic uncertainties on the $3 < p_T^{(t)} < 4$ GeV/c data; those for $4 < p_T^{(t)} < 6$ GeV/c are similar.

fluctuation model further in Sec. IV D.

There is strong experimental evidence suggesting that the jet-like component and the ridge are produced by different physics mechanisms [15, 55], thus their p_T dependences are expected to be different. To quantitatively study this, we show in Fig. 15(c) the ratio of the ridge yield to the jet-like yield for $0 < \phi_s < \pi/12$. Again, the systematic uncertainties shown in boxes have already taken into account correlations among different sources of systematics. Within the systematic uncertainties, the ridge over jet-like component ratio appears to be constant over the measured $p_T^{(a)}$. This may suggest, on the contrary to the other findings, that the ridge and the jet-like component may be of the same origin. However, it is possible that differences in the $p_T^{(a)}$ spectra of the jet-like and the ridge component are small for our trigger $p_T^{(t)}$ ranges compared to our systematic uncertainties. The p_T spectra of the jet-like component and the ridge will be further discussed below.

D. Connections between Near- and Away-Side

We have observed that the away-side amplitude in the π-region decreases strongly with increasing ϕ_s, so does the near-side ridge amplitude. We have also observed that both the away-side amplitude in the double-peak region and the near-side jet-like amplitude remain approximately constant with ϕ_s. This raises the question whether the near-side and the away-side are connected, or stem from the same physics origin, even though high p_T trigger particles strongly bias the near-side towards surface emission. In order to gain further insights, we study the near- and away-side correlation properties together as a function of ϕ_s and $p_T^{(a)}$.

Figure 16 shows the average correlation amplitudes of the away-side π-region and double-peak region and the near-side ridge and jet-like component. The averages are taken within the same window size of ± 0.39. The ridge

amplitude is scaled by a factor of $1 + \mathcal{A} \approx 2.45$, which is approximately the acceptance factor to scale $|\Delta\eta| > 0.7$ to the entire $\Delta\eta$ range assuming a uniform ridge. The jet-like amplitude and the double-peak region amplitude have a similar dependence on ϕ_s. The similarity suggests that the near-side jet-like component and the away-side double-peak region might be closely related.

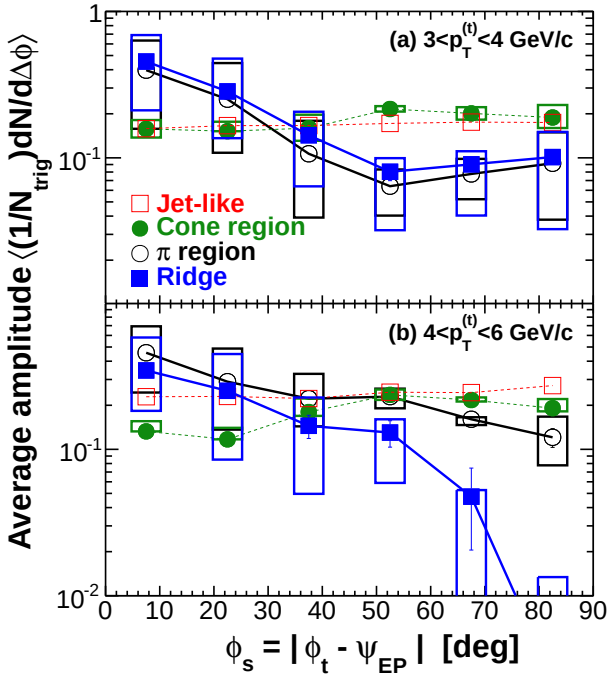

FIG. 16: (Color online) Average correlation amplitude as a function of $\phi_s = |\phi_t - \psi_{\rm EP}|$ for the near-side jet-like component ($|\Delta\phi| < 1$, $|\Delta\eta| < 0.7$), the double-peak region ($|\Delta\phi - \pi \pm 1.2| < 0.39$, $|\eta| < 1$), the π-region ($|\Delta\phi - \pi| < 0.39$, $|\eta| < 1$), and the acceptance-scaled near-side ridge ($|\Delta\phi| < 1$, $|\Delta\eta| > 0.7$). Data are from 20-60% Au+Au collisions. Both trigger $p_T^{(t)}$ selections are shown: (a) $3 < p_T^{(t)} < 4$ GeV/c and (b) $4 < p_T^{(t)} < 6$ GeV/c. The associated particle p_T range is $1 < p_T^{(a)} < 2$ GeV/c for both panels. Error bars are statistical. Boxes indicate systematic uncertainties due to anisotropic flow. The systematic uncertainties due to ZYAM background normalization, common to the π-region, double-peak region and ridge amplitudes, are not shown.

Figure 16 also shows that the ridge amplitude and the away-side π-region amplitude have a similar dependence on ϕ_s. The magnitudes are also similar between the ridge and the π-region. This is especially true for the lower $p_T^{(t)}$ range. On the other hand, the jet-like and double-peak region amplitudes have a rather different dependence on ϕ_s than the ridge and π-region amplitudes. This suggests that the near-side ridge and the away-side π-region may be connected. On the contrary, they seem not connected to the jet-like component or to the component in the double-peak region.

There are many other experimental evidences suggesting that the ridge and the jet-like component may be unrelated in physics despite of the apparent correlation between the ridge and the high p_T trigger particle. For example, three-particle correlations suggest that the production of the jet-like component and the production of the ridge are uncorrelated [15]. The particle composition of the ridge was found to be similar to that of the bulk medium [55]. The ridge magnitude was observed to be rather independent of the trigger particle $p_T^{(t)}$, persisting to very large $p_T^{(t)}$ [14] where jets are almost the sole source of those large $p_T^{(t)}$ trigger particles. The parent parton energies triggered by the wide range $p_T^{(t)}$ trigger particles vary greatly, and yet the ridge is independent of $p_T^{(t)}$. This, again, suggests that the ridge and the jet-like component may be unrelated.

It has been suggested that the ridge may be generated by fluctuations of color flux tubes stretched between the colliding nuclei at the initial time of contact [102–105]. The ridge particles from the color flux tubes near the surface of the collision zone are boosted radially by the medium expansion, becoming correlated in relative azimuth. If the ridge is indeed due to color flux tube fluctuations, i.e. entirely from the medium without connection to high p_T trigger particles, then the meaning of "near side" as defined by the high p_T trigger particle bears no significance to the ridge. In such a case, there ought to exist a ridge partner on the away side due to symmetry, i.e. a back-to-back ridge. In addition, it is conceivable that the ridge would be stronger along the reaction plane direction where both the flux tube strength and the medium flow are stronger. This would naturally explain our observation that the ridge decreases from in-plane to out-of-plane and the ridge amplitude and the π-region amplitude trace other other. The trigger particles in the in-plane direction happen to have ridge particles associated within a narrow $\Delta\phi$ region (near-side), while those trigger particles out-of-plane cannot accidentally pick up ridge particles to be within a narrow $\Delta\phi$ azimuth. In fact, the above mechanism where the ridge particles are aligned with the trigger particle in azimuth is similar to the ridge formation mechanism proposed in CEM [99]; however, the underlying physics is quite different.

Examining the p_T dependences of the different correlation components can give further insights into the physics mechanisms responsible for their formation. We show in Fig. 17 the $p_T^{(a)}$ spectra of the average correlation amplitudes from various $\Delta\phi$ regions, $\frac{dN}{p_T dp_T}$. The upper panels show results for in-plane trigger particles, $0 < \phi_s < \pi/4$. Four $\Delta\phi$ regions are shown: the π-region, the double-peak region, the jet, and the ridge. The lower panels show results for out-of-plane particles, $\pi/4 < \phi_s < \pi/2$. The ridge, which is consistent with zero, is not shown in the lower panel for clarity. Both $p_T^{(t)}$ selections are shown, $3 < p_T^{(t)} < 4$ GeV/c in the left panels and $4 < p_T^{(t)} < 6$ GeV/c in the right panels. Note that the upper panels and the lower panels have the same order of magnitude span in their coordinates,

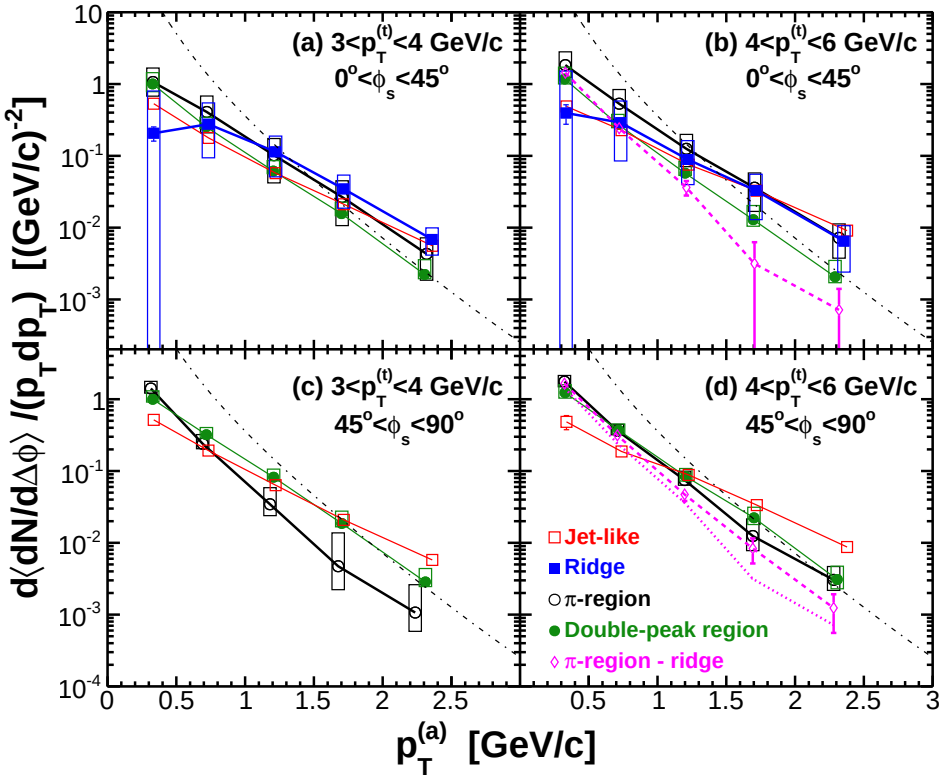

FIG. 17: (Color online) Correlated particle p_T spectra in different $\Delta\phi$ regions: the near-side jet-like component ($|\Delta\phi| < 1$, $|\Delta\eta| < 0.7$), the double-peak region ($|\Delta\phi - \pi \pm 1.2| < 0.39$, $|\eta| < 1$), the π-region ($|\Delta\phi - \pi| < 0.39$, $|\eta| < 1$), and the near-side ridge ($|\Delta\phi| < 1$, $|\Delta\eta| > 0.7$). The ridge amplitude is scaled by the two-particle $\Delta\eta$ acceptance ratio of approximately 2.45. The data are from minimum-bias 20-60% Au+Au collisions. Error bars are statistical. Systematic uncertainties (including those on anisotropic flow and on ZYAM background normalization) are shown as boxes for the double-peak region, the π-region, and the ridge spectra. Two trigger $p_T^{(t)}$ ranges and two ϕ_s regions are shown: (a) $3 < p_T^{(t)} < 4$ GeV/c and $0 < \phi_s < \pi/4$, (b) $4 < p_T^{(t)} < 6$ GeV/c and $0 < \phi_s < \pi/4$, (c) $3 < p_T^{(t)} < 4$ GeV/c and $\pi/4 < \phi_s < \pi/2$, and (d) $4 < p_T^{(t)} < 6$ GeV/c and $\pi/4 < \phi_s < \pi/2$. The dot-dashed curve is the inclusive charged hadron spectrum with an arbitrary normalization. All other lines are to guide the eye. The dotted curves in (d) is replicate of the dashed curve in (b).

TABLE IV: Inverse slope parameter T (MeV/c) from an exponential fit to the associated particle p_T spectra of correlated amplitudes in different $\Delta\phi$ regions: $dN/(p_T dp_T) \propto \exp(-p_T/T)$. Systematic uncertainties for the jet-like spectra and the (π-region $-$ ridge) spectra are small. Statistical and systematic uncertainties on inclusive charged hadron spectrum are both negligible.

	$0 < \phi_s < \pi/4$		$\pi/4 < \phi_s < \pi/2$	
	$3 < p_T^{(t)} < 4$ GeV/c	$4 < p_T^{(t)} < 6$ GeV/c	$3 < p_T^{(t)} < 4$ GeV/c	$4 < p_T^{(t)} < 6$ GeV/c
Jet-like	465 ± 6(stat)	518 ± 13(stat)	460 ± 6(stat)	518 ± 14(stat)
Double-peak region	$331 \pm 2(\text{stat})^{+21}_{-21}(\text{syst})$	$307 \pm 5(\text{stat})^{+27}_{-21}(\text{syst})$	$342 \pm 2(\text{stat})^{+12}_{-3}(\text{syst})$	$335 \pm 4(\text{stat})^{+12}_{-5}(\text{syst})$
π-region	$359 \pm 2(\text{stat})^{+7}_{-31}(\text{syst})$	$360 \pm 4(\text{stat})^{+5}_{-26}(\text{syst})$	$231 \pm 3(\text{stat})^{+47}_{-17}(\text{syst})$	$291 \pm 6(\text{stat})^{+24}_{-13}(\text{syst})$
Ridge	$456 \pm 4(\text{stat})^{+73}_{-38}(\text{syst})$	$444 \pm 12(\text{stat})^{+48}_{-40}(\text{syst})$		
π-region $-$ Ridge		226 ± 14(stat)		249 ± 13(stat)
Inclusive charged hadron	256			

so the spectral shapes can be readily compared.

To investigate the spectral shapes quantitatively, we fit an exponential function to the spectra. The inverse slopes from the fits are tabulated in Table IV. The systematic uncertainties of the fitted inverse slope parameters have already taken into account the correlations in the various sources of systematic uncertainties of the spectra. As expected, the jet-like spectra are harder for the higher trigger $p_T^{(t)}$ range. The difference in the jet-like spectra between in-plane and out-of-plane is small.

On the other hand, the double-peak hadron spectra do not seem to depend on trigger particle $p_T^{(t)}$, nor trigger particle orientation relative to the reaction plane. The double-peak region appears to be universal. In addition, the double-peak hadron spectra are significantly softer than the jet-like spectra, suggesting a different production mechanisms for the near-side jet-like hadrons and the away-side double-peak correlated hadrons. Yet, the hadron yields in the jet-like correlation region and in the double-peak region appear to trace each other. This would be a natural consequence if the away-side parton, in rough energy balance with the near-side jet, loses most of its energy to form the double-peak structure [21].

It is interesting to note that the π-region hadrons are similar to the double-peak hadrons in the in-plane direction; however, in the out-of-plane region they are softer. In fact, the out-of-plane hadrons in the π-region are not much different from the inclusive hadrons in their p_T distributions. In the scenario of only jet-quenching, the in-plane away-side partons do not have enough medium to interact in 20-60% Au+Au collisions to completely wash out their identity. On the other hand, the out-of-plane away-side partons have a longer path-length and the lost energy appears to have equilibrated with the medium, a result found in the inclusive dihadron correlation in central collisions [13].

Surprisingly, the ridge particles are relatively hard, not much softer than the jet-like particle spectra (see Fig. 17 and Table IV). Yet, the ϕ_s dependence of the ridge yield is completely different from that of the jet-like yield. We note that the ridge spectrum measured at larger $p_T^{(a)} > 2$ GeV/c is significantly softer than the jet-like hadron spectrum also at large $p_T^{(a)}$ [14], suggesting that the ridge might be related to the medium. If the ridge comes from the medium, then our result implies that it is not a simple uniform share of medium particles at our measured relatively low $p_T^{(a)}$ because the ridge particles are harder than the bulk medium particles.

For the associated particle p_T range of $1 < p_T^{(a)} < 2$ GeV/c shown in Fig. 16, the π-region amplitude is slightly smaller than the ridge amplitude for $3 < p_T^{(t)} < 4$ GeV/c. For the higher trigger p_T range of $4 < p_T^{(t)} < 6$ GeV/c, there appears an excess of particles in the away-side π-region over those in the near-side ridge for all $p_T^{(a)}$ bins. The excess appears to be insensitive to ϕ_s. Experimentally, it is interesting to examine the p_T dependence of this excess by taking the difference between the away-side π-region and the near-side ridge. This difference is rather robust because all the systematic uncertainties cancel. The difference (excess of particles in the away-side π-region over the near-side ridge) for the trigger particle $4 < p_T^{(t)} < 6$ GeV/c range is shown as diamonds in Fig. 17(b,d). It is remarkable to note that the p_T spectra of those excess particles are rather similar between in-plane and out-of-plane in terms of their inverse slopes. Direct comparison is made in the lower panels where the excess particle spectra in the upper panels are superimposed in the corresponding lower panel as dotted lines. The agreement is excellent. Those excess particles have rather soft p_T's, similar to the inclusive charged hadrons. This is already evident from the ridge and π-region spectra–the away-side π-region spectra are softer than the ridge spectra. If the ridge is generated by fluctuating color flux tubes and is back-to-back [102–105], then the excess particles in the away-side π-region must come from other physics mechanisms. One such mechanism is punch-through jets. However, it is counterintuitive to have a much softer spectrum for punch-through jet-like particles, as well as the agreement between in-plane and out-of-plane directions. Another mechanism is statistical global momentum conservation to balance the extra momentum carried by the ridge particles (because they are harder than the particles in the π-region). However, one may expect a somewhat harder spectrum for the recoil from statistical global momentum conservation than the inclusive spectrum [106].

E. Properties of the Correlation Peaks

To characterize the structure of the correlation functions, we fit the large-$\Delta\eta$ azimuthal correlations with two away-side Gaussian peaks symmetric about $\Delta\phi = \pi$ and two ridge Gaussians (at $\Delta\phi = 0$ and π) with identical widths. We allow the ridge Gaussian magnitudes to vary independently because physics mechanisms other than the back-to-back ridge can also contribute to the π-region as discussed earlier. The fit results are shown by the curves in Fig. 18 for $3 < p_T^{(t)} < 4$ GeV/c and $1 < p_T^{(a)} < 2$ GeV/c as an example. The away-side to near-side ridge ratio for $3 < p_T^{(t)} < 4$ GeV/c is generally larger than unity at low $p_T^{(a)}$ but becomes smaller than unity at large $p_T^{(a)}$. For $4 < p_T^{(t)} < 6$ GeV/c the fit error is too large to draw a firm conclusion.

We study the peak positions and the Gaussian widths of the various components in the dihadron correlation obtained from our four-Gaussian fit. The Gaussian widths are shown in Fig. 19(a) as a function of ϕ_s for the associated particle $p_T^{(a)}$ range of $1 < p_T^{(a)} < 2$ GeV/c. Also shown are the jet-like peak widths in $\Delta\eta$ fit to the near-side $\Delta\eta$ correlation functions ($|\Delta\phi| < 1$), as in Fig. 5. The jet-like peak widths as a function of ϕ_s are flat and are consistent between $\Delta\phi$ and $\Delta\eta$ for this associated $1 < p_T^{(a)} < 2$ GeV/c bin. This again indicates that the jet-like correlation component is independent of the orientation of the trigger particle. The widths for the double peaks and the ridge seem to have some dependence on ϕ_s, being most different in the $\phi_s \sim \pi/3$ region.

Figure 19(b) shows the peak Gaussian widths as a function of $p_T^{(a)}$ for integrated ϕ_s. The jet-like width in $\Delta\phi$ decreases with increasing associated particle $p_T^{(a)}$, consistent with expectations for jet fragmentation. The $\Delta\eta$

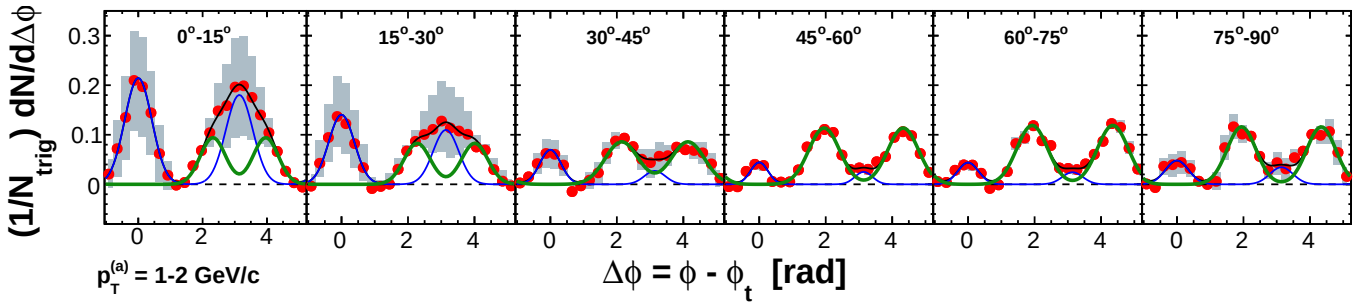

FIG. 18: (Color online) Fit to the background-subtracted $\Delta\phi$ correlation functions at $|\Delta\eta| > 0.7$ in six slices of $\phi_s = |\phi_t - \psi_{\rm EP}|$ by four Gaussians (curves): a near-side Gaussian at $\Delta\phi = 0$ corresponding to the ridge, an away-side Gaussian at $\Delta\phi = \pi$ with identical width to the near-side Gaussian but with varying amplitude, and two identical away-side Gaussians symmetric about $\Delta\phi = \pi$. Data are from 20-60% Au+Au collisions, as same as those in the upper panel of Fig. 13. The trigger and associated particle p_T ranges are $3 < p_T^{(t)} < 4$ GeV/c and $1 < p_T^{(a)} < 2$ GeV/c, respectively. Flow background is subtracted by Eq. (1) using measurements in Table I and the parameterization in Eq. (15). The systematic uncertainties due to elliptic flow are shown by the shaded areas; those due to ZYAM normalization are not shown.

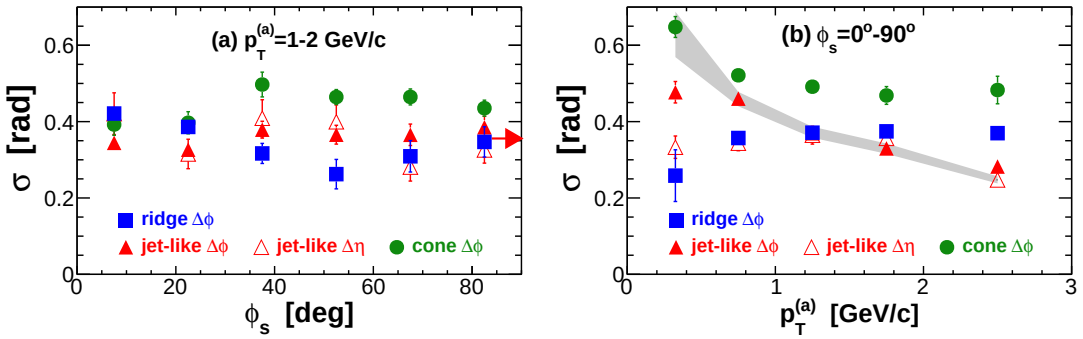

FIG. 19: (Color online) Fit Gaussian widths of the near-side jet-like correlation, the near-side ridge, and the away-side double-peak: (a) as a function of $\phi_s = |\phi_t - \psi_{\rm EP}|$ for $1 < p_T^{(a)} < 2$ GeV/c, and (b) as a function of $p_T^{(a)}$ for the ϕ_s-integrated correlation. The $\Delta\eta$ Gaussian width for the jet-like correlation is also shown. Data are from 20-60% Au+Au collisions. The trigger $p_T^{(t)}$ range is $3 < p_T^{(t)} < 4$ GeV/c. Error bars are statistical only. The near-side jet-like $\Delta\phi$ correlation Gaussion width from the minimum bias d+Au data is indicated by the arrow in (a) and by the shaded area in (b); the width of the shaded area indicates the statistical uncertainty.

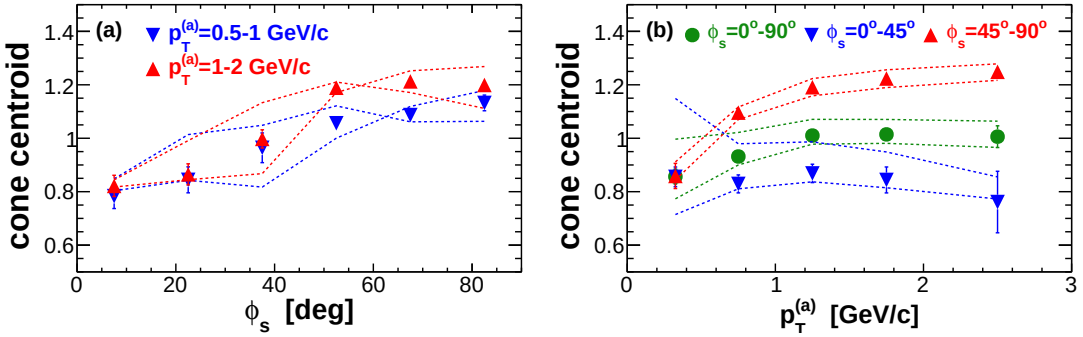

FIG. 20: (Color online) Away-side double-peak position relative to $\Delta\phi = \pi$ from four-Gaussian fits to $\Delta\phi$ correlations at $|\Delta\eta| > 0.7$: (a) as a function of $\phi_s = |\phi_t - \psi_{\rm EP}|$ for two associated particle $p_T^{(a)}$ bins, and (b) as a function of $p_T^{(a)}$ for ϕ_s-integrated as well as in-plane and out-of-plane correlations. Data are from 20-60% Au+Au collisions. The trigger $p_T^{(t)}$ range is $3 < p_T^{(t)} < 4$ GeV/c. Error bars are statistical. The systematic uncertainties due to elliptic flow are indicated by the dashed lines.

width of the jet-like component generally agrees with the $\Delta\phi$ width for $p_T^{(a)} > 1$ GeV/c, but appears narrower than the $\Delta\phi$ width for lower $p_T^{(a)}$. The double-peak width does not vary significantly with $p_T^{(a)}$ except a drop at low $p_T^{(a)}$, and is wider than the near-side jet-like peak. The ridge peak width does not seem to vary with $p_T^{(a)}$ except perhaps an increase at low $p_T^{(a)}$. This is in contrast to the $\Delta\phi$ width of the jet-like peak. This may be taken as a confirmation that the ridge and the jet-like component, both on the near side of the trigger particle, may come from rather different physics mechanisms.

For comparison, we fit the near-side jet-like $\Delta\phi$ correlation in minimum bias d+Au collisions [which was also obtained by the difference between small and large $\Delta\eta$ correlations by Eq. (18)] with a single Gaussian centered at $\Delta\phi = 0$. The fitted Gaussian widths are shown in Fig. 19 by the shaded area whose vertical breaths indicate the statistical uncertainties. The p_T-integrated correlation Gaussian width is shown by the arrow in the left panel. As seen from the figure, the $\Delta\phi$ widths of the near-side jet-like correlations in Au+Au collisions are consistent with those from d+Au collisions at the corresponding p_T. In addition, as shown in Fig. 14, the near-side jet-like yields are the same between Au+Au and d+Au. In fact, the near-side jet-like correlations in Au+Au collisions of all ϕ_s bins are consistent with the minimum bias d+Au data for all $p_T^{(t)}$ and $p_T^{(a)}$ bins, as shown in Figs. 35 and 36. This strongly suggests that the near-side jet-like correlations in Au+Au collisions are result of in-vacuum jet fragmentation, just as in d+Au collisions.

Figure 20(a) shows the fitted double-peak angle as a function of ϕ_s for two associated particle $p_T^{(a)}$ bins. The peak angle increases with increasing ϕ_s, and becomes somewhat different for low and high associated particle $p_T^{(a)}$. The larger double-peak angle for out-of-plane trigger particles may be due to a more significant influence from medium flow. For the in-plane orientation, the away-side double-peak hadrons are likely aligned with the medium flow, receiving only a small deflection to their p_T. Moreover, the overlap collision zone is thinner in the in-plane direction, thus the away-side correlated hadrons can escape the collision zone more easily. For the out-of-plane orientation, on the other hand, the away-side double-peak hadrons move more or less perpendicularly to the medium flow direction because of the long path-length they have to traverse. They receive a large side-kick from the medium flow, broadening their final emission angle.

Figure 20(b) shows the double-peak angle as a function of $p_T^{(a)}$ for in-plane, out-of-plane, and all trigger particle orientations. The peak angle is relatively independent of the associated particle $p_T^{(a)}$ for in-plane trigger particles. They may more closely reflect the average emission angle of correlated away-side hadrons because the medium flow effect is expected to be small, as discussed above.

On the other hand, the double-peak angle for the out-of-plane orientation is larger, consistent with a larger deflection from the medium flow. However, the angle position increases with $p_T^{(a)}$, which is naively not expected if those particles are pushed by media with the same flow velocity. We note that the medium flow can either broaden or shrink the double-peak angle, depending on the relative orientations of the double-peak hadron direction and the direction of the flow. Investigations of medium flow effects on the correlated hadron emission require realistic dynamical modeling which is outside the scope of this paper.

It is also worthwhile to note that the peak positions reported here are from fits to dihadron correlations. They are different from those obtained from three-particle correlations [31] where the away-side correlated hadron angle was found to be independent of the associated particle $p_T^{(a)}$. The angle obtained from the three-particle correlation fit is cleaner because the peaks are more cleanly separated in the two-dimensional angular space, while the fit to dihadron correlations is more affected by other physics effects. One such effect is jet deflection [107, 108], which was found to be present by three-particle correlations where the diagonal peaks are stronger than the off-diagonal peaks [31].

F. Effect of Higher Order Harmonics

It has been suggested by the NeXSPheRIO model [105, 109–113] that initial energy density fluctuations (hot spots) with subsequent hydro evolution may generate a near-side ridge and a double-peak correlation on the away side. The physics mechanism appears to be side-splashes of particles by the hot spot on the surface resulting in two peaks in the single particle azimuthal distribution event-by-event separated by about two radians [109, 110]. These two-peaked single particle distributions produce two-particle correlations of a near-side ridge and an away-side double peak. The near-side ridge and the away-side double peak are due to the same physics, and the near-side ridge amplitude should be larger (by a factor of two) than each of the two away-side peaks. This relative amplitude is a unique feature of the NeXSPheRIO model because of the topology of particle distributions in the model [109, 110]. This feature is not observed in the out-of-plane large $\Delta\eta$ correlations in data.

It has also been shown based on the AMPT, UrQMD and other models that incorporate Glauber initial geometry [30, 65, 67, 68, 114, 115] that there can be large triangularity in the initial collision geometry event-by-event and those initial geometry fluctuations could produce a triangular anisotropy (triangular flow) in the final momentum space. Such triangular flow would result in three peaks at $\Delta\phi = 0$, $2\pi/3$, and $4\pi/3$ in the two-particle correlation, which appear to be qualitively consistent with the inclusive dihadron correlation data integrated over all reaction plane directions [16, 17].

Hydrodynamic calculations [69–73, 116–121], incorpo-

rating event-by-event fluctuations in the initial collision geometry, all confirm the existence of v_3 and higher-order harmonics in the azimuthal distributions of final-state hadrons. The hydrodynamic evolutions translate the initial configuration space anisotropy (and fluctuations) into final-state momentum anisotropy. The triangular anisotropy v_3 has been measured at RHIC [80, 81, 122–125] with the event-plane as well as the two-particle cumulant method. Event-by-event hydrodynamic calculations are able to reproduce the measurements qualitatively, and in some cases even quantitatively [82].

Because the minor axis direction of the initial fluctuating triangular geometry is random with respect to the reaction plane or the participant plane [75, 76], the three-peak structure in two-particle correlation from triangular flow should be independent of ϕ_s. However, the near-side peak of our dihadron correlation data decreases with increasing ϕ_s and is consistent with zero at large $\Delta\eta$ with trigger particles out-of-plane, as shown in the upper panel of Fig. 13 as well as in Figs. 33 and 34. The ϕ_s dependence of the observed correlation structures suggests that the ridge-like correlation is unlikely due solely to the possible triangular flow.

1. *Subtraction of v_3*

In order to make a quantitative estimate of the v_3 effect on our dihadron correlations, we measure the v_3 using STAR data and apply flow background subtraction including v_3 by Eq. (10). We obtain v_3 of trigger and associated particles using the two-particle cumulant method with a reference particle of $0.15 < p_T < 2$ GeV/c by Eq. (12). A η-gap of 0.7 is applied between the particle of interest and the reference particle, similar to the $v_2\{2\}$ described in Sec. II B. The $v_3\{2, \eta_{\rm gap}{=}0.7\}$ values are listed in Table V. Also listed are the $v_4\{2, \eta_{\rm gap}{=}0.7\}$ values which will be discussed later.

TABLE V: Triangular and quadrangular anisotropies, $v_3\{2\}$ and $v_4\{2\}$, measured by the two-particle cumulant method (with a reference particle) as a function of p_T in 20-60% minimum-bias Au+Au collisions. An $\eta_{\rm gap} = 0.7$ is applied. The errors are statistical.

p_T (GeV/c)	$v_3\{2, \eta_{\rm gap}{=}0.7\}$	$v_4\{2, \eta_{\rm gap}{=}0.7\}$
0.15 - 0.5	0.0079 ± 0.0002	0.0019 ± 0.0004
0.5 - 1	0.0246 ± 0.0002	0.0080 ± 0.0006
1 - 1.5	0.0482 ± 0.0004	0.0236 ± 0.0010
1.5 - 2	0.0688 ± 0.0007	0.0376 ± 0.0018
2 - 3	0.0858 ± 0.0012	0.0558 ± 0.0028
3 - 4	0.0905 ± 0.0038	0.0648 ± 0.0088
4 - 6	0.0748 ± 0.0092	0.0687 ± 0.0214

Figure 21 shows the dihadron correlation functions for $|\Delta\eta| > 0.7$ and $3 < p_T^{(t)} < 4$ GeV/c obtained with $v_3\{2\}$ included in the background subtraction. The change from Fig. 13 is the additional subtraction of the $v_3\{2\}$ contribution. As seen from Fig. 21, the qualitative features of the correlation functions are unchanged from those in the upper panels of Fig. 13. The away-side double-peak structure out-of-plane remains prominent. The decreasing trend of the ridge magnitude from in-plane to out-of-plane is unaffected because a constant v_3 contribution over ϕ_s is subtracted. This demonstrates that the main features of the measured near-side ridge and away-side double peak in the dihadron correlations with high p_T trigger particles, whether or not integrated over ϕ_s, are unlikely due solely to the possible triangular flow contributions, but other physics mechanisms.

2. *Subtraction of uncorrelated v_4*

We have so far subtracted the $v_4\{\psi_2\}$ background correlated with the second harmonic plane, ψ_2, by Eq. (1) and Eq. (10). We have used the parameterization of Eq. (15) to the previous $v_4\{\psi_2\}$ measurement [45]. There is an additional contribution to v_4 that is uncorrelated to ψ_2 and arises from fluctuations. The uncorrelated component can be obtained by

$$V_4\{\rm uc\} = v_4^{(t)}\{2\}v_4^{(a)}\{2\} - v_4^{(t)}\{\psi_2\}v_4^{(a)}\{\psi_2\}\,. \qquad (22)$$

where $v_4\{2\}$ is the two-particle cumulant v_4 with $\eta_{\rm gap} = 0.7$ given in Table V.

The flow background including the uncorrelated $V_4\{\rm uc\}$ is given by Eq. (11). Figure 22 shows the dihadron correlation functions for $|\Delta\eta| > 0.7$ and $3 < p_T^{(t)} < 4$ GeV/c obtained with additional $V_4\{\rm uc\}$ included in the background subtraction. As can be seen, the correlation results are effectively as same as those shown in Fig. 21. This is because $V_4\{\rm uc\}$ is small for the 20-60% centrality and its effect on dihadron correlation is negligible.

3. *Subtraction of ϕ_s-Dependent v_2*

One can always attribute all azimuthal dependence to Fourier harmonics. In fact, Luzum [126] argued that our $|\Delta\eta| > 0.7$ correlation data can be fitted by Fourier harmonics upto the $4^{\rm th}$ order and the fitted coefficients are consistent with features expected from anisotropic flows. This is not supprising because nonflow effects, which must be contained in the fitted Fourier coefficients, are relatively small compared to the flow contributions in our kinematic regions. If the observed ϕ_s-dependent ridge is due to anisotropic flow, then the harmonic flows must be ϕ_s-dependent. This may not be impossible because the requirement of trigger particles in a particular ϕ_s bin from the event plane reconstructed from particles in $0.15 < p_T < 2$ GeV/c could preferentially select events with associated particle v_2 displaced from the average. In the following, we analyze the two-particle cumulant

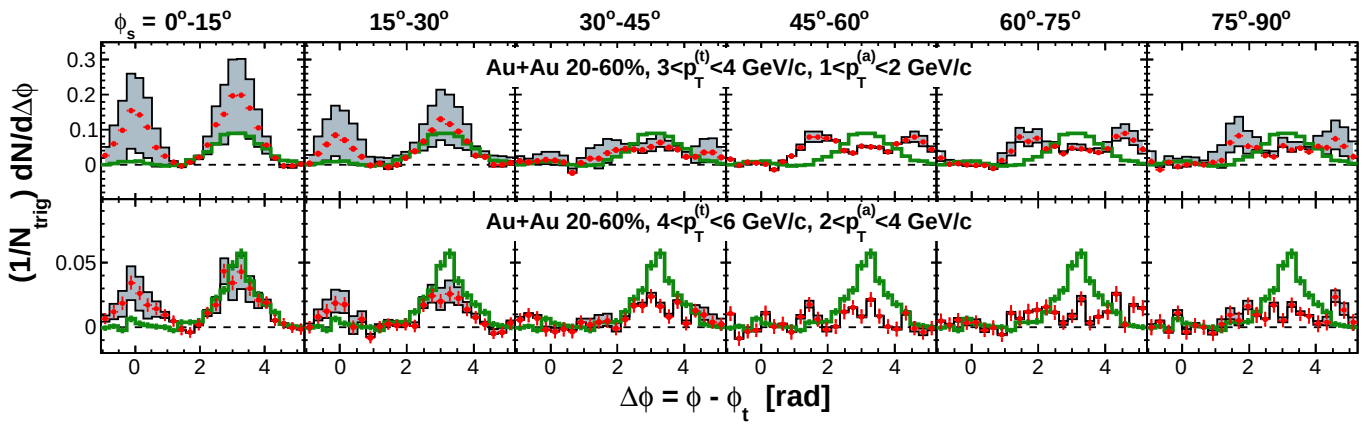

FIG. 21: (Color online) Background-subtracted dihadron correlations with trigger particles in six slices of azimuthal angle relative to the event plane, $\phi_s = |\phi_t - \psi_{\rm EP}|$, with a cut on the trigger-associated pseudo-rapidity difference of $|\Delta\eta| > 0.7$. The triangle two-particle $\Delta\eta$ acceptance is not corrected. The trigger and associated particle p_T ranges are $3 < p_T^{(t)} < 4$ GeV/c and $1 < p_T^{(a)} < 2$ GeV/c (upper panel), and $4 < p_T^{(t)} < 6$ GeV/c and $2 < p_T^{(a)} < 4$ GeV/c (lower panel), respectively. The data points are from minimum-bias 20-60% Au+Au collisions. Flow background is subtracted by Eq. (10) using v_2 measurements in Table I and v_3 in Table V and the parameterization in Eq. (15). Systematic uncertainties due to flow subtraction are shown in the thin histograms embracing the shaded area; those due to ZYAM normalization are not shown. Error bars are statistical. For comparison, the inclusive dihadron correlations from d+Au collisions are superimposed as the thick (green) histograms (only statistical errors are depicted).

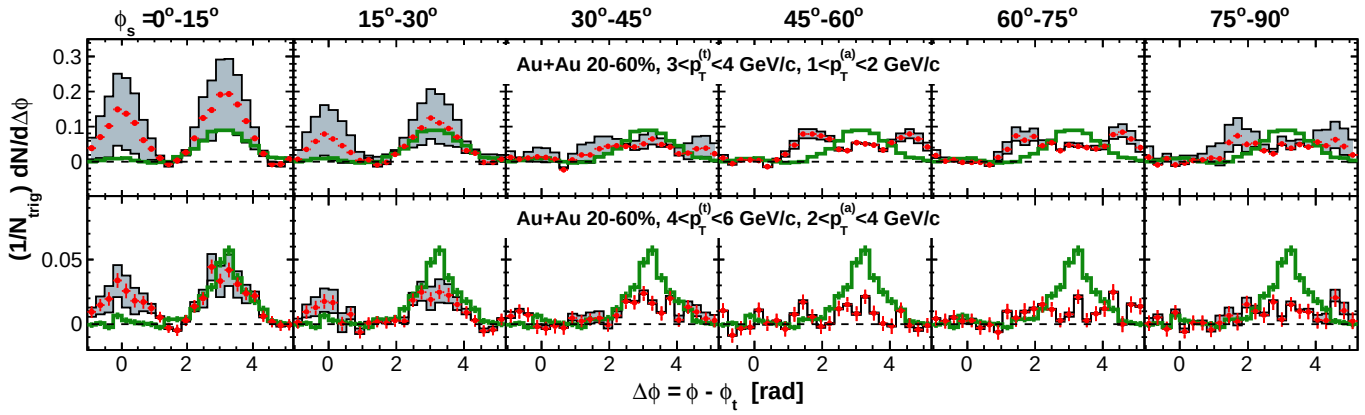

FIG. 22: (Color online) As same as Fig. 21, except with subtraction of an additional background of $V_4\{\rm uc\}$ uncorrelated to the second harmonic event plane (ψ_2). The data in the upper panels have been published in Ref. [35].

v_n in events of different ϕ_s values separately, and subtract them from the dihadron correlations.

Since reference particles are used to reconstruct the EP to determine the ϕ_s, one cannot calculate v_n from cumulant of the associated particle and a reference particle in event sample selected according to ϕ_s. Instead, we form two-particle cumulant from particles in a given associated $p_T^{(a)}$ bin, applying η-gap of 0.7. The v_n of the associated particles are simply the square root of the cumulants:

$$v_n\{p_T\text{-}p_T\}(\phi_s) = \sqrt{V_n\{p_T\text{-}p_T, \eta_{\rm gap}{=}0.7\}(\phi_s)}\,. \qquad (23)$$

Here $V_n\{p_T\text{-}p_T, \eta_{\rm gap}{=}0.7\}$ indicates the two-particle cumulant with particle pairs from the same p_T bin. We use $v_n\{p_T\text{-}p_T, \eta_{\rm gap}{=}0.7\}$ or simply $v_n\{p_T\text{-}p_T\}$ to stand for the resultant anisotropy measurement. Figure 23 shows the obtained $v_n\{p_T\text{-}p_T\}$ of $1.5 < p_T < 2$ GeV/c as a function of ϕ_s of trigger particles of $3 < p_T^{(t)} < 4$ GeV/c. The $v_2\{p_T\text{-}p_T\}$ decreases with ϕ_s. The decrease is a consequence of the decreasing ridge with increasing ϕ_s. The $v_4\{p_T\text{-}p_T\}$ is found to be smallest with $\phi_s = 45°$ and largest with $\phi_s = 0°$ and 90°. On the other hand, the $v_3\{p_T\text{-}p_T\}$ is independent of ϕ_s, consistent with the expectation that the third and second harmonic planes are uncorrelated at mid-rapidity. The $v_3\{p_T\text{-}p_T\}$ from the cumulant of same-p_T bin pairs is consistent with that obtained from the cumulant with a reference particle, $v_3\{2\}$, given in Table V. The $v_2\{p_T\text{-}p_T\}$ values are listed in Table VI as a function of p_T and ϕ_s. Results

for two $\eta_{\rm gap}$ values are listed, $v_2\{p_T\text{-}p_T, \eta_{\rm gap}{=}0.7\}$ and $v_2\{p_T\text{-}p_T, \eta_{\rm gap}{=}1.2\}$, to estimate the range of $v_2\{p_T\text{-}p_T\}$.

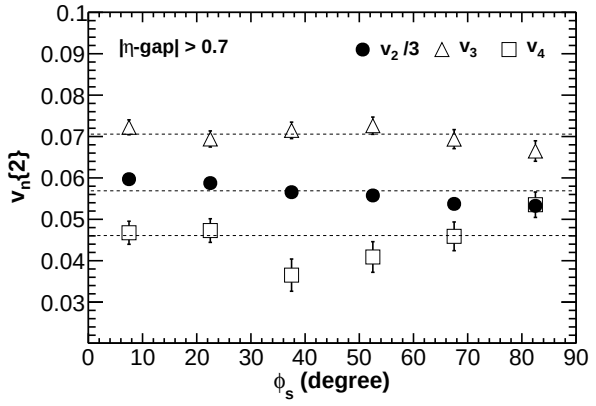

FIG. 23: Harmonic $v_n\{p_T\text{-}p_T\}$ of associated particles of $1.5 < p_T^{(a)} < 2$ GeV/c as a function of ϕ_s of trigger particles of $3 < p_T^{(t)} < 4$ GeV/c. Note the $v_2\{p_T\text{-}p_T\}$ is scaled down by a factor of 3 to fit into the plot coordinate range. The $v_n\{p_T\text{-}p_T\}$ is measured by the two-particle cumulant method with particle pairs from the same associated $p_T^{(a)}$ bin and with $\eta_{\rm gap} = 0.7$. The data are from minimum-bias 20-60% Au+Au collisions. Error bars are statistical. The horizontal lines are to guide the eye.

Although the measured $v_4\{p_T\text{-}p_T\}$ is ϕ_s-dependent, the contribution of the ψ_2-uncorrelated v_4 to flow background is negligibly small, as discussed in Sec. IV F 2. We therefore use the ϕ_s-independent $v_4\{2\}$ measured by two-particle cumulant with a reference particle, as in Sec. IV F 2. We have checked our results using the ϕ_s-dependent $v_4\{p_T\text{-}p_T\}$ and found no observable difference.

In the following we subtract flow background using the ϕ_s-dependent $v_2\{p_T\text{-}p_T\}(\phi_s)$, as discussed above and tabulated in Table VI. The trigger particle v_2 is still given by the two-particle cumulant flow obtained with a reference particle from Table I as in Sec. II B. This is because the trigger v_2 is the second harmonic modulation of trigger particles which determines the ϕ_s. The flow background is given by Eq. (11) and is normalized by ZYAM. Figure 24 shows the dihadron correlation results for $3 < p_T^{(t)} < 4$ GeV/c and $|\Delta\eta| > 0.7$ with subtraction of ϕ_s-dependent $v_2\{p_T\text{-}p_T\}$. The change from the lower systematic bound in Fig. 21 is the subtraction of the ϕ_s-dependent v_2 in place of the ϕ_s-independent one.

As seen from Fig. 24, the near-side ridge is diminished, maybe as expected, because the large $\Delta\eta$ ridge is presumbaly included in the subtracted v_n. However, it is important to point out that it is not automatically guaranteed that the ridge will be gone just because the v_n's are measured by two-particle cumulant either with a reference particle or with a particle from the same p_T region. This is because they are not simply measured by the trigger-associated particle pair at $|\Delta\eta| > 0.7$. If they were, then the correlation will be strictly zero everywhere, both on the near side and on the away side. This would be similar to the fitting method in Ref. [85] where the large $\Delta\eta$ region on the near side is fitted and treated as background Fourier coefficients. Such Fourier coefficients would be inevitably ϕ_s-dependent, and the near-side ridge would by definition be zero.

It is interesting to note, despite of the diminished near-side ridge, that the away-side correlation is not diminished. It still evolves from a single peak with in-plane trigger particles to a double peak with out-of-plane trigger particles. The observation of the away-side double-peak structure for out-of-plane triggers seems robust against the wide range of flow background subtraction.

It is worthwhile to note that, if v_2 depends on ϕ_s, then the factorization of $v_2^{(t)}$ and $v_2^{(a)}$ in inclusive dihadron correlation analysis is no longer valid and the flow background there may be underestimated. This is discussed in Appendix B.

As noted in Sec. II C we have neglected the effect of dipole fluctuations (rapidity-even v_1) in flow background subtraction. STAR measurements [127, 128] indicate that the dipole fluctuation effect changes sign at $p_T \approx 1$ GeV/c, negative at lower p_T and positive at higher p_T. For $p_T^{(a)} =$ 1-2 GeV/c shown in Fig. 24, the dipole fluctuation effect is approximately zero and can be neglected. The qualitative conclusions on the near-side and away-side correlations are therefore unaffected by the potential dipole fluctuations.

Figure 39 shows results similar to Fig. 24 but for other associated $p_T^{(a)}$ bins. Figure 40 shows the results for $4 < p_T^{(t)} < 6$ GeV/c. For all kinematic cuts studied, the near-side ridges seem all vanished after the subtraction of the ϕ_s-dependent $v_2\{p_T\text{-}p_T\}$, the two-particle cumulant $v_3\{2\}$, and the ψ_2-correlated $v_4\{\psi_2\}$ and uncorrelated $v_4\{\rm uc\}$. The evolution of the away-side correlation function from in-plane to out-of-plane appears different for high and low associated $p_T^{(a)}$. At relatively high $p_T^{(a)}$, the away-side correlation is single-peaked for in-plane triggers and double-peaked for out-of-plane triggers, as already noted earlier in Fig. 24. At low $p_T^{(a)}$, however, the trend is opposite–the away-side correlation is double-peaked in-plane and single-peaked out-of-plane. As noted above we have neglected the effect of dipole fluctuations in flow background subtraction. The effect of dipole fluctuations is negative at low $p_T^{(a)}$. It may be responsible for the concave shape of the near-side correlation. However, the away-side correlation shape would be more strongly double-peaked after the subtraction of a negative dipole background. Thus the qualitative conclusion of the double-peaked away-side correlations at low $p_T^{(a)}$ for in-plane triggers seems robust.

Since the ridge is diminished after subtraction of ϕ_s-dependent v_2 from two-particle cumulant at large $\Delta\eta$, can we conclude that the physics origin of the ridge is hydrodynamic v_n flow? The answer is no because any non-hydrodynamic origin of v_n is also included in the two-particle v_n measurements. In other words, any ridge signal (whatever its physics origin might be) is included

TABLE VI: Elliptic flow anisotropy, $v_2\{p_T\text{-}p_T\}$, measured by the two-particle cumulant method using pairs from the same p_T bin, as a function of p_T and ϕ_s in 20-60% minimum-bias Au+Au collisions. Two $\eta_{\rm gap}$ values (0.7 and 1.2) are used. Errors are statistical.

$p_T^{(a)}$ (GeV/c)	$0-\pi/12$	$\pi/12-\pi/6$	$\pi/6-\pi/4$	$\pi/4-\pi/3$	$\pi/3-5\pi/12$	$5\pi/12-\pi/2$
			$v_2\{p_T\text{-}p_T, \eta_{\rm gap}=0.7\}$			
0.15 - 0.5	0.0432 ± 0.0002	0.0421 ± 0.0003	0.0416 ± 0.0003	0.0403 ± 0.0003	0.0393 ± 0.0003	0.0379 ± 0.0004
0.5 - 1	0.0923 ± 0.0002	0.0916 ± 0.0002	0.0903 ± 0.0002	0.0878 ± 0.0002	0.0858 ± 0.0002	0.0854 ± 0.0002
1 - 1.5	0.1427 ± 0.0003	0.1399 ± 0.0003	0.1371 ± 0.0004	0.1347 ± 0.0004	0.1301 ± 0.0004	0.1296 ± 0.0004
1.5 - 2	0.1791 ± 0.0007	0.1763 ± 0.0008	0.1697 ± 0.0008	0.1673 ± 0.0009	0.1612 ± 0.0010	0.1598 ± 0.0010
2 - 3	0.2108 ± 0.0015	0.2081 ± 0.0016	0.1976 ± 0.0018	0.1905 ± 0.0020	0.1860 ± 0.0021	0.1885 ± 0.0022
			$v_2\{p_T\text{-}p_T, \eta_{\rm gap}=1.2\}$			
0.15 - 0.5	0.0435 ± 0.0004	0.0422 ± 0.0005	0.0417 ± 0.0005	0.0403 ± 0.0006	0.0397 ± 0.0006	0.0366 ± 0.0007
0.5 - 1	0.0914 ± 0.0003	0.0903 ± 0.0004	0.0891 ± 0.0004	0.0861 ± 0.0004	0.0850 ± 0.0004	0.0843 ± 0.0005
1 - 1.5	0.1409 ± 0.0006	0.1401 ± 0.0006	0.1356 ± 0.0007	0.1324 ± 0.0007	0.1297 ± 0.0008	0.1274 ± 0.0008
1.5 - 2	0.1752 ± 0.0013	0.1755 ± 0.0014	0.1673 ± 0.0015	0.1649 ± 0.0017	0.1593 ± 0.0018	0.1553 ± 0.0019
2 - 3	0.2136 ± 0.0027	0.2037 ± 0.0030	0.1963 ± 0.0032	0.1959 ± 0.0035	0.1773 ± 0.0040	0.1863 ± 0.0040

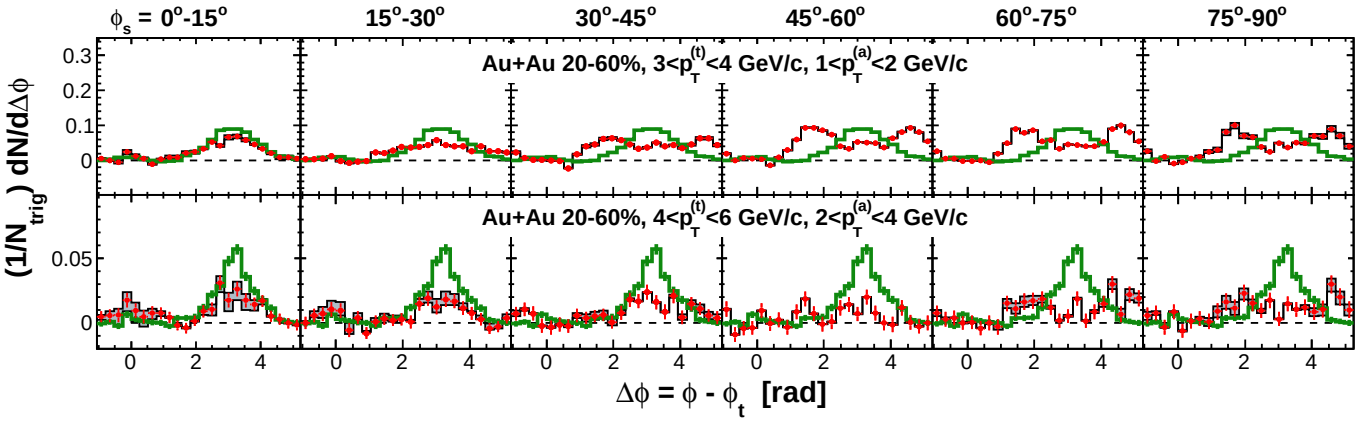

FIG. 24: (Color online) Background-subtracted dihadron correlations with trigger particles in six slices of azimuthal angle relative to the event plane, $\phi_s = |\phi_t - \psi_{\rm EP}|$, with a cut on the trigger-associated pseudo-rapidity difference of $|\Delta\eta| > 0.7$. The triangle two-particle $\Delta\eta$ acceptance is not corrected. The trigger and associated particle p_T ranges are $3 < p_T^{(t)} < 4$ GeV/c and $1 < p_T^{(a)} < 2$ GeV/c (upper panel), and $4 < p_T^{(t)} < 6$ GeV/c and $2 < p_T^{(a)} < 4$ GeV/c (lower panel), respectively. The data points are from minimum-bias 20-60% Au+Au collisions. Flow background is subtracted by Eq. (11). The ϕ_s-dependent $v_2\{p_T\text{-}p_T\}$ measured by two-particle cumulants with $\eta_{\rm gap} = 0.7$ and 1.2 in Table VI are used (the thin histograms embracing the shaded area), with their average shown in the data points. The subtracted $v_3\{2\}$ is given in Table V. The subtracted $v_4\{\psi_2\}$ is parameterized by Eq. (15), and the $V_4\{\rm uc\}$ is given by Eq. (22). Error bars are statistical; systematic uncertainties are not shown. The shaded areas show the range of the results using $v_2\{p_T\text{-}p_T\}$ values from two η-gaps of 0.7 and 1.2. For comparison, the inclusive dihadron correlations from d+Au collisions are superimposed as the thick (green) histograms.

in v_n, and the ridge would be subtracted after subtraction of v_n. However, one also cannot rule out the ridge being part of hydrodynamic flow. This is because it is still possible that hydrodynamic flow of the underlying event is biased by the selection of the trigger particle orientation, and all the long-range $\Delta\eta$ correlation may be indeed due to flow.

V. CONCLUSIONS

Dihadron azimuthal correlations in non-central 20-60% Au+Au collisions are reported by the STAR experiment as a function of trigger particle azimuthal angle relative to the event plane ($\phi_s = |\phi_t - \psi_{\rm EP}|$) in six equal-size slices. The correlations are first studied with subtraction of the even harmonic elliptic and quadrangular flow backgrounds. The ϕ_s dependence of the dihadron correlation signal, as well as the trigger and associated particle transverse momentum (p_T) dependences, are studied. Minimum-bias d+Au collision data are presented for

comparisons. The correlation functions are also obtained for small and large pseudo-rapidity separations ($|\Delta\eta|$) independently in order to isolate the jet-like and ridge (long range $\Delta\eta$ correlation) contributions. The resulting jet-like and ridge components are studied as a function of ϕ_s, trigger particle $p_T^{(t)}$ and associated particle $p_T^{(a)}$.

The ZYAM background subtraction method is described in detail. The flow subtraction is carried out to the order of v_2v_4. The systematic uncertainties in the background subtraction are extensively discussed. The effect of the triangular flow harmonic is not subtracted in the results quantitatively characterizing the main features of the correlation function in the jet-like versus ridge-like regions. However, the effects of triangular flow fluctuations, as well as ϕ_s-dependent elliptic flow, on these main features are investigated and discussed.

The dihadron correlations are strongly modified in Au+Au collisions with respect to minimum-bias d+Au collisions. The modifications strongly depend on the trigger particle orientation relative to the event plane and evolve with associated particle $p_T^{(a)}$. No significant changes are observed between trigger particle $p_T^{(t)}$ ranges of $3 < p_T^{(t)} < 4$ GeV/c and $4 < p_T^{(t)} < 6$ GeV/c. The ϕ_s and $p_T^{(a)}$ dependences of the correlation functions are quantitatively similar in the two trigger particle $p_T^{(t)}$ ranges.

The away-side dihadron correlation broadens from in-plane to out-of-plane. The away-side correlation for $\phi_s < \pi/6$ is single-peaked, independent of $p_T^{(a)}$, and not much wider than in d+Au, while the amplitude is larger than the d+Au data. For $\phi_s > \pi/6$, the away-side double-peak structure starts to develop and becomes stronger for increasing ϕ_s and increasing $p_T^{(a)}$. The strongest double-peak structure is found at large $p_T^{(a)}$ in the out-of-plane direction.

The away-side dihadron correlation amplitude at $\Delta\phi = \pi$ drops from in-plane to out-of-plane, while that in the double-peak region remains approximately constant over ϕ_s. For in-plane ϕ_s, the amplitude ratio in the π-region to the double-peak region increases with $p_T^{(a)}$, consistent with d+Au and qualitatively consistent with punch-through jets or away-side jets not interacting with the medium. However, the individual amplitudes in these two regions are both higher than in d+Au, suggesting other physics mechanisms at work. For out-of-plane ϕ_s, the amplitude ratio decreases strongly with $p_T^{(a)}$, opposite to expectations from punch-through jets.

The near-side dihadron correlation amplitude decreases with increasing ϕ_s. The decrease comes entirely from the decrease in the ridge. The ridge is extracted from correlations at $|\Delta\eta| > 0.7$. Its amplitude is found to decrease with increasing ϕ_s significantly in the 20-60% centrality. This feature is present for all associated particle $p_T^{(a)}$, and appears to be independent of $p_T^{(a)}$.

The jet-like contribution to the near-side correlation is extracted from the difference between small- and large-$\Delta\eta$ azimuthal correlations, subject to small experimental systematic uncertainties. The jet-like contribution is invariant from in-plane to out-of-plane within our systematic uncertainties, and is found to be the same as in d+Au collisions.

The different behaviors of the jet-like component and the ridge with respect to ϕ_s suggest that their production mechanisms are different. The jet-like component is insensitive to the reaction plane and appears to be universal, suggesting in-vacuum jet-fragmentation of partons whose production is biased towards the surface of the collision zone by requiring the high p_T trigger particles. The strong dependence of the ridge on the reaction plane suggests its origin to be connected to the medium, not to the jet.

There might be strong connections between the near- and aways-side of the dihadron correlations. It is found that the near-side jet-like yield and the away-side double-peak yield both have little dependence on ϕ_s. The jet-like spectral shape and the double-peak hadron spectral shape do not change with ϕ_s, and the double-peak region spectra are not much softer than the jet-like spectra. The jet-like spectrum for $4 < p_T^{(t)} < 6$ GeV/c is somewhat harder than that for $3 < p_T^{(t)} < 4$ GeV/c, while the double-peak hadron spectra remain the same between the two trigger $p_T^{(t)}$ ranges.

On the other hand, the near-side ridge and the away-side π-region appear to trace each other as a function of ϕ_s, and also approximately as a function of $p_T^{(a)}$, suggesting the possibility of a back-to-back ridge. This would be consistent with the recent suggestion that the ridge may be generated by fluctuations in the initial color flux tubes focused by transverse radial flow. Such a picture would also explain the decreasing ridge from in-plane to out-of-plane because both the color flux tubes and the radial flow are the strongest along the in-plane direction. However, it remains unclear why the ridge particles are much harder than inclusive hadrons in our measured $p_T^{(a)}$ region.

The dihadron correlation structure is fit with a four-Gaussian model representing a back-to-back ridge and an away-side double peak. The fitted away-side double-peak angle increases from in-plane to out-of-plane. For in-plane trigger particles, the fitted double-peak angle is approximately constant over the associated particle $p_T^{(a)}$; For out-of-plane trigger particles, it increases with $p_T^{(a)}$. Whether and how much the medium flow influences the emission directions of the away-side correlated particles warrants further investigations.

The dihadron correlations are further studied with subtraction of triangular anisotropy (v_3) independent of ϕ_s. The v_3 is measured by the two-particle cumulant method with a η-gap ($\eta_{\rm gap}$) of 0.7; The triangular anisotropy with larger $\eta_{\rm gap}$ is significantly smaller. The qualitative feature of the correlation data seems unchanged. The ridge magnitude is reduced, but seems still present for in-plane trigger particles, decreasing from in-plane to out-

of-plane, and vanishes for out-of-plane trigger particles.

Finally we consider the effect of a v_n that is dependent on the trigger-particle ϕ_s. We analyzed the two-particle cumulants $v_n\{p_T\text{-}p_T\}$ in events with different trigger particle ϕ_s separately. The second harmonic $v_2\{p_T\text{-}p_T\}$ is found to decrease with increasing ϕ_s. This is synonymous to the decreasing ridge magnitude with ϕ_s. The fourth harmonic $v_4\{p_T\text{-}p_T\}$ is found to also depend on ϕ_s, but its effect on dihadron correlation is negligible. The third harmonic $v_3\{p_T\text{-}p_T\}$ is found to be independent of ϕ_s. The dihadron correlations are studied relative to the event plane with the subtraction of the two-particle cumulants, $v_3\{2, \eta_{\rm gap}{=}0.7\}$, $v_4\{2, \eta_{\rm gap}{=}0.7\}$ and the ϕ_s-dependent $v_2\{p_T\text{-}p_T, \eta_{\rm gap}{=}0.7\}(\phi_s)$. With this exploratory subtraction of the v_n values, the ridge is found to be eliminated. However, this result does not enlighten the origin of the ridge because the measured ϕ_s-dependent v_2 has likely already included the ridge; whether the ridge is due to flow or nonflow is undetermined. On the other hand, the away-side double-peak structure for out-of-plane triggers remains robust even with the subtraction of ϕ_s-dependent $v_n\{p_T\text{-}p_T, \eta_{\rm gap}{=}0.7\}$. This indicates medium effect to the away-side jet propagation and the effect depends on the pathlength the away-side jet traverses.

To summarize our main findings, high p_T triggered particles are biased towards surface emission, and the near-side jet fragmentation is hardly modified by the medium. Away-side partner jets interact maximally with the medium in the direction perpendicular to the reaction plane. These interactions may be responsible for the double-peak correlation structure remaining on the away side even after v_3 subtraction. The near-side jet-like component is accompanied by the ridge in the reaction-plane direction. The ridge magnitude drops rapidly with increasing ϕ_s and largely disappears out-of-plane in mid-central 20-60% Au+Au collisions. The most natural explanation for our results seems to be the combination of a near-side in-vacuum jet-fragmentation, a near-side ridge and away-side double-peak structure significantly contributed by triangular flow, and remaining double-peak correlations on the away side for out-of-plane trigger particles.

Appendix A: Effect of Possible Biases in Event-Plane Reconstruction

In our analysis, the event plane is reconstructed by particles excluding those within $|\Delta\eta| < 0.5$ of the trigger particle. Question remains how much is the effect of possible biases to the reconstructed event plane by particles correlated to the trigger, especially on the away side. One way to estimate this possible effect is to analyze dihadron correlations relative to the event plane reconstructed from particles without exluding those within $|\Delta\eta| < 0.5$ of the trigger, thereby maximizing the biases from jet-correlations. These results (subtracted by v_2, $v_4(\psi_2)$, and v_3 backgrounds with resolutions corresponding to the new EP) are shown in the upper panels of Fig. 25. The differences between these results and our default results in Fig. 21 are shown in the lower panels of Fig. 25. By including in EP those particles close to the trigger in η, the correlated yield at $\Delta\phi = 0$ for in-plane triggers is smaller, and for out-of-plane triggers, larger. The correlated yield at $\Delta\phi = 0$ is not larger for in-plane triggers as one would naively expect from a more aligned EP. This is because the associated p_T bin is always excluded from EP reconstruction. We have verified, if the associated p_T bin is included in EP, that the associated yield at $\Delta\phi = 0$ for in-plane triggers is significantly enhanced as expected.

As seen from Fig. 25, introducing a stronger bias in EP reconstruction causes a relatively small change in the correlation signals. This suggests that possible EP biases in our default results in Fig. 21 may be also relatively small.

Appendix B: Implications of Possible ϕ_s-Dependent v_2 on Inclusive Dihadron Correlations

If v_2 depends on ϕ_s, then there is an important implication to the inclusive dihadron correlation (i.e., without cutting on ϕ_s). For inclusive dihadron correlation, a flow background $\langle v_2^{(t)}\{2\}\rangle \cdot \langle v_2^{(a)}\{2\}\rangle$ has been used so far for $\langle v_2^{(t)}\{2\} \cdot v_2^{(a)}\{2\}\rangle$. (Note, for clarity, we have omitted the $\langle ...\rangle$ notation throughout the paper except here.) This is correct because fluctuations are already included in the two-particle cumulant flow measurement of $\langle v_2\{2\}\rangle$. However, if v_2 depends on trigger particle orientation ϕ_s, then the equality $\langle v_2^{(t)}\{2\}(\phi_s) \cdot v_2^{(a)}\{2\}(\phi_s)\rangle = \langle v_2^{(t)}\{2\}(\phi_s)\rangle \cdot \langle v_2^{(a)}\{2\}(\phi_s)\rangle$ is no longer valid. The left side is always larger than the right side. This means that the inclusive dihadron flow background is underestimated by $\langle v_2^{(t)}\{2\}\rangle \cdot \langle v_2^{(a)}\{2\}\rangle$. In fact, because $v_2^{(t)}\{2\}(\phi_s)$ is positive for $\phi_s \sim 0$ and negative for $\phi_s \sim \pi/2$, the true background magnitude for inclusive dihadron correlation is even larger than that for the $\phi_s = 0$ dihadron correlation, which has the largest background magnitude of all ϕ_s bins. Namely, for all ϕ_s,

$$\langle v_2^{(t)}\{2\}(\phi_s) \cdot v_2^{(a)}\{2\}(\phi_s)\rangle > \langle v_2^{(t)}\{2\}(\phi_s)\rangle \cdot \langle v_2^{(a)}\{2\}(\phi_s)\rangle > \langle v_2^{(t)}\{2\}(\phi_s = 0)\rangle \cdot \langle v_2^{(a)}\{2\}(\phi_s = 0)\rangle\,. \quad \text{(B1)}$$

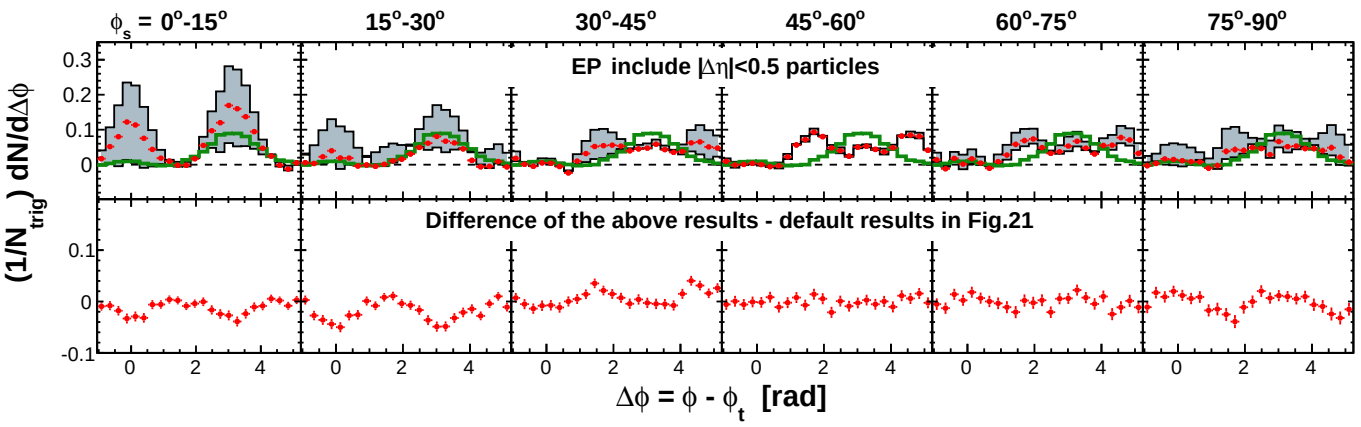

FIG. 25: (Color online) Upper panels: As same as Fig. 21 upper panels but relative to event plane reconstructed without excluding particles within $|\Delta\eta| < 0.5$ of the trigger. The v_2, $v_4(\psi_2)$, and v_3 backgrounds are subtracted with resolutions corresponding to the new EP. Lower panels: the difference between the upper panel results minus the default results in Fig. 21.

Fig. 26 illustrates the effect. The upper panel shows the raw dihadron correlation for $3 < p_T^{(t)} < 4$ GeV/c and $1 < p_T^{(a)} < 1.5$ GeV/c together with two flow background curves both ZYAM-normalized. The blue histogram is from a traditional inclusive dihadron correlation analysis with the v_2 modulation calculated from $\langle v_2^{(t)}\{2\}\rangle \cdot \langle v_2^{(a)}\{2\}\rangle$. The red histogram is that calculated from the ϕ_s-dependent $v_2\{2\}(\phi_s)$ by $\langle v_2^{(t)}\{2\}(\phi_s) \cdot v_2^{(a)}\{2\}(\phi_s)\rangle$ which is the correct flow background provided $v_2(\phi_s)$ is the real flow. (The v_3 and v_4 contributions are included in both flow background histograms). As seen from Fig. 26, the traditional flow background is underestimated. The lower panel of Fig. 26 shows the dihadron correlation signals after subtraction of the traditional background in the histogram and by the correct flow background in the data points, respectively. The signal from the traditional average flow background subtraction is less double-peaked. This means, if the ridge is entirely due to flow that must be ϕ_s-dependent, then all the inclusive dihadron correlation analyses have under-subtracted the flow background, resulting in a more peaked away-side correlation signal.

Appendix C: Dihadron Correlation Functions

This appendix presents dihadron correlation functions. Figures 27, 28, 29, and 30 show the raw correlation functions. Figures 31, 32, 33, and 34 show the v_2, v_4 and ZYAM background-subtracted correlation functions. Figures 35 and 36 show the near-side jet-like correlation functions. Figures 37, 38, 39, and 40 show the v_2, v_3, v_4 and ZYAM background-subtracted correlation functions. The data for the correlation functions and all other figures in the paper are published on-line at http://www.star.bnl.gov/central/publications/.

Acknowledgments

We thank the RHIC Operations Group and RCF at BNL, the NERSC Center at LBNL and the Open Science Grid consortium for providing resources and support. This work was supported in part by the Offices of NP and HEP within the U.S. DOE Office of Science, the U.S. NSF, the Sloan Foundation, the DFG cluster of excellence 'Origin and Structure of the Universe' of Germany, CNRS/IN2P3, STFC and EPSRC of the United Kingdom, FAPESP CNPq of Brazil, Ministry of Ed. and Sci. of the Russian Federation, NNSFC, CAS, MoST, and MoE of China, GA and MSMT of the Czech Republic, FOM and NWO of the Netherlands, DAE, DST, and CSIR of India, Polish Ministry of Sci. and Higher Ed., Korea Research Foundation, Ministry of Sci., Ed. and Sports of the Rep. Of Croatia, Russian Ministry of Sci. and Tech, and RosAtom of Russia.

[1] I. Arsene et al. Quark gluon plasma and color glass condensate at RHIC? The Perspective from the BRAHMS experiment. *Nucl.Phys.*, A757:1–27, 2005.

[2] B.B. Back et al. The PHOBOS perspective on discoveries at RHIC. *Nucl.Phys.*, A757:28–101, 2005.

[3] John Adams et al. Experimental and theoretical challenges in the search for the quark gluon plasma: The STAR Collaboration's critical assessment of the evidence from RHIC collisions. *Nucl.Phys.*, A757:102–183, 2005.

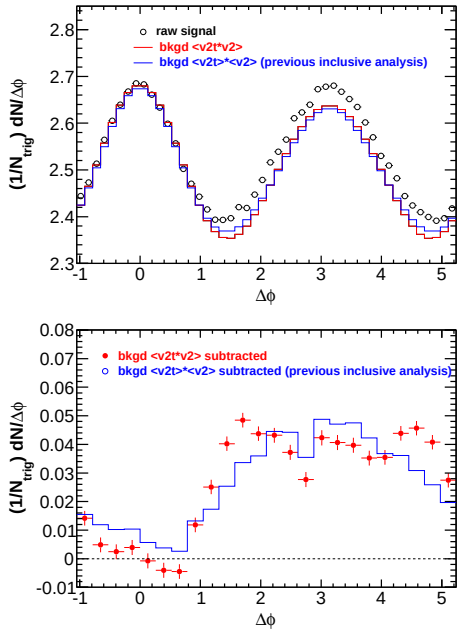

FIG. 26: (Color online) Effect of possible ϕ_s-dependent elliptic flow anisotropy on inclusive dihadron correlations. Upper panel: raw $\Delta\phi$ correlation together with flow background obtained by two different ways, one by the average of the product of the trigger $v_2^{(t,R)}$ and the associated particle $v_2^{(a)}(\phi_s)$ as from this analysis (red histogram), and the other by the product of the average trigger and associated v_2 as from the standard inclusive dihadron correlation analysis (blue histogram). Lower panel: the correlation signals subtracted by the background from this analysis (red points) and by the standard background from inclusive dihadron correlation analysis (blue histogram). The data are from minimum-bias 20-60% Au+Au collisions. The trigger and associated particle p_T ranges are $3 < p_T^{(t)} < 4$ GeV/c and $1 < p_T^{(a)} < 1.5$ GeV/c, respectively. A $|\Delta\eta| > 0.7$ cut is applied to the trigger-associated pairs. Error bars are statistical.

[4] K. Adcox et al. Formation of dense partonic matter in relativistic nucleus-nucleus collisions at RHIC: Experimental evaluation by the PHENIX collaboration. *Nucl.Phys.*, A757:184–283, 2005.

[5] Miklos Gyulassy and Larry McLerran. New forms of QCD matter discovered at RHIC. *Nucl.Phys.*, A750:30–63, 2005.

[6] Peter Jacobs and Xin-Nian Wang. Matter in extremis: Ultrarelativistic nuclear collisions at RHIC. *Prog.Part.Nucl.Phys.*, 54:443–534, 2005.

[7] Hanzhong Zhang, J. F. Owens, Enke Wang, and Xin-Nian Wang. Dihadron tomography of high-energy nuclear collisions in NLO pQCD. *Phys. Rev. Lett.*, 98:212301, 2007.

[8] Fuqiang Wang. Novel Phenomena in Particle Correlations in Relativistic Heavy-Ion Collisions. *Prog. Part. Nucl. Phys.*, 74:35–54, 2014.

[9] C. Adler et al. Disappearance of back-to-back high p_T hadron correlations in central Au+Au collisions at $\sqrt{s_{NN}}$= 200 GeV. *Phys.Rev.Lett.*, 90:082302, 2003.

[10] Miklos Gyulassy and Michael Plumer. JET QUENCHING IN DENSE MATTER. *Phys.Lett.*, B243:432–438, 1990.

[11] Xin-Nian Wang and Miklos Gyulassy. Gluon shadowing and jet quenching in A + A collisions at $\sqrt{s}$ = 200-GeV. *Phys.Rev.Lett.*, 68:1480–1483, 1992.

[12] R. Baier, D. Schiff, and B. G. Zakharov. Energy loss in perturbative QCD. *Ann. Rev. Nucl. Part. Sci.*, 50:37–69, 2000.

[13] J. Adams et al. Distributions of charged hadrons associated with high transverse momentum particles in pp and Au + Au collisions at $\sqrt{s_{NN}}$= 200-GeV. *Phys.Rev.Lett.*, 95:152301, 2005.

[14] B.I. Abelev et al. Long range rapidity correlations and jet production in high energy nuclear collisions. *Phys.Rev.*, C80:064912, 2009.

[15] B.I. Abelev et al. Three-particle coincidence of the long range pseudorapidity correlation in high energy nucleus-nucleus collisions. *Phys.Rev.Lett.*, 105:022301, 2010.

[16] A. Adare et al. Dihadron azimuthal correlations in Au+Au collisions at $\sqrt{s_{NN}}$= 200-GeV. *Phys.Rev.*, C78:014901, 2008.

[17] M.M. Aggarwal et al. Azimuthal di-hadron correlations in d+Au and Au+Au collisions at $\sqrt{s_{NN}}$=200 GeV from STAR. *Phys.Rev.*, C82:024912, 2010.

[18] Ivan Vitev. Large angle hadron correlations from medium-induced gluon radiation. *Phys. Lett.*, B630:78–84, 2005.

[19] Antonio D. Polosa and Carlos A. Salgado. Jet Shapes in Opaque Media. *Phys.Rev.*, C75:041901, 2007.

[20] Horst Stoecker. Collective flow signals the quark gluon plasma. *Nucl.Phys.*, A750:121–147, 2005.

[21] J. Casalderrey-Solana, E.V. Shuryak, and D. Teaney. Conical flow induced by quenched QCD jets. *J.Phys.Conf.Ser.*, 27:22–31, 2005.

[22] Jorg Ruppert and Berndt Muller. Waking the colored plasma. *Phys.Lett.*, B618:123–130, 2005.

[23] Thorsten Renk and Jorg Ruppert. Mach cones in an evolving medium. *Phys. Rev.*, C73:011901, 2006.

[24] Sergei Khlebnikov, Martin Kruczenski, and Georgios Michalogiorgakis. Shock waves in strongly coupled plasmas. *Phys.Rev.*, D82:125003, 2010.

[25] Barbara Betz, Jorge Noronha, Giorgio Torrieri, Miklos Gyulassy, and Dirk H. Rischke. Universal Flow-Driven Conical Emission in Ultrarelativistic Heavy-Ion Collisions. *Phys.Rev.Lett.*, 105:222301, 2010.

[26] R.B. Neufeld and Ivan Vitev. Parton showers as sources of energy-momentum deposition in the QGP and their implication for shockwave formation at RHIC and at the LHC. *Phys.Rev.*, C86:024905, 2012.

[27] Alejandro Ayala, Isabel Dominguez, and Maria Elena Tejeda-Yeomans. Head shock vs Mach cone: azimuthal correlations from 2 to 3 parton processes in relativistic heavy-ion collisions. *Phys.Rev.*, C88:025203, 2013.

[28] I. Bouras, B. Betz, Z. Xu, and C. Greiner. Mach cones in viscous heavy-ion collisions. *Phys. Rev.*, C90(2):024904, 2014.

[29] Yasuki Tachibana and Tetsufumi Hirano. Interplay between Mach cone and radial expansion and its signal in γ-jet events. *Phys. Rev.*, C93(5):054907, 2016.

[30] B. Alver and G. Roland. Collision geometry fluctuations and triangular flow in heavy-ion collisions. *Phys.Rev.*, C81:054905, 2010. Erratum-ibid. **C82**, 039903 (2010).

[31] B.I. Abelev et al. Indications of Conical Emission of Charged Hadrons at RHIC. *Phys.Rev.Lett.*, 102:052302,

2009.

[32] Arthur M. Poskanzer and S.A. Voloshin. Methods for analyzing anisotropic flow in relativistic nuclear collisions. *Phys.Rev.*, C58:1671–1678, 1998.

[33] J. Adams et al. Azimuthal anisotropy and correlations at large transverse momenta in p+p and Au+Au collisions at $\sqrt{s_{NN}}$= 200-GeV. *Phys.Rev.Lett.*, 93:252301, 2004.

[34] Aoqi Feng. Di-hadron Azimuthal Correlations Relative to Reaction Plane in Au + Au Collisions at $\sqrt{s_{NN}}$ = 200 GeV. 2008. Ph.D. thesis, Institute of Particle Physics, CCNU, May 2008.

[35] H. Agakishiev et al. Event-plane-dependent dihadron correlations with harmonic v_n subtraction in Au + Au collisions at $\sqrt{s_{NN}}$ = 200 GeV. *Phys. Rev.*, C89(4):041901, 2014.

[36] A. Adare et al. Measurement of two-particle correlations with respect to second- and third-order event planes in Au+Au collisions at $\sqrt{s_{NN}}$ = 200 GeV. *Phys. Rev.*, C99(5):054903, 2019.

[37] K.H. Ackermann et al. STAR detector overview. *Nucl.Instrum.Meth.*, A499:624–632, 2003.

[38] F.S. Bieser, H.J. Crawford, J. Engelage, G. Eppley, L.C. Greiner, et al. The STAR trigger. *Nucl.Instrum.Meth.*, A499:766–777, 2003.

[39] C. Adler et al. The RHIC zero-degree calorimeters. *Nucl.Instrum.Meth.*, A499:433–436, 2003.

[40] K.H. Ackermann et al. The STAR time projection chamber. *Nucl.Phys.*, A661:681–685, 1999.

[41] M. Anderson et al. The Star time projection chamber: A Unique tool for studying high multiplicity events at RHIC. *Nucl.Instrum.Meth.*, A499:659–678, 2003.

[42] J. Adams et al. Identified particle distributions in pp and Au+Au collisions at $\sqrt{s_{NN}}$= 200 GeV. *Phys. Rev. Lett.*, 92:112301, 2004.

[43] B.I. Abelev et al. Systematic measurements of identified particle spectra in *pp*, *d*+Au and Au+Au collisions from STAR. *Phys.Rev.*, C79:034909, 2009.

[44] B. Alver, B.B. Back, M.D. Baker, M. Ballintijn, D.S. Barton, et al. Importance of correlations and fluctuations on the initial source eccentricity in high-energy nucleus-nucleus collisions. *Phys.Rev.*, C77:014906, 2008.

[45] J. Adams et al. Azimuthal anisotropy in Au+Au collisions at $\sqrt{s_{NN}}$= 200-GeV. *Phys.Rev.*, C72:014904, 2005.

[46] S. Wang, Y. Z. Jiang, Y. M. Liu, D. Keane, D. Beavis, S. Y. Chu, S. Y. Fung, M. Vient, C. Hartnack, and Horst Stoecker. Measurement of collective flow in heavy ion collisions using particle pair correlations. *Phys. Rev.*, C44:1091–1095, 1991.

[47] Michael Daugherity. Anomalous centrality variation of minijet angular correlations in Au-Au collisions at 62-GeV and 200-GeV from STAR. *J. Phys.*, G35:104090, 2008.

[48] G. Agakishiev et al. Anomalous centrality evolution of two-particle angular correlations from Au-Au collisions at $\sqrt{s_{NN}}$= 62 and 200 GeV. *Phys.Rev.*, C86:064902, 2012.

[49] J. Bielcikova, S. Esumi, K. Filimonov, S. Voloshin, and J. P. Wurm. Elliptic flow contribution to two particle correlations at different orientations to the reaction plane. *Phys. Rev.*, C69:021901, 2004.

[50] K. Adcox et al. Centrality dependence of pi+ / pi-, K+ / K-, p and anti-p production from $\sqrt{s_{NN}}$= 13-=GeV Au+Au collisions at RHIC. *Phys. Rev. Lett.*, 88:242301, 2002.

[51] John Adams et al. Measurements of identified particles at intermediate transverse momentum in the STAR experiment from Au + Au collisions at $\sqrt{s_{NN}}$ = 200 GeV. 2006.

[52] Rudolph C. Hwa and C. B. Yang. Scaling distributions of quarks, mesons and proton for all p(T), energy and centrality. *Phys. Rev.*, C67:064902, 2003.

[53] V. Greco, C. M. Ko, and P. Levai. Parton coalescence at RHIC. *Phys. Rev.*, C68:034904, 2003.

[54] R. J. Fries, Berndt Muller, C. Nonaka, and S. A. Bass. Hadron production in heavy ion collisions: Fragmentation and recombination from a dense parton phase. *Phys. Rev.*, C68:044902, 2003.

[55] Christine E. Nattrass. System size dependence of strange particle correlations in Cu + Cu and Au + Au collisions at $\sqrt{s_{NN}}$= 200-GeV in STAR at RHIC. *J. Phys.*, G35:044063, 2008.

[56] R. J. Fries, S. A. Bass, and Berndt Muller. Correlated emission of hadrons from recombination of correlated partons. *Phys. Rev. Lett.*, 94:122301, 2005.

[57] Jason G. Ulery and Fuqiang Wang. Analysis method for jet-like three-particle azimuthal correlations. *Nucl. Instrum. Meth.*, A595:502–511, 2008.

[58] B. I. Abelev et al. System-size independence of directed flow at the Relativistic Heavy-Ion Collider. *Phys. Rev. Lett.*, 101:252301, 2008.

[59] B.I. Abelev et al. Azimuthal Charged-Particle Correlations and Possible Local Strong Parity Violation. *Phys.Rev.Lett.*, 103:251601, 2009.

[60] B.I. Abelev et al. Observation of charge-dependent azimuthal correlations and possible local strong parity violation in heavy ion collisions. *Phys.Rev.*, C81:054908, 2010.

[61] Derek Teaney and Li Yan. Triangularity and Dipole Asymmetry in Heavy Ion Collisions. *Phys.Rev.*, C83:064904, 2011.

[62] Jiangyong Jia, Sooraj K. Radhakrishnan, and Soumya Mohapatra. A study of the anisotropy associated with dipole asymmetry in heavy ion collisions. *J. Phys.*, G40:105108, 2013.

[63] Nicolas Borghini, Phuong Mai Dinh, and Jean-Yves Ollitrault. Are flow measurements at SPS reliable? *Phys.Rev.*, C62:034902, 2000.

[64] Paul Sorensen. Implications of space-momentum correlations and geometric fluctuations in heavy-ion collisions. *J.Phys.*, G37:094011, 2010.

[65] Hannah Petersen, Guang-You Qin, Steffen A. Bass, and Berndt Muller. Triangular flow in event-by-event ideal hydrodynamics in Au+Au collisions at $\sqrt{s_{NN}}$=200 GeV. *Phys.Rev.*, C82:041901, 2010.

[66] Michael L. Miller, Klaus Reygers, Stephen J. Sanders, and Peter Steinberg. Glauber modeling in high energy nuclear collisions. *Ann.Rev.Nucl.Part.Sci.*, 57:205–243, 2007.

[67] Jun Xu and Che Ming Ko. The effect of triangular flow on di-hadron azimuthal correlations in relativistic heavy ion collisions. *Phys.Rev.*, C83:021903, 2011.

[68] Jun Xu and Che Ming Ko. Triangular flow in heavy ion collisions in a multiphase transport model. *Phys.Rev.*, C84:014903, 2011.

[69] Bjorn Schenke, Sangyong Jeon, and Charles Gale. Elliptic and triangular flow in event-by-event (3+1)D viscous

hydrodynamics. *Phys. Rev. Lett.*, 106:042301, 2011.

[70] Zhi Qiu and Ulrich W. Heinz. Event-by-event shape and flow fluctuations of relativistic heavy-ion collision fireballs. *Phys.Rev.*, C84:024911, 2011.

[71] Bjorn Schenke, Sangyong Jeon, and Charles Gale. Higher flow harmonics from (3+1)D event-by-event viscous hydrodynamics. *Phys.Rev.*, C85:024901, 2012.

[72] Huichao Song, Steffen A. Bass, Ulrich Heinz, Tetsufumi Hirano, and Chun Shen. 200 A GeV Au+Au collisions serve a nearly perfect quark-gluon liquid. *Phys. Rev. Lett.*, 106:192301, 2011. [Erratum: Phys. Rev. Lett.109,139904(2012)].

[73] Bjoern Schenke, Prithwish Tribedy, and Raju Venugopalan. Fluctuating Glasma initial conditions and flow in heavy ion collisions. *Phys.Rev.Lett.*, 108:252301, 2012.

[74] Paul Romatschke and Ulrike Romatschke. Viscosity Information from Relativistic Nuclear Collisions: How Perfect is the Fluid Observed at RHIC? *Phys.Rev.Lett.*, 99:172301, 2007.

[75] Roy A. Lacey, Rui Wei, N. N. Ajitanand, J. M. Alexander, J. Jia, and A. Taranenko. Glauber-based evaluations of the odd moments of the initial eccentricity relative to the even order participant planes. *Phys. Rev.*, C84:027901, 2011.

[76] D. Teaney and L. Yan. Event-plane correlations and hydrodynamic simulations of heavy ion collisions. *Phys.Rev.*, C90(2):024902, 2014.

[77] Burak Han Alver, Clement Gombeaud, Matthew Luzum, and Jean-Yves Ollitrault. Triangular flow in hydrodynamics and transport theory. *Phys.Rev.*, C82:034913, 2010.

[78] Charles Gale, Sangyong Jeon, Bjorn Schenke, Prithwish Tribedy, and Raju Venugopalan. Event-by-event anisotropic flow in heavy-ion collisions from combined Yang-Mills and viscous fluid dynamics. *Phys.Rev.Lett.*, 110:012302, 2013.

[79] B.I. Abelev et al. Charge Independent(CI) and Charge Dependent(CD) correlations as a function of Centrality formed from Delta phi imum Delta eta Charged Pair Correlations in Minimum Bias Au+Au Collisions at $\sqrt{s_{NN}}$= 200-GeV. 2008.

[80] A. Adare et al. Measurements of Higher-Order Flow Harmonics in Au+Au Collisions at $\sqrt{s_{NN}}$= 200 GeV. *Phys.Rev.Lett.*, 107:252301, 2011.

[81] L. Adamczyk et al. Third Harmonic Flow of Charged Particles in Au+Au Collisions at $\sqrt{s_{NN}}$ = 200 GeV. *Phys. Rev. C 88,*, 014904, 2013.

[82] Ulrich Heinz and Raimond Snellings. Collective flow and viscosity in relativistic heavy-ion collisions. *Ann.Rev.Nucl.Part.Sci.*, 63:123–151, 2013.

[83] J. Adams et al. Azimuthal anisotropy at RHIC: The First and fourth harmonics. *Phys.Rev.Lett.*, 92:062301, 2004.

[84] N.N. Ajitanand et al. Decomposition of harmonic and jet contributions to particle-pair correlations at ultra-relativistic energies. *Phys.Rev.*, C72:011902, 2005.

[85] Natasha Sharma, Joel Mazer, Meghan Stuart, and Christine Nattrass. Background subtraction methods for precision measurements of di-hadron and jet-hadron correlations in heavy ion collisions. *Phys. Rev.*, C93(4):044915, 2016.

[86] Quan Wang and Fuqiang Wang. Identification of flow background to subtract in jet-like azimuthal correlations. *Phys.Rev.*, C81:014907, 2010.

[87] Quan Wang and Fuqiang Wang. Non-flow correlations in a cluster model. *Phys.Rev.*, C81:064905, 2010.

[88] C. Adler et al. Elliptic flow from two and four particle correlations in Au+Au collisions at $\sqrt{s_{NN}}$= 130-GeV. *Phys.Rev.*, C66:034904, 2002.

[89] David Kettler. Universal centrality and collision energy trends for v(2) measurements from 2D angular correlations. *Eur.Phys.J.*, C62:175–181, 2009.

[90] N. M. Abdelwahab et al. Isolation of flow and nonflow correlations by two- and four-particle cumulant measurements of azimuthal harmonics in $\sqrt{s_{\rm NN}}$ = 200 GeV Au+Au collisions. *Phys. Lett.*, B745:40–47, 2015.

[91] Lingshan Xu, Li Yi, Daniel Kikola, Joshua Konzer, Fuqiang Wang, et al. Model-independent decomposition of flow and nonflow in relativistic heavy-ion collisions. *Phys.Rev.*, C86:024910, 2012.

[92] Fuqiang Wang. Jet Quenching and Correlations. *Pramana*, 84(5):801–819, 2015.

[93] B. I. Abelev et al. Centrality dependence of charged hadron and strange hadron elliptic flow from $\sqrt{s_{NN}}$= 200-GeV Au + Au collisions. *Phys. Rev.*, C77:054901, 2008.

[94] Joshua Konzer and Fuqiang Wang. Anisotropic flow background to jet-correlation relative to reaction plane. *Nucl. Instrum. Meth.*, A606:713–716, 2009.

[95] Joshua Robert Konzer. Is the ridge formed by aligned jet propagation and medium flow? *Nucl.Phys.*, A830:621C–622C, 2009.

[96] John Adams et al. Minijet deformation and charge-independent angular correlations on momentum subspace (eta, phi) in Au-Au collisions at $\sqrt{s_{NN}}$= 130-GeV. *Phys.Rev.*, C73:064907, 2006.

[97] B.B. Back et al. Energy dependence of elliptic flow over a large pseudorapidity range in Au+Au collisions at RHIC. *Phys.Rev.Lett.*, 94:122303, 2005.

[98] B.B. Back et al. Centrality and pseudorapidity dependence of elliptic flow for charged hadrons in Au+Au collisions at $\sqrt{s_{NN}}$= 200-GeV. *Phys.Rev.*, C72:051901, 2005.

[99] Charles B. Chiu and Rudolph C. Hwa. Dependence of Ridge Formation on Trigger Azimuth: Correlated Emission Model. *Phys.Rev.*, C79:034901, 2009.

[100] Sergei A. Voloshin. Transverse radial expansion in nuclear collisions and two particle correlations. *Phys. Lett.*, B632:490–494, 2006.

[101] E. V. Shuryak. On the origin of the 'Ridge' phenomenon induced by jets in heavy ion collisions. *Phys. Rev.*, C76:047901, 2007.

[102] Adrian Dumitru, Francois Gelis, Larry McLerran, and Raju Venugopalan. Glasma flux tubes and the near side ridge phenomenon at RHIC. *Nucl.Phys.*, A810:91–108, 2008.

[103] Kevin Dusling, Daniel Fernandez-Fraile, and Raju Venugopalan. Three-particle correlation from glasma flux tubes. *Nucl. Phys.*, A828:161–177, 2009.

[104] Sean Gavin, Larry McLerran, and George Moschelli. Long Range Correlations and the Soft Ridge in Relativistic Nuclear Collisions. *Phys.Rev.*, C79:051902, 2009.

[105] J. Takahashi, B.M. Tavares, W.L. Qian, R. Andrade, F. Grassi, et al. Topology studies of hydrodynamics using two particle correlation analysis. *Phys.Rev.Lett.*, 103:242301, 2009.

[106] Nicolas Borghini. Momentum conservation and correlation analyses in heavy-ion collisions at ultrarelativistic energies. *Phys. Rev.*, C75:021904, 2007.

[107] Nestor Armesto, Carlos A. Salgado, and Urs Achim Wiedemann. Measuring the collective flow with jets. *Phys.Rev.Lett.*, 93:242301, 2004.

[108] Charles B. Chiu and Rudolph C. Hwa. Away-side azimuthal distribution in a Markovian parton scattering model. *Phys.Rev.*, C74:064909, 2006.

[109] Yogiro Hama, Rone Peterson G. Andrade, Frederique Grassi, and Wei-Liang Qian. Trying to understand the ridge effect in hydrodynamic model. *Nonlin.Phenom.Complex Syst.*, 12:466–470, 2009.

[110] R. Andrade, F. Grassi, Yogiro Hama, and W.-L. Qian. A Closer look at the influence of tubular initial conditions on two-particle correlations. *J.Phys.*, G37:094043, 2010.

[111] Guang-You Qin, Hannah Petersen, Steffen A. Bass, and Berndt Muller. Translation of collision geometry fluctuations into momentum anisotropies in relativistic heavy-ion collisions. *Phys.Rev.*, C82:064903, 2010.

[112] Wei-Liang Qian, Rone Andrade, Fernando Gardim, Frédérique Grassi, and Yogiro Hama. Origin of trigger-angle dependence of di-hadron correlations. *Phys. Rev.*, C87(1):014904, 2013.

[113] Dan Wen, Wagner M. Castilho, Kai Lin, Wei-Liang Qian, Yogiro Hama, and Takeshi Kodama. On the peripheral-tube description of the two-particle correlations in nuclear collisions. *J. Phys.*, G46(3):035103, 2019.

[114] Roy A. Lacey, Rui Wei, N.N. Ajitanand, and A. Taranenko. Initial eccentricity fluctuations and their relation to higher-order flow harmonics. *Phys.Rev.*, C83:044902, 2011.

[115] Wei-Liang Qian, Philipe Mota, Rone Andrade, Fernando Gardim, Frédérique Grassi, et al. Decomposition of fluctuating initial conditions and flow harmonics. *J.Phys.*, G41:015103, 2013.

[116] K. Werner, Iu. Karpenko, T. Pierog, M. Bleicher, and K. Mikhailov. Event-by-Event Simulation of the Three-Dimensional Hydrodynamic Evolution from Flux Tube Initial Conditions in Ultrarelativistic Heavy Ion Collisions. *Phys.Rev.*, C82:044904, 2010.

[117] R.P.G. Andrade, F. Grassi, Yogiro Hama, and W.-L. Qian. Hydrodynamics: Fluctuating Initial Conditions and Two-particle Correlations. *Nucl.Phys.*, A854:81–88, 2011.

[118] Fernando G. Gardim, Frederique Grassi, Matthew Luzum, and Jean-Yves Ollitrault. Mapping the hydrodynamic response to the initial geometry in heavy-ion collisions. *Phys. Rev.*, C85:024908, 2012.

[119] Zhi Qiu, Chun Shen, and Ulrich Heinz. Hydrodynamic elliptic and triangular flow in Pb-Pb collisions at $\sqrt{s_{NN}}$=2.76 TeV. *Phys.Lett.*, B707:151–155, 2012.

[120] Fernando G. Gardim, Frederique Grassi, Matthew Luzum, and Jean-Yves Ollitrault. Anisotropic flow in event-by-event ideal hydrodynamic simulations of $\sqrt{s_{NN}}$=200 GeV Au+Au collisions. *Phys.Rev.Lett.*, 109:202302, 2012.

[121] Charles Gale, Sangyong Jeon, and Bjoern Schenke. Hydrodynamic Modeling of Heavy-Ion Collisions. *Int.J.Mod.Phys.*, A28:1340011, 2013.

[122] A. Adare et al. Measurement of the higher-order anisotropic flow coefficients for identified hadrons in Au+Au collisions at $\sqrt{s_{NN}}$ = 200 GeV. *Phys. Rev.*, C93(5):051902, 2016.

[123] A. Adare et al. Measurements of directed, elliptic, and triangular flow in Cu+Au collisions at $\sqrt{s_{NN}}$ = 200 GeV. *Phys. Rev.*, C94(5):054910, 2016.

[124] L. Adamczyk et al. Beam Energy Dependence of the Third Harmonic of Azimuthal Correlations in Au+Au Collisions at RHIC. *Phys. Rev. Lett.*, 116(11):112302, 2016.

[125] Leszek Adamczyk et al. Azimuthal anisotropy in Cu+Au collisions at $\sqrt{s_{NN}}$ = 200 GeV. *Phys. Rev.*, C98(1):014915, 2018.

[126] Matthew Luzum. Collective flow and long-range correlations in relativistic heavy ion collisions. *Phys.Lett.*, B696:499–504, 2011.

[127] Yadav Pandit. Dipole asymmetry at $\sqrt{s_{NN}}$ = 200 GeV Au+Au Collisions from STAR experiment at RHIC. *J. Phys. Conf. Ser.*, 446:012012, 2013.

[128] J. Adam et al. Beam energy dependence of rapidity-even dipolar flow in Au+Au collisions. *Phys. Lett.*, B784:26–32, 2018.

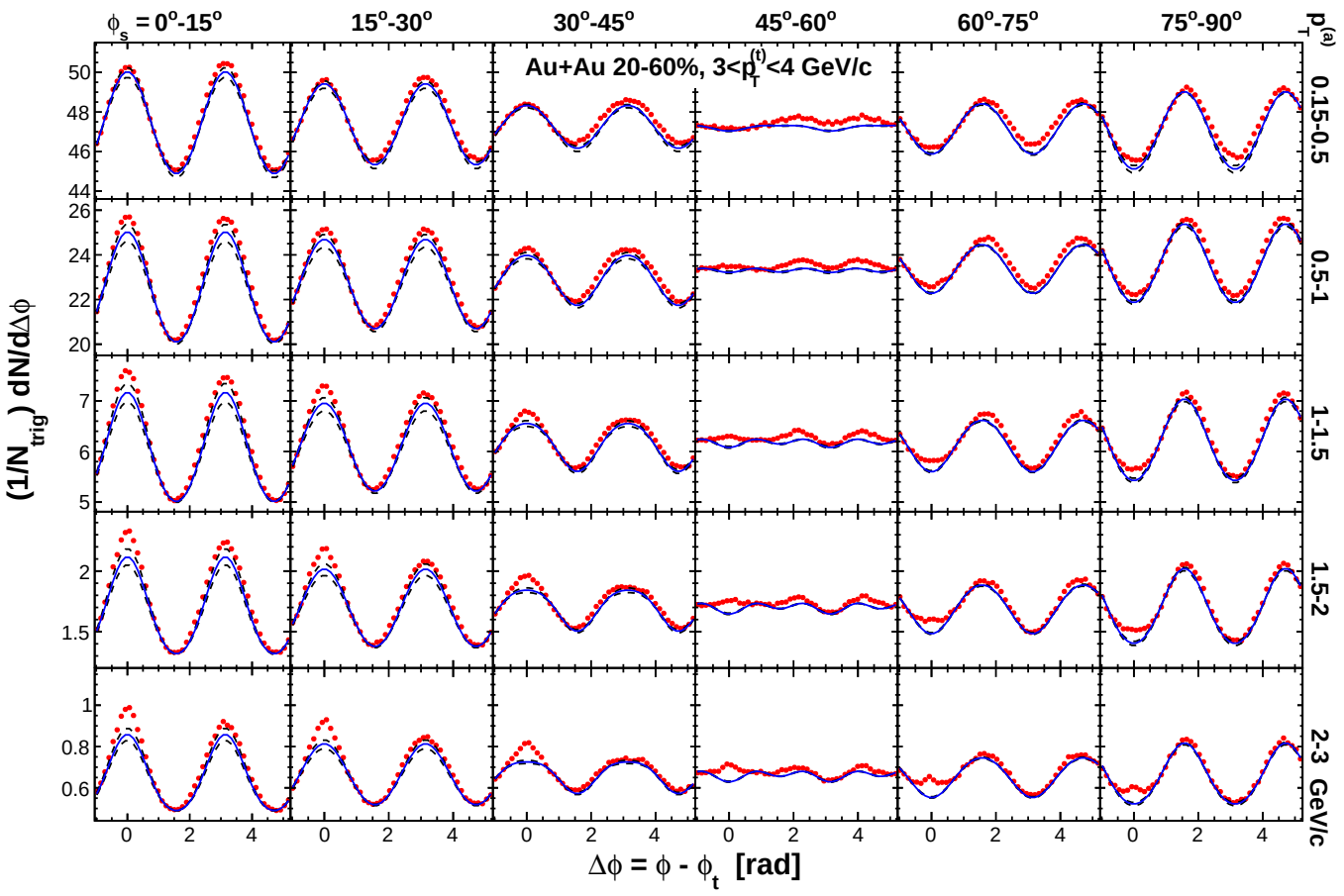

FIG. 27: (Color online) Raw dihadron $\Delta\phi$ correlations with trigger particles in six slices of azimuthal angle relative to the event plane, $\phi_s = |\phi_t - \psi_{\rm EP}|$. The data are from minimum-bias 20-60% Au+Au collisions. The trigger p_T range is $3 < p_T^{(t)} < 4$ GeV/c. Five associated particle $p_T^{(a)}$ bins are shown. Both the trigger and associated particles are restricted within $|\eta| < 1$. The triangle two-particle $\Delta\eta$ acceptance is not corrected. Statistical errors are smaller than the symbol size. The curves are flow modulated ZYAM background including v_2 and $v_4\{\psi_2\}$ by Eq. (1). The used v_2 values are given in Table I from four-particle $v_2\{4\}$ and two-particle $v_2\{2, \eta_{\rm gap}{=}0.7\}$ (dashed curves) and the average v_2 from the two methods (solid curve). The $v_4\{\psi_2\}$ is taken from the parameterization in Eq. (15).

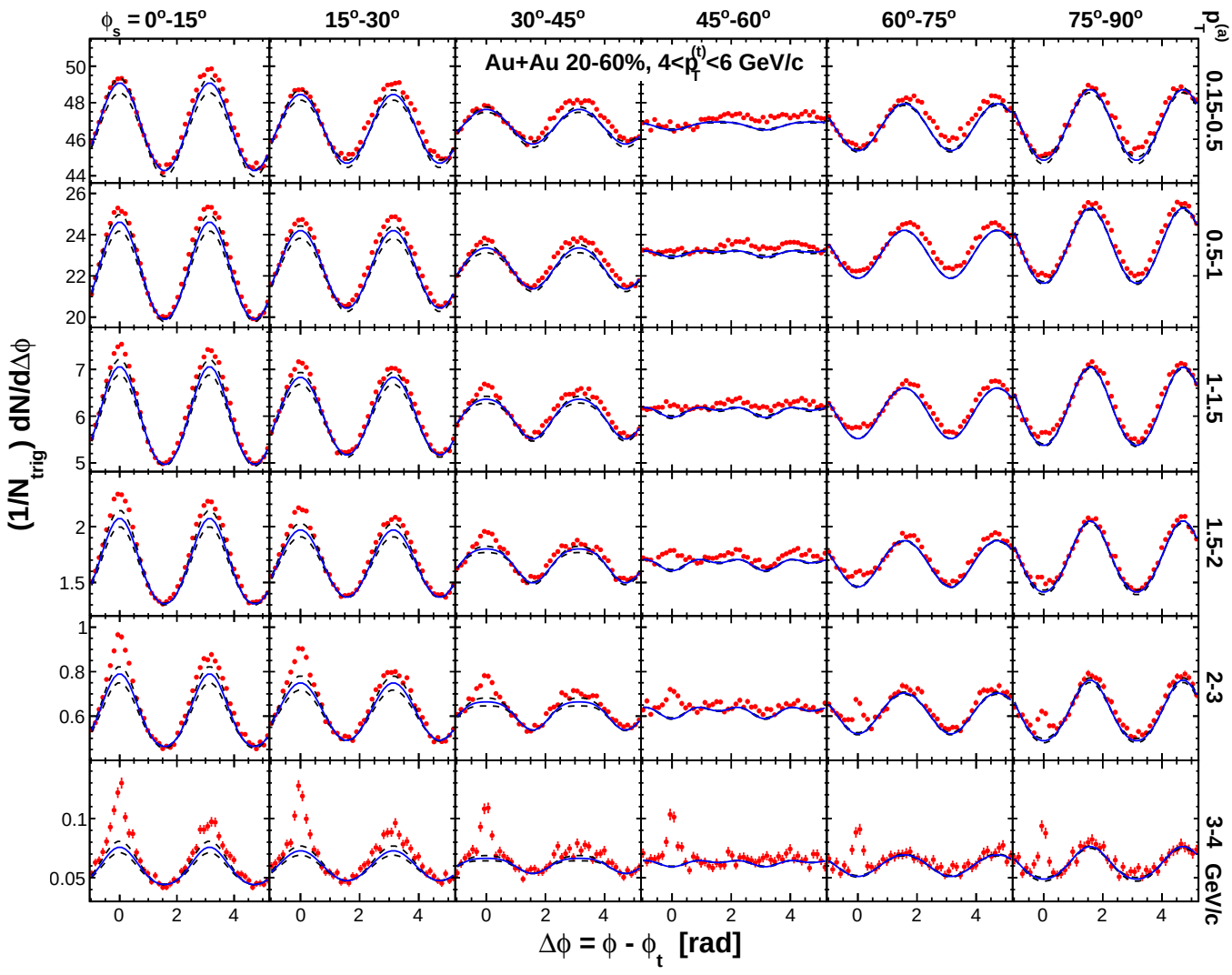

FIG. 28: (Color online) Same as in Fig. 27 but for trigger particle $4 < p_T^{(t)} < 6$ GeV/c and six bins in associated particle $p_T^{(a)}$.

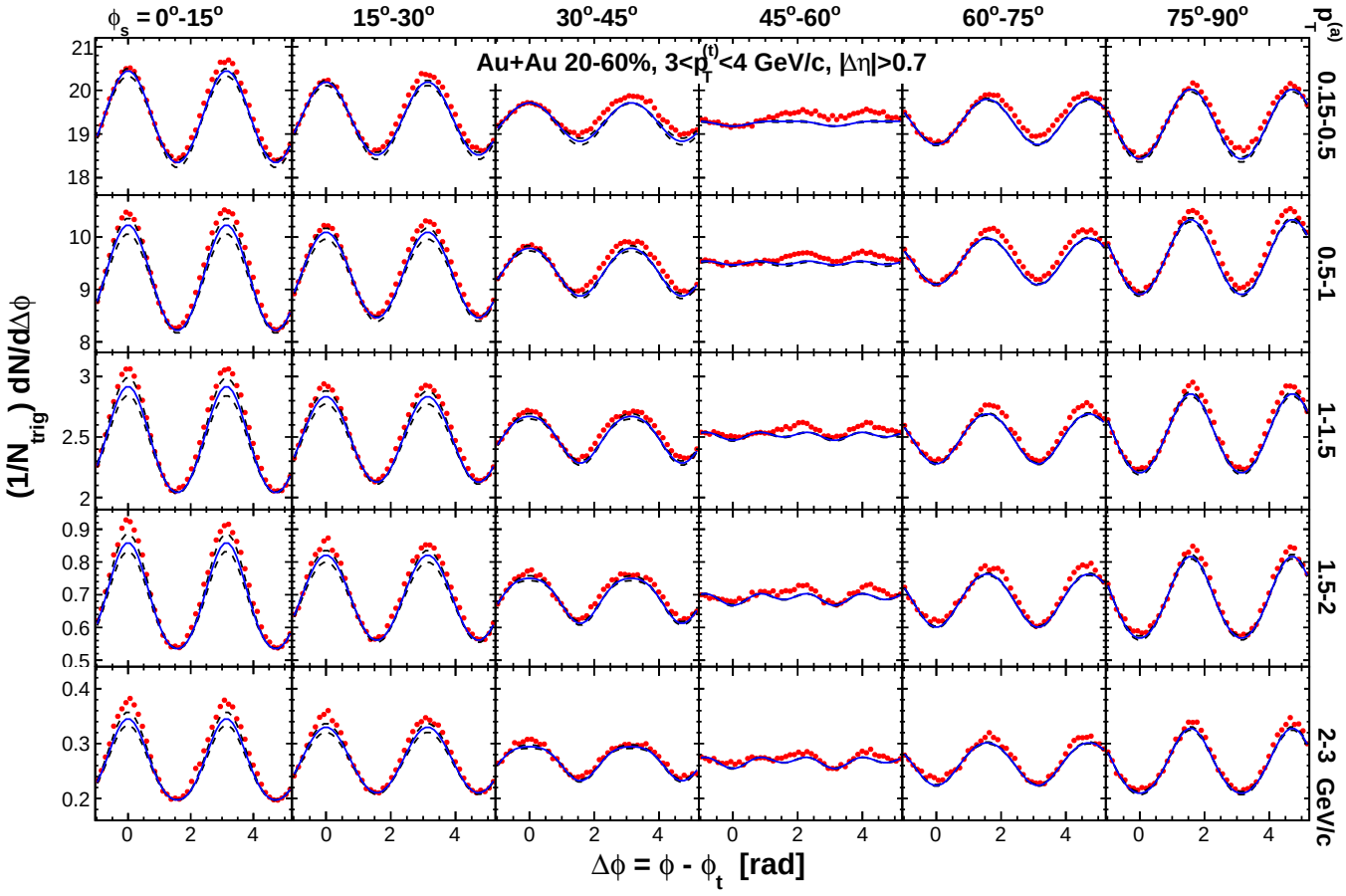

FIG. 29: (Color online) Same as in Fig. 27 but for $|\Delta\eta| > 0.7$.

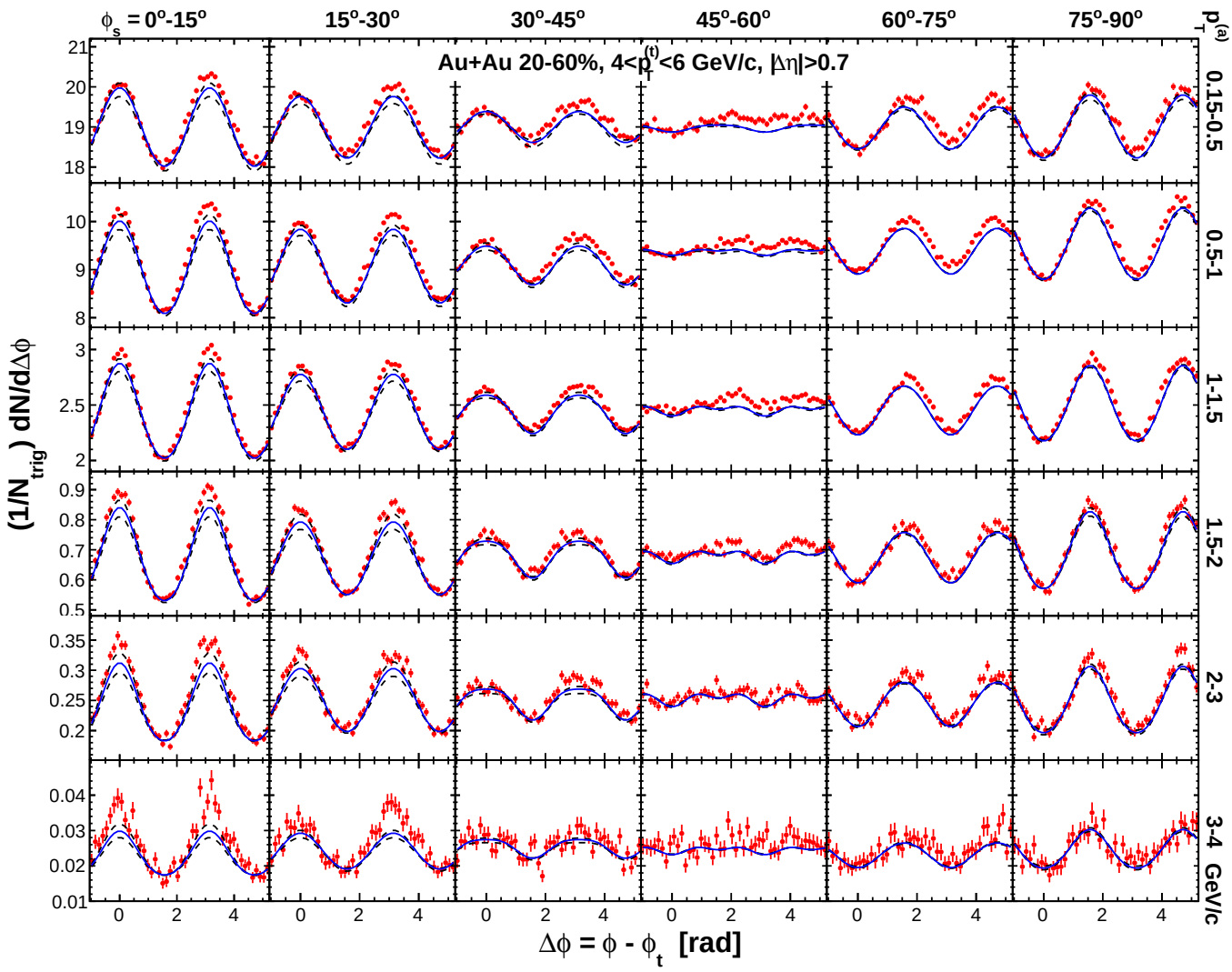

FIG. 30: (Color online) Same as in Fig. 28 but for $|\Delta\eta| > 0.7$.

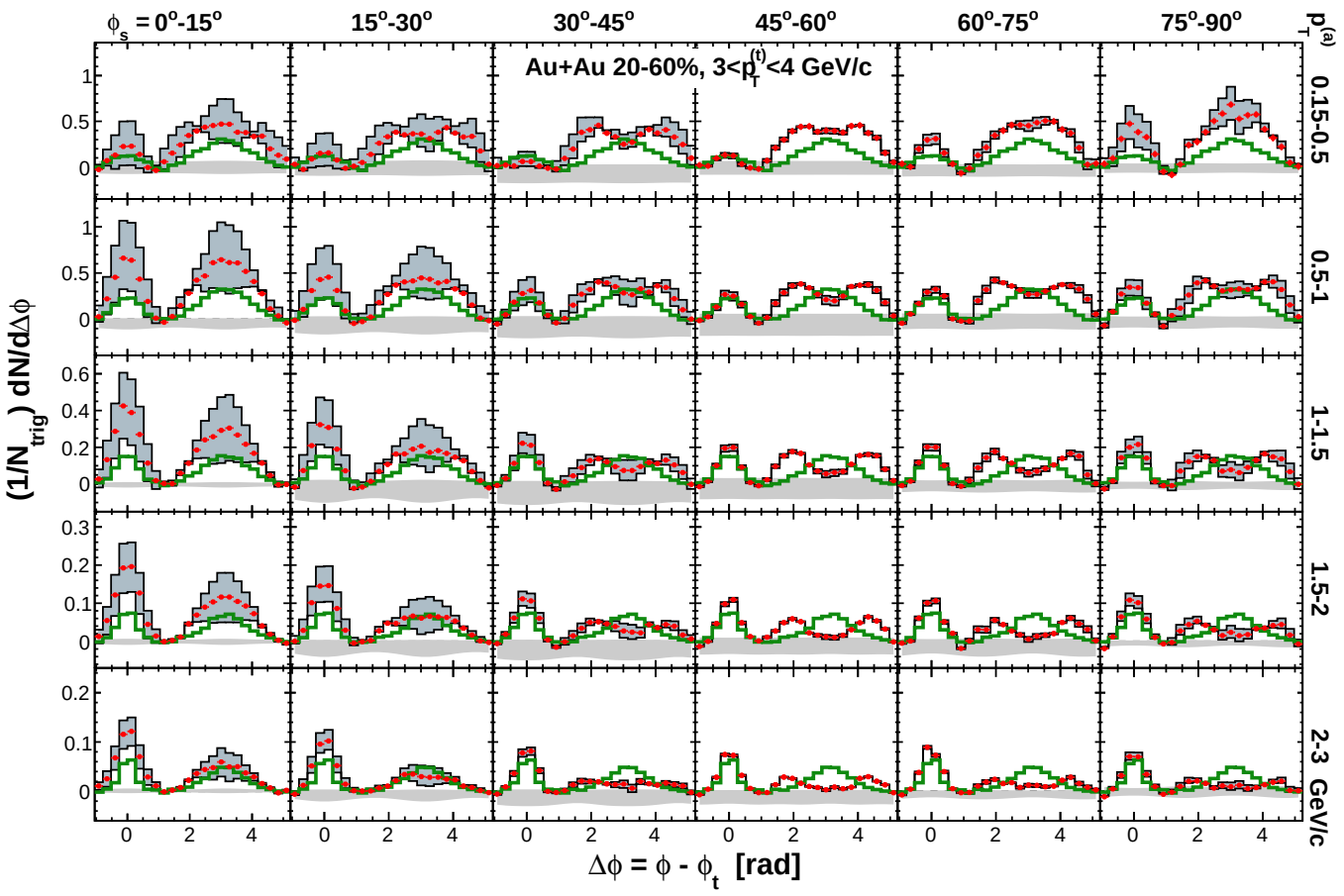

FIG. 31: (Color online) Background-subtracted dihadron correlations with trigger particle in six slices of azimuthal angle relative to the event plane, $\phi_s = |\phi_t - \psi_{\rm EP}|$. The trigger p_T range is $3 < p_T^{(t)} < 4$ GeV/c. Five associated particle $p_T^{(a)}$ bins are shown. Both the trigger and associated particles are restricted to be within $|\eta| < 1$. The triangle two-particle $\Delta\eta$ acceptance is not corrected. The figure corresponds to the raw correlations in Fig. 27. The data points are from minimum-bias 20-60% Au+Au collisions. Flow background is subtracted by Eq. (1) using measurements in Table I and the parameterization in Eq. (15). Systematic uncertainties are shown in the thin histograms embracing the shaded area due to flow subtraction and in the horizontal shaded band around zero due to ZYAM background normalization. Statistical errors are mostly smaller than symbol size. For comparison, the inclusive dihadron correlations from d+Au collisions are superimposed as the thick (green) histograms (only statistical errors are depicted).

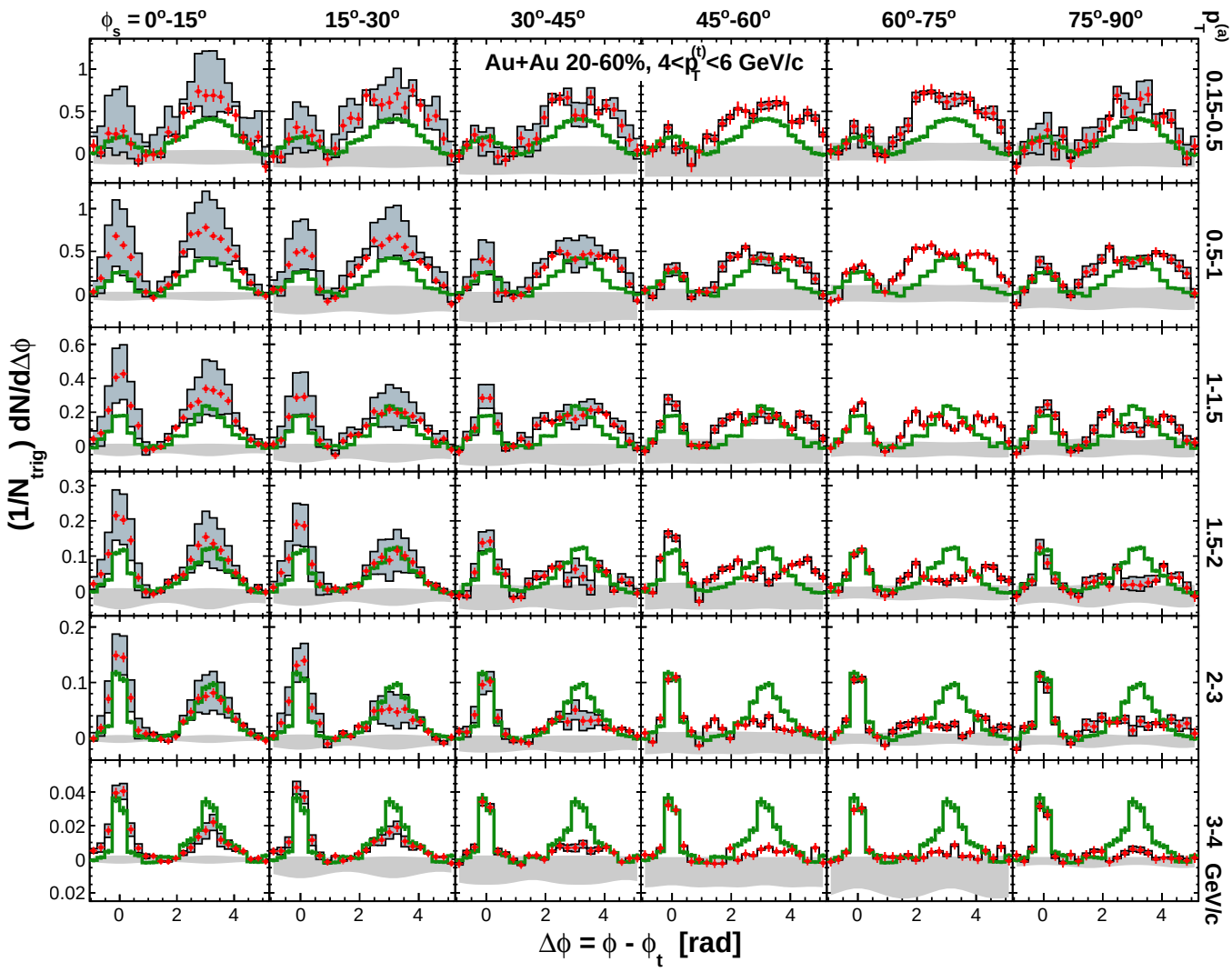

FIG. 32: (Color online) Same as in Fig. 31 but for trigger particle $4 < p_T^{(t)} < 6$ GeV/c and six bins in associated particle $p_T^{(a)}$. The figure corresponds to raw correlations in Fig. 28.

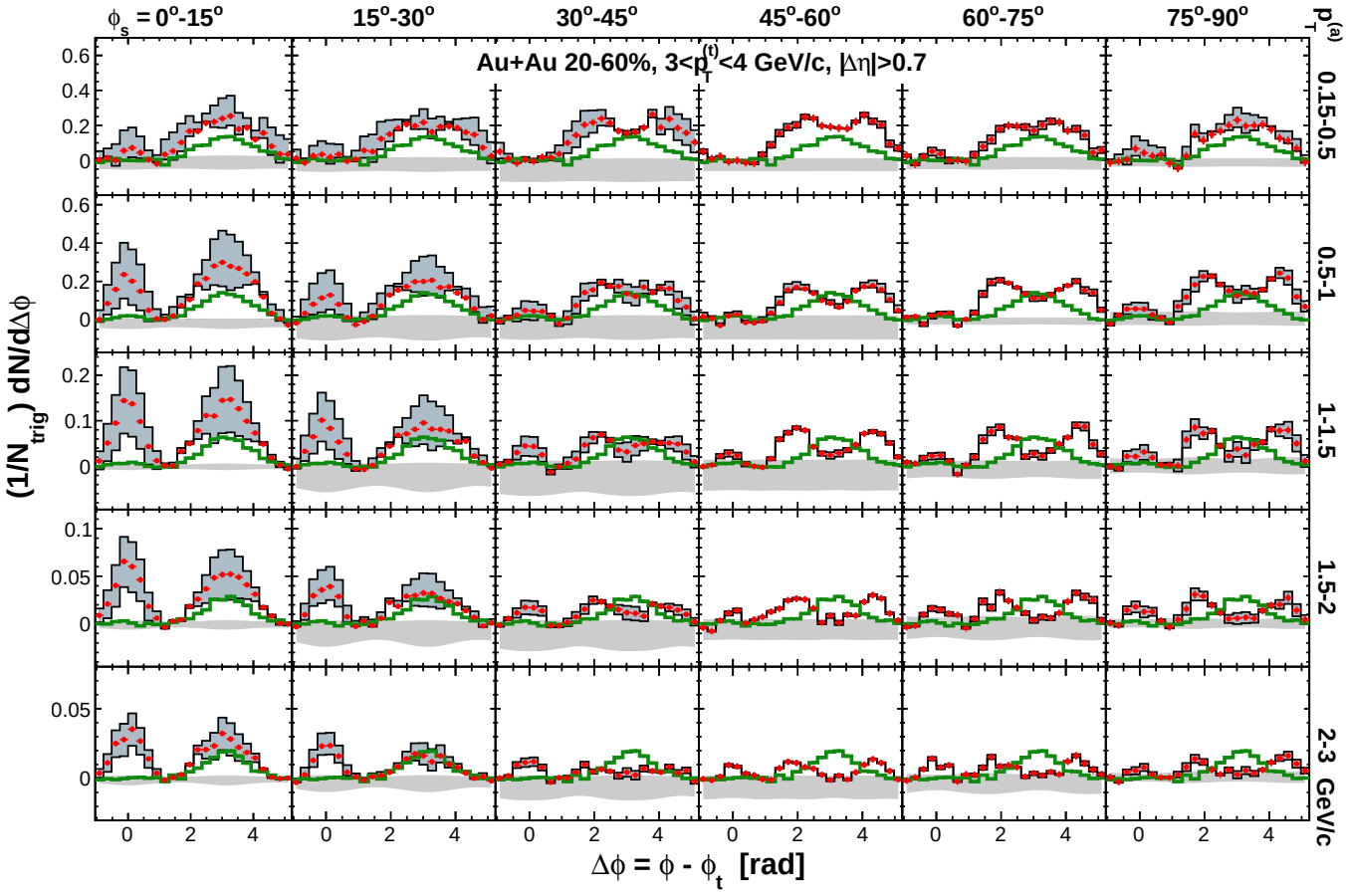

FIG. 33: (Color online) Same as in Fig. 31 but for $|\Delta\eta| > 0.7$. The figure corresponds to raw correlations in Fig. 29.

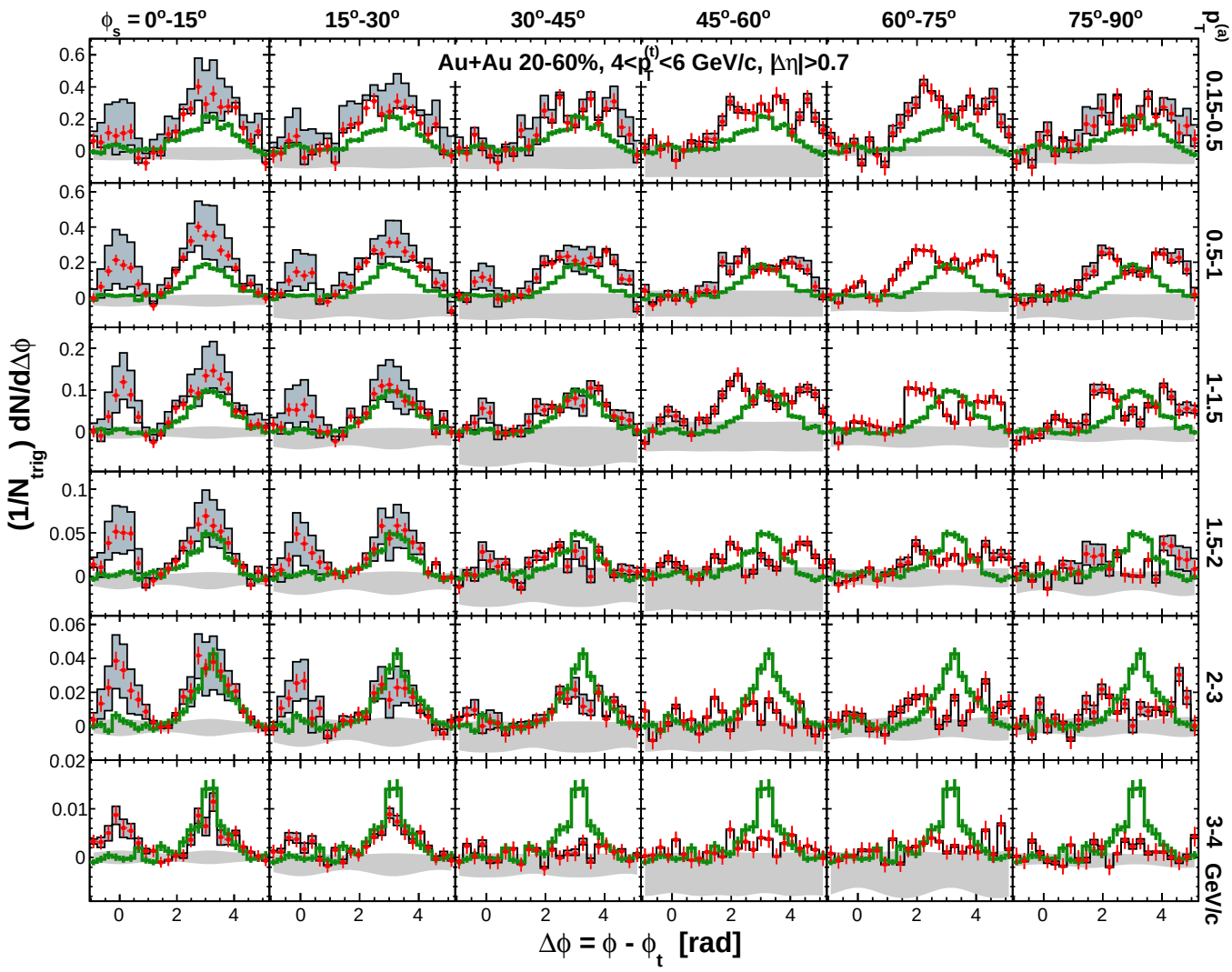

FIG. 34: (Color online) Same as in Fig. 32 but for $|\Delta\eta| > 0.7$. The figure corresponds to raw correlations in Fig. 30.

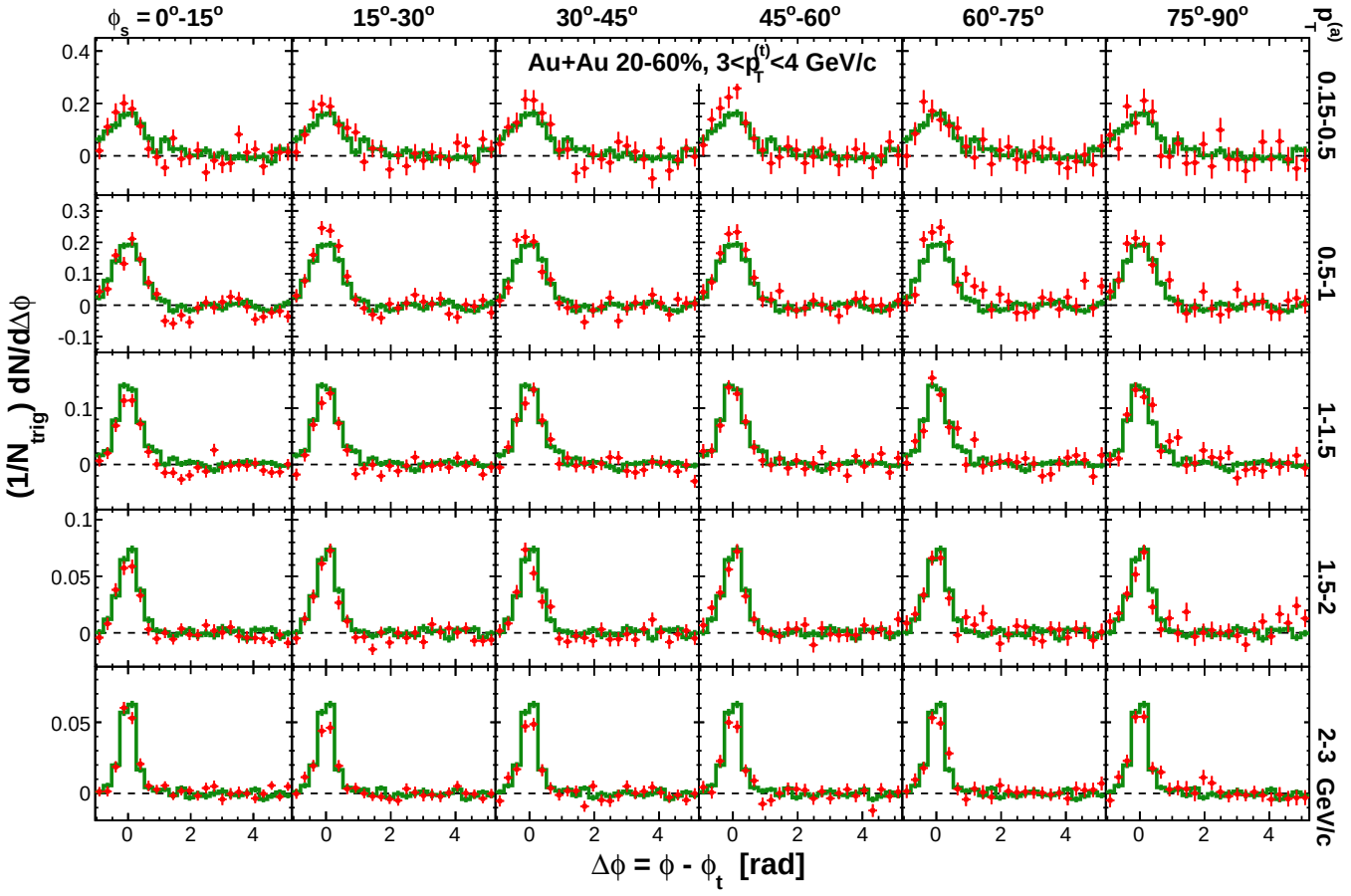

FIG. 35: (Color online) Jet-like dihadron correlations with trigger particle in six slices of azimuth relative to the event plane, $\phi_s = |\phi_t - \psi_{\rm EP}|$. The jet-like dihadron correlations are obtained from the difference between $|\Delta\eta| < 0.7$ and (acceptance weighted) $|\Delta\eta| > 0.7$ correlations. The triangle two-particle $\Delta\eta$ acceptance is not corrected. The trigger p_T range is $3 < p_T^{(t)} < 4$ GeV/c. Five associated particle $p_T^{(a)}$ bins are shown. Both the trigger and associated particles are restricted to be within $|\eta| < 1$. The data points are from minimum-bias 20-60% Au+Au collisions. Superimposed for comparison in the thick histograms are the inclusive jet-like dihadron correlation from d+Au collisions. Errors bars are statistical; Systematic uncertainties are small.

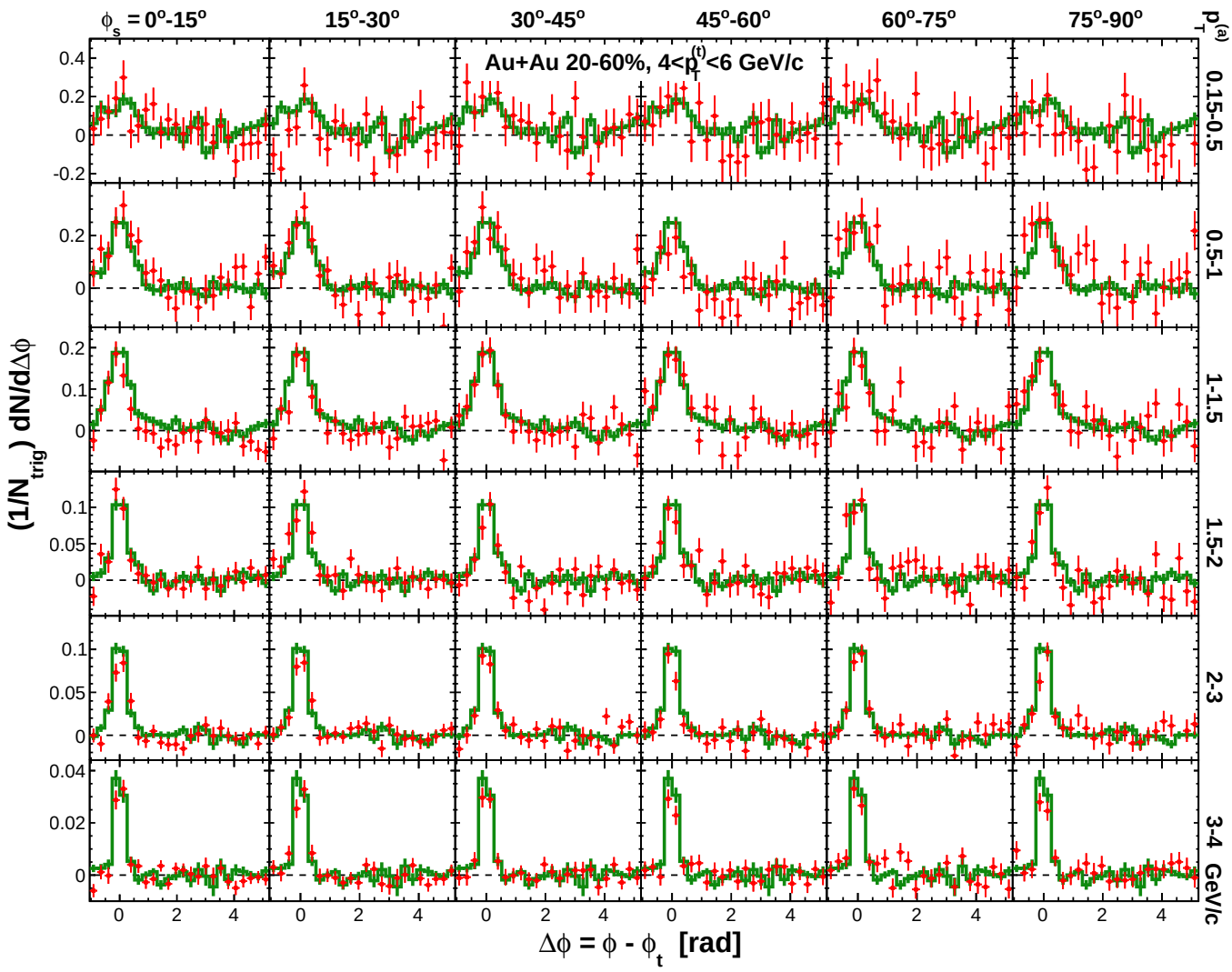

FIG. 36: (Color online) Same as in Fig. 35 but for trigger particle $4 < p_T^{(t)} < 6$ GeV/c and six bins in associated particle $p_T^{(a)}$.

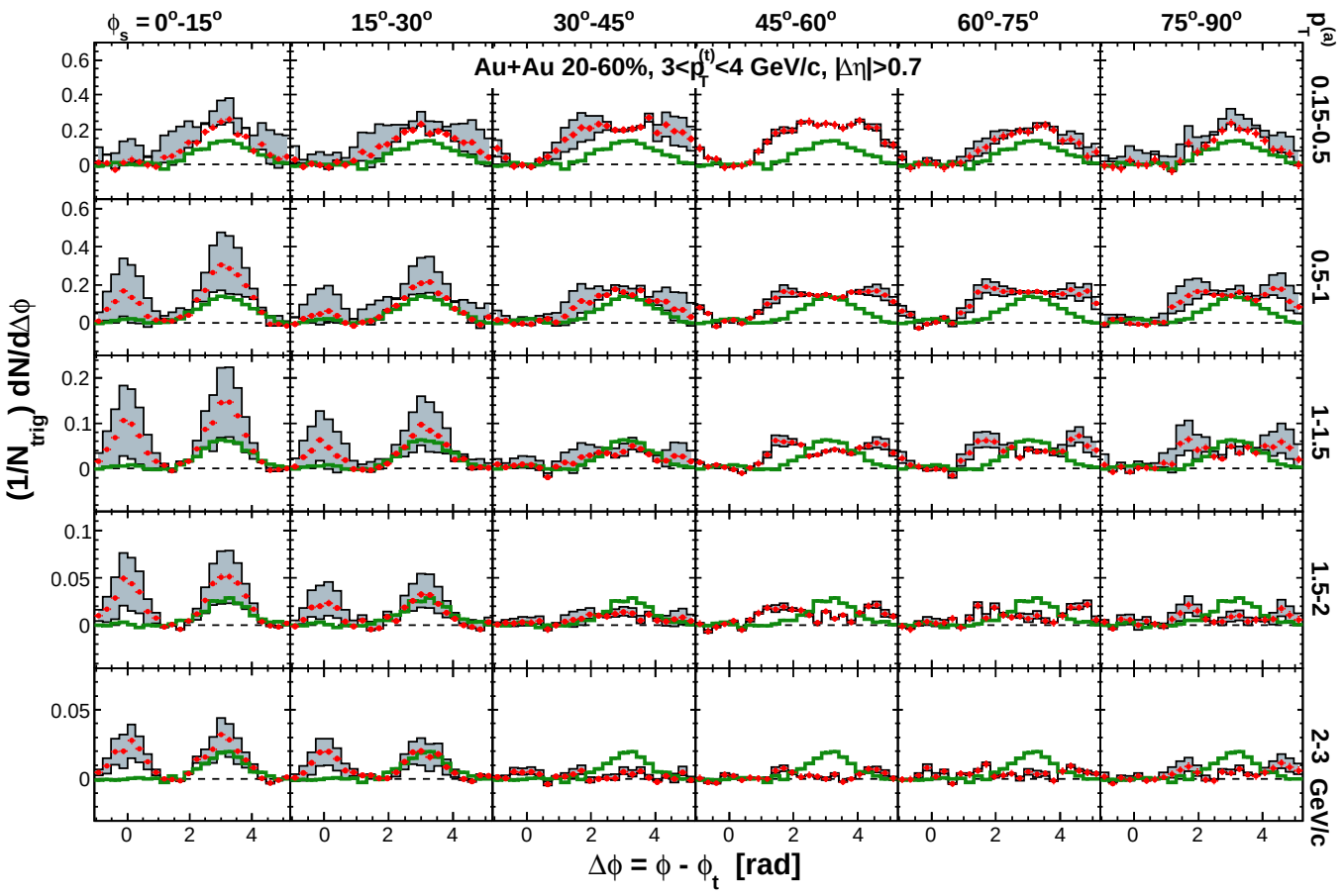

FIG. 37: (Color online) Background-subtracted dihadron correlations with trigger particle in six slices of azimuthal angle relative to the event plane, $\phi_s = |\phi_t - \psi_{\rm EP}|$, with a cut on the trigger-associated pseudo-rapidity difference of $|\Delta\eta| > 0.7$. The triangle two-particle $\Delta\eta$ acceptance is not corrected. The trigger p_T range is $3 < p_T^{(t)} < 4$ GeV/c. Five associated particle $p_T^{(a)}$ bins are shown. Both the trigger and associated particles are restricted to be within $|\eta| < 1$. The figure corresponds to the raw correlations in Fig. 29. The data points are from minimum-bias 20-60% Au+Au collisions. Flow background is subtracted by Eq. (10) using v_2 measurements in Table I and v_3 in Table V and the parameterization in Eq. (15). Systematic uncertainties due to flow subtraction are shown in the thin histograms embracing the shaded area; those due to ZYAM background normalization are not shown. Error bars are statistical. For comparison, the inclusive dihadron correlations from d+Au collisions are superimposed as the thick (green) histograms.

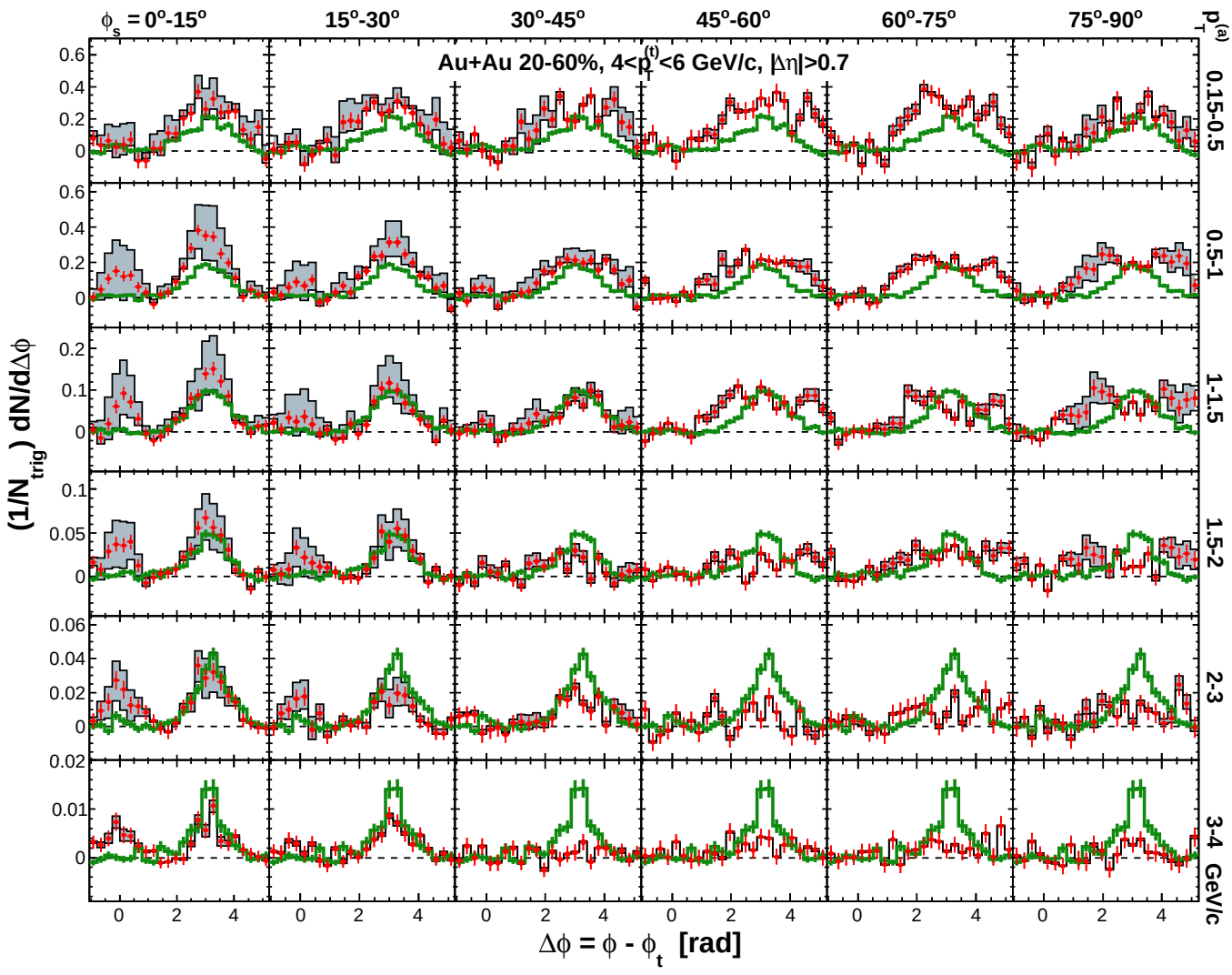

FIG. 38: (Color online) Same as in Fig. 37 but but for trigger particle $4 < p_T^{(t)} < 6$ GeV/c and six bins in associated particle $p_T^{(a)}$.

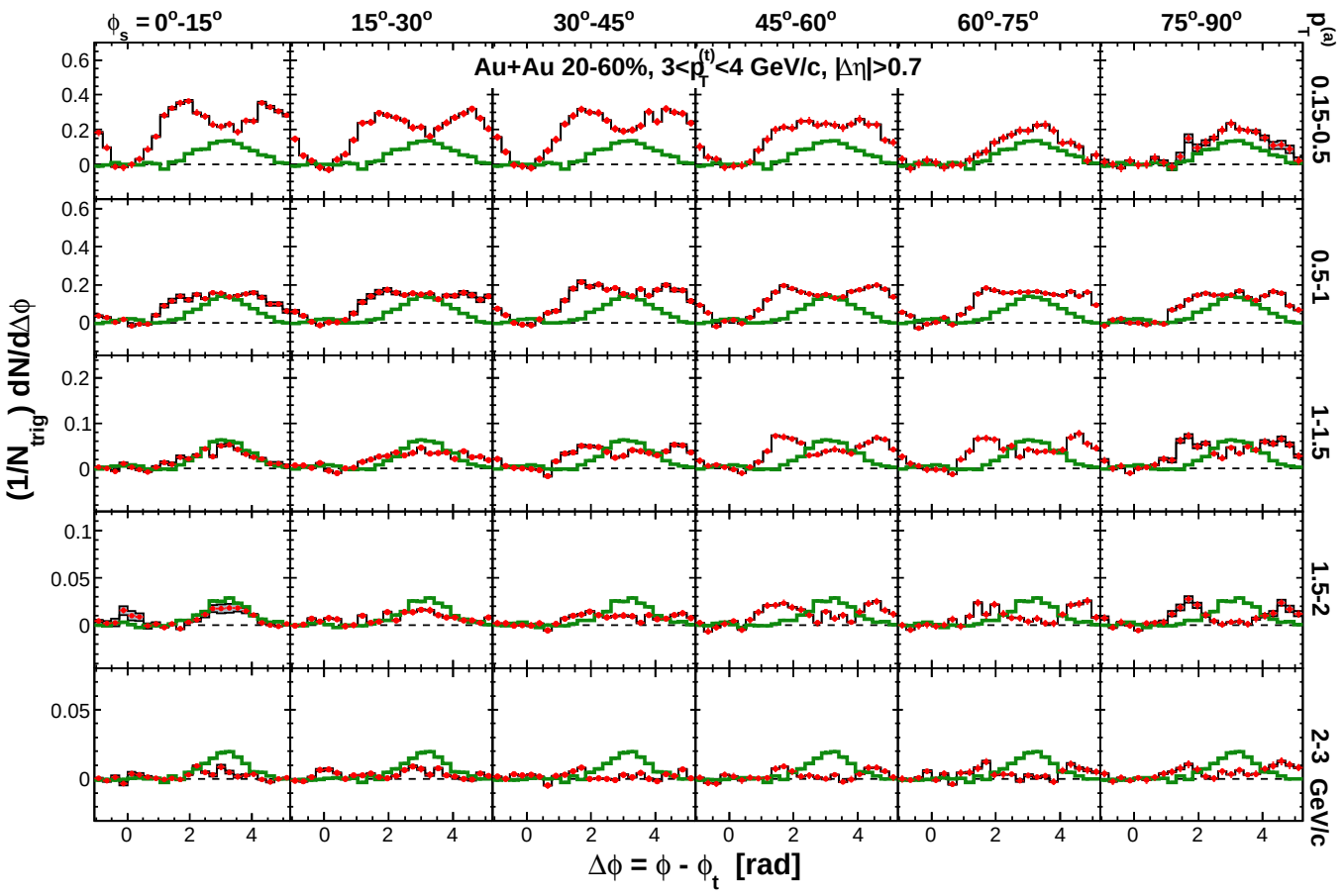

FIG. 39: (Color online) Background-subtracted dihadron correlations with trigger particle in six slices of azimuthal angle relative to the event plane, $\phi_s = |\phi_t - \psi_{\rm EP}|$, with a cut on the trigger-associated pseudo-rapidity difference of $|\Delta\eta| > 0.7$. The triangle two-particle $\Delta\eta$ acceptance is not corrected. The trigger p_T range is $3 < p_T^{(t)} < 4$ GeV/c. Five associated particle $p_T^{(a)}$ bins are shown. Both the trigger and associated particles are restricted to be within $|\eta| < 1$. The figure corresponds to the raw correlations in Fig. 29. The data points are from minimum-bias 20-60% Au+Au collisions. Flow background is subtracted by Eq. (11). The ϕ_s-dependent $v_2\{p_T\text{-}p_T\}$ measured by two-particle cumulants with $\eta_{\rm gap} = 0.7$ and 1.2 in Table VI are used (the thin histograms embracing the shaded area), with their average shown in the data points. The subtracted $v_3\{2\}$ is given in Table V. The subtracted $v_4\{\psi_2\}$ is parameterized by Eq. (15), and the $V_4\{\rm uc\}$ is given by Eq. (22). Error bars are statistical; systematic uncertainties are not shown. For comparison, the inclusive dihadron correlations from d+Au collisions are superimposed as the thick (green) histograms.

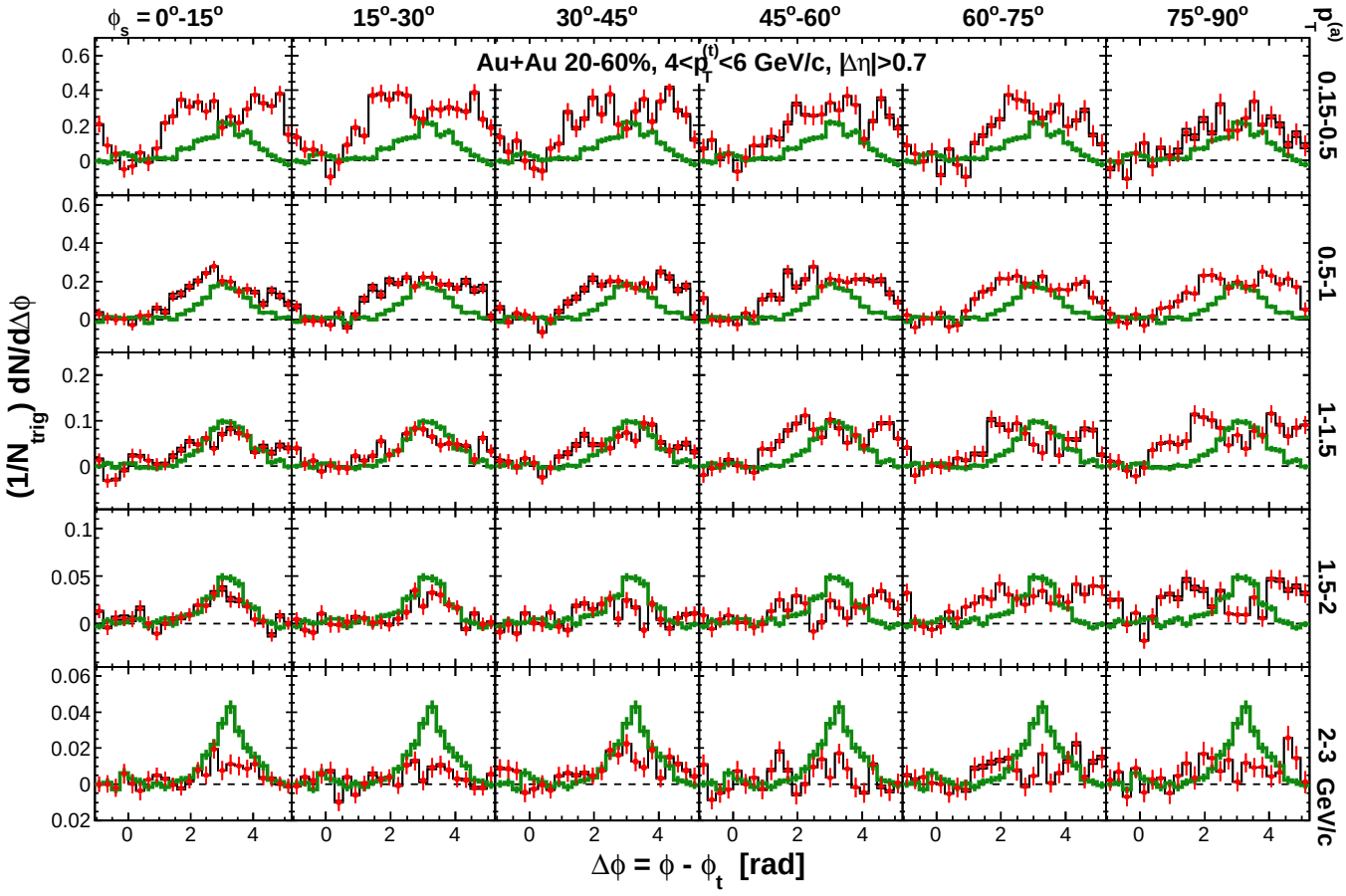

FIG. 40: (Color online) Same as in Fig. 39 but but for trigger particle $4 < p_T^{(t)} < 6$ GeV/c.